UPPSALA
UNIVERSITET

Digital Comprehensive Summaries of Uppsala Dissertations from the Faculty of Science and Technology 1365

Complex Excitations in Advanced Functional Materials

JOHANN LÜDER

ACTA
UNIVERSITATIS
UPSALIENSIS
UPPSALA
2016

ISSN 1651-6214
ISBN 978-91-554-9543-5
urn:nbn:se:uu:diva-282151

Dissertation presented at Uppsala University to be publicly examined in Å80101, Ångströmlaboratoriet, Lägerhyddsvägen 1, Uppsala, Friday, 13 May 2016 at 09:15 for the degree of Doctor of Philosophy. The examination will be conducted in English. Faculty examiner: Prof. Dr. Frank de Groot (Department of Chemistry, Utrecht University).

Abstract

Lüder, J. 2016. Complex Excitations in Advanced Functional Materials. *Digital Comprehensive Summaries of Uppsala Dissertations from the Faculty of Science and Technology* 1365. 90 pp. Uppsala: Acta Universitatis Upsaliensis. ISBN 978-91-554-9543-5.

Understanding the fundamental electronic properties of materials is a key step to develop innovations in many fields of technology. For example, this has allowed to design molecular based devices like organic field effect transistors, organic solar cells and molecular switches.

In this thesis, the properties of advanced functional materials, in particular metal-organic molecules and molecular building blocks of 2D materials, are investigated by means of Density Functional Theory (DFT), the GW approximation (GWA) and the Bethe-Salpeter equation (BSE), also in conjunction with experimental studies. The main focus is on calculations aiming to understand spectroscopic results.

In detail, the molecular architectures of lutetium-bis-phthalocyanine ($LuPc_2$) on clean and hydrogenated vicinal Si(100)2×1, and of the biphenylene molecule on Cu(111) were analysed by means of X-ray Photoelectron spectroscopy (XPS) and Near Edge X-ray Absorption Fine Structure (NEXAFS) spectroscopy; DFT calculations were performed to obtain insights into the atomic and electronic structures. Furthermore, detailed information about the electronic states of the gas phase iron phthalocyanine (FePc) and of the gas phase biphenylene molecule were obtained through XPS and NEXAFS spectroscopy. I have studied by means of DFT, multiplet and GWA calculations the electronic correlation effects in these systems. Also the optical, electronic and excitonic properties of a hypothetical 2D material based on the biphenylene molecule were investigated by GWA and BSE calculations. Monolayers of metal-free phthalocyanine (H_2Pc) on Au(111) and of FePc on Au(111) and Cu(100)c(2×2)-2N/Cu(111) with and without pyridine modifier were studied by XPS and final state calculations. A multiplet approach to compute L-edges employing the hybridizations function, known from dynamical mean field theory, was proposed and applied to transition metal oxides.

Keywords: X-ray Absorption Spectroscopy, Photoelectron Spectroscopy, Adsorption, Phthalocyanines, Biphenylene, Excitons, Functional Materials

Johann Lüder, Department of Physics and Astronomy, Materials Theory, Box 516, Uppsala University, SE-751 20 Uppsala, Sweden.

ISSN 1651-6214
ISBN 978-91-554-9543-5
urn:nbn:se:uu:diva-282151 (http://urn.kb.se/resolve?urn=urn:nbn:se:uu:diva-282151)

To Mankind - 'Live Long and Prosper'

Abstract

Understanding the fundamental electronic properties of materials is a key step to develop innovations in many fields of technology. For example, this has allowed to design molecular based devices like organic field effect transistors, organic solar cells and molecular switches.

In this thesis, the properties of advanced functional materials, in particular metal-organic molecules and molecular building blocks of 2D materials, are investigated by means of Density Functional Theory (DFT), the GW approximation (GWA) and the Bethe-Salpeter equation (BSE), also in conjunction with experimental studies. The main focus is on calculations aiming to understand spectroscopic results.

In detail, the molecular architectures of lutetium-bis-phthalocyanine ($LuPc_2$) on clean and hydrogenated vicinal Si(100)2×1, and of the biphenylene molecule on Cu(111) were analysed by means of X-ray Photoelectron spectroscopy (XPS) and Near Edge X-ray Absorption Fine Structure (NEXAFS) spectroscopy; DFT calculations were performed to obtain insights into the atomic and electronic structures. Furthermore, detailed information about the electronic states of the gas phase iron phthalocyanine (FePc) and of the gas phase biphenylene molecule were obtained through XPS and NEXAFS spectroscopy. I have studied by means of DFT, multiplet and GWA calculations the electronic correlation effects in these systems. Also the optical, electronic and excitonic properties of a hypothetical 2D material based on the biphenylene molecule were investigated by GWA and BSE calculations. Monolayers of metal-free phthalocyanine (H_2Pc) on Au(111) and of FePc on Au(111) and Cu(100)$c(2\times2)$-2N/Cu(111) with and without pyridine modifier were studied by XPS and final state calculations. A multiplet approach to compute *L*-edges employing the hybridizations function, known from dynamical mean field theory, was proposed and applied to transition metal oxides.

List of papers

This thesis is based on the following papers, which are referred to in the text by their roman numerals.

I **Photoelectron and Absorption Spectroscopy Studies of Metal-Free Phthalocyanine on Au(111): Experiment and Theory**
M.-N. Shariati, J. Lüder, I. Bidermane, S. Ahmadi, E. Göthelid, P. Palmgren, B. Sanyal, O. Eriksson, M. N. Piancastelli, B. Brena and C. Puglia, *J. Phys. Chem C*, **117**, 7018-7025 (2013)

II **Comparison of dispersion corrections and sparse-matter functionals at the H_2Pc - Au(111) interface**,
J. Lüder, B. Sanyal, O. Eriksson and B. Brena, *Physical Review B* **89**, 045416 (2014)

III **Experimental and theoretical study of electronic structure of lutetium bi-phthalocyanine**,
I. Bidermane, J. Lüder, S. Boudet, T. Zhang, S.Ahmadi, C.Grazioli, M. Bouvet, J. Rusz, B. Sanyal, O. Eriksson, B. Brena C. Puglia and N. Witkowski, *J. Chem Phys.* **138**, 234701 (2013)

IV **When the Grafting of Double Deckers Phthalocyanine on Si(100)-2$\times$1 Partly Affects the Molecular Electronic Structure**,
I. Bidermane, J. Lüder , S. Ahmadi, C. Grazioli, M. Bouvet, B. Brena, N. Mårtensson, C. Puglia and N. Witkowski *Submitted* ,

V **Characterization of gas phase iron phthalocyanine with X-ray photoelectron and absorption spectroscopies**,
I. Bidermane, J. Lüder, R. Totani, C. Grazioli, M. de Simone, M. Coreno, A. Kivimäki, J. Åhlund, L. Lozzi, B. Brena, and C. Puglia, *physica status solidi (b)* **252**, 1259–1265 (2015)

VI **Nature of the bias-dependent symmetry reduction of iron phthalocyanine on Cu (111)**,
O. Snezhkova, J. Lüder , A. Wiengarten, S. Burema, F. Bischoff, Y. He, J. Rusz, J. Knudsen, M.-L. Bocquet, K. Seufert, J. V. Barth, W. Auwärter, B. Brena and J. Schnadt *Physical Review B* **92**, 075428 (2015)

VII **Iron phthalocyanine on copper nitride: geometry, spin state, and modification by pyridine adsorption**,
O. Snezhkova, J. Lüder , S. Chaudhary, C. Coman, J. Knudsen, K. Schulte, B. Brena, and J. Schnadt, *In Manuscript*

VIII **Many-body effects and excitonic features in 2D biphenylene carbon**,
J. Lüder, O. Eriksson, B. Sanyal, H. Ottosson, and B. Brena, *J. Chem Phys.* **114**, 024702 (2016)

IX **The electronic characterization of biphenylene - Experimental and theoretical insights from core and valence level spectroscopy**,
J. Lüder , M. de Simone, R. Totani, M. Coreno, C. Grazioli, B. Sanyal O. Eriksson, B. Barbara and C. Puglia, *J. Chem Phys.* **142**, 074305 (2015)

X **Electronic correlations revealed by hybrid functional and GW calculations in the anti-aromatic biphenylene molecule**,
J. Lüder , B. Sanyal, O. Eriksson and B. Brena *In Manuscript*

XI **Core levels, valence band structures and unoccupied states of biphenylene films** ,
R. Totani, T. Zhang, C. Grazioli, J. Lüder, I. Bidermane, V. Lanzilotto, M. de Simone, M. Coreno, B. Brena, L. Lozzi and C. Puglia, *In Manuscript*

XII **Theory of X-ray spectroscopy of strongly correlated systems**,
J. Lüder, B. Brena, M. W. Haverkort, O. Eriksson, B. Sanyal, I. Di Marco, Y. O. Kvashnin, *In Manuscript*

Reprints were made with permission from the publishers.

Additional publications

The following publications resulted from work done under the Ph.D project but are not included as part of this thesis.

- **Revisiting the adsorption of Copper-Phthalocyanine on Au(111)**,
J. Lüder, O. Eriksson, B. Sanyal and B. Brena, *J. Chem Phys.* **140**, 124711 (2014)

- **The Influence of Electron Correlation on the Electronic Structure and Magnetism of Transition Metal Phthalocyanines**,
I. Brumboiu, S. Haldar, J. Lüder, H. C. Herper, O. Eriksson, B. Sanyal and B. Brena, *Journal of Chemical Theory and Computation* (2016)

The author's contributions to the publications

All work presented in the Papers I to XII has been a collaboration with other coauthors. Here, I briefly state my contributions to them. In the Papers I to XII, I have been responsible for the calculations and I have participated in discussions. I have written the manuscripts for the Papers in which I am the first author, e.g. II, VIII, IX, X and XII. For the other Papers in which I am not the first author, I helped to interpret the experimental results based on the theoretical ones and I wrote the theory part in conjunction with the experimental findings. In Paper XII, I actively worked on the realization of the approach presented.

Contents

1. Introduction

Higher, faster and stronger, these are key aims in most sports competitions. This brings up a very important question. How can we achieve this? It is very easy to map this driving point to materials research. Considering that 70% of all innovations are coupled to new insights into and development of materials [1], asking how materials can be designed and improved is a driving force of technological progress.

Key aspect of the systematic investigations is to understand the fundamental processes and mechanisms in materials and how the mechanisms can be made (among others) faster, more robust and energy efficient. If the quantum mechanical properties of a material shall be optimized in order to perform best for a certain task, spectroscopy has developed to be a powerful tool to investigate, monitor and understand the progresses in the developments of materials.

Spectroscopic tools can be very helpful. Their interpretation can be straightforward for simple systems like the hydrogen atom and quantum mechanics should be the theoretical backbone of this interpretation. However, more complex systems which actually can serve dedicated and complex purposes are more challenging to understand. Many effects can occur at the same time adding complexity, which is not necessarily desired. Nonetheless, also from these systems information can be extracted with spectroscopic experiments. Thankfully, there exists more than one technique to probe the state of a system. Consider for example Schrödinger's cat in a dark room in Figure 1.1 (i). Without light matter interaction, no spectroscopic information is obtained. However, the cat can be probed by light, but the questions are which light to use and for what purpose. If I would like to know if the cat has a fever, the infra-red photon could be measured, see Figure 1.1 (ii). If I would like to know the color of the cat, I shine visible light on it, Figure 1.1 (iii), and if I would like to learn about the bone structure of the cat I use X-rays, Figure 1.1 (iv). Even though it is always the same cat, I can "see" different parts of it, which added to the complete understanding. This shall demonstrate how in a similar way light-matter interaction can reveal different properties. Also, different kinds of spectroscopy can access different information and in the best outcome complement the understanding of a system or process.

This thesis deals with various kinds of theoretical methods to understand the results of experiments testing light-matter interactions and to contribute to materials research. The articles in this thesis can be divided in roughly three groups: (i) adsorption studies of organic molecules on substrates focusing on structure related phenomena (ii) investigating the electronic structure of

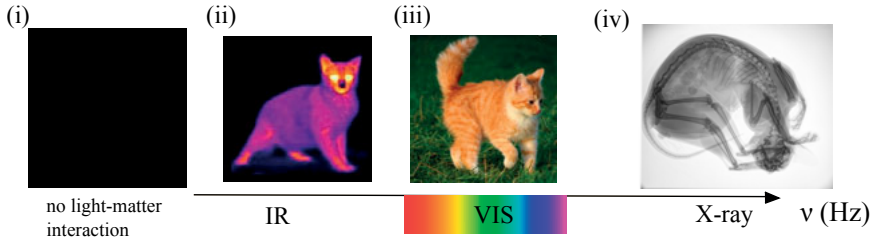

Figure 1.1. Schrödinger's cat seen without light-matter interaction (i), measuring the photon in the infra-red range (ii), in the visible region (iii) and with X-rays (iv).

(metal-)organic molecules in gas phase and the adsorption induced changes as possible building blocks for advanced 2D materials and (iii) implementation of a theoretical method for X-ray absorption spectroscopy.

In particular, phthalocyanine molecules with and without metal center are a prototype system. Their general structure is shown in Fig. 1.2. Most of the here presented studies investigate the intrinsic properties of phthalocyanine molecules or/and how their interaction with substrates and/or adsorbates, so-called modifiers. Phthalocyanines exist in several variants, which is achieved by combining the organic macro-cycle composed of four connected isoindole rings, each a fused benzo-pyrrole, in D_{4h} symmetry with a metal center. The metal centers are often transition metals, but they can be also alkali, alkali earth, lanthanide metals and others [2]. Note that in combination with lanthanide metals, the phthalocyanines form double and triple deckers [3, 4]. Phthalocyanines are already a target of research since several decades; starting from synthesizing various of them, even exotic ones like the gold phthalocyanine [5], over determining their properties and investigating possible technological applications . Research topics range from solar cells [6], to spintronics and as molecular magnets [7], single-molecule junctions [8], spin-filters [9], gas-sensors [10], field-effect transistors [11], photodynamic therapy [12], optical data storage [13] and others. In industry, they are already used as dyes due to their blue, cyan or green color.

The properties of phthalocyanines and their possible application in technology were investigated in the Paper I to VII. The adsorption of metal-free phthalocyanines (H_2Pc) on Au(111) was studied in the Paper I and II and the importance of van der Waals interactions between molecule and substrate were pointed out. The conclusions were supported by X-ray Absorption studies combined with Density Functional Theory calculations. The $LuPc_2$ was a research target in the Papers III and IV aiming to understand the difference in the interactions on a passivated and a reactive silicon substrate, as well as the molecular architectures in films forming on the substrates. The electronic states of the FePc gas phase molecule were investigated by means of 1s and 2p X-ray Photoelectron measurements and multiplet calculations in Paper V. Papers VI and VII investigate how the interaction of FePc with the Cu(111),

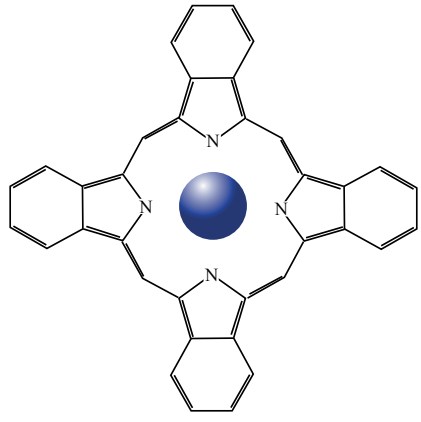

Figure 1.2. Chemical structure of a metal-phthalocyanine.

Au(111) and Cu(100)$c(2\times2)$-2N/Cu(111) surface, including the adsorption of a modifier, can reduce the symmetry of FePc and may change the electronic and the spin state.

Since the discovery of graphene, much attention was attracted by 2D materials. In particular, new carbon 2D allotrops may have for technological purposes desired properties. The search for new materials has motivated four of the biphenylene studies. Biphenylene is a small anti-aromatic molecule. It has been suggested to be a building block for new materials. The biphenylene molecule and a hypothetical 2D sheet constructed from it were studied in Papers VIII to XI, which also includes the adsorption of biphenylene on Cu(111) and its film architectures.

An efficient XAS multiplet method is suggested in Paper XII with applications to transition metal oxides.

2. About quantum mechanics and density functional theory

"Es gab eine Zeit, als Zeitungen sagten,
nur zwölf Menschen verstünden die Relativitätstheorie.
Ich glaube nicht, dass es jemals eine solche Zeit gab.
Auf der anderen Seite denke ich, es ist sicher zu sagen,
dass niemand die Quantenmechanik versteht." (German translation)
– Richard P. Feynman

The behaviour and the properties of microscopic systems are dictated by quantum effects. For an accurate understanding of the behaviour and the properties of microscopic systems the laws of quantum mechanics have necessarily to be taken into account. Quantum mechanics has given fundamental insights in innumerable branches of physics and in particular it has led to a detailed understanding of the physical and chemical properties of matter. As a result, we have been able to develop several technologies, like LEDs, solar cells and lasers, which are commonly used nowadays, based on quantum phenomena.

The theory of quantum mechanics began with the study of the black-body radiation problem in the beginning of the 20th century, where the work of Max Planck had a central role. In 1900, Max Planck solved the black-body radiation problem by describing light in terms of quantized oscillators, which lead to Planck's law of black-body radiation. He also postulated that the energy of the electro-magnetic field is quantized. This led to the well-known Planck's relation[1] for the energy E:

$$E = h\nu \tag{2.1}$$

with ν the frequency of the oscillators and the Planck's constant h. This equation connects the frequency of a photon to its energy. A further fundamental step came with the study of light-matter interaction performed by Albert Einstein who could explain the photoelectric effect. The latter is the phenomenon of the emission of electrons by a piece of metal or other material, when shone by light with a certain frequency. Einstein moved further from Planck's energy relation, developing the idea of the quantized nature of the electro-magnetic field and therefore also of light. His interpretation was that an energy transfer between light and matter can only happen in discrete quanta, so-called photons, at certain energy as given in Eq. (2.1).

[1] or Planck-Einstein relation

Further basic advancements were about to come. In 1913, Niels Bohr extended the quantum energy hypothesis to the electronic energy levels of atoms, showing that the electrons in an atom occupy quantized energy levels.

In 1925, Erwin Schrödinger formulated the fundamental equation of quantum mechanics, the Schrödinger equation. Its time-independent form is given, as below, by

$$\left(-\frac{\hbar^2}{2m}\nabla^2 + v(\mathbf{r})\right)|\Psi(\mathbf{r})\rangle = E\,|\Psi(\mathbf{r})\rangle \tag{2.2}$$

which describes the energy E of the state $|\Psi(\mathbf{r})\rangle$ as sum of the potential and kinetic contributions. This equation is a fundamental ansatz to describe ground and excited states of a quantum system. In the hydrogen atom, for example, the wave function can be described as a so-called *s*-orbital wave function, where '*s*' stands for sharp. This simple one-electron system can be solved analytically, but an analytic solution cannot be obtained for other systems, like technologically relevant systems with many electrons. This is caused by the increasing complexity caused by many electrons interacting with each other and the resulting many-body effects.

Since the early description of quantum mechanics, there was and there still is a strong connection to experimental spectroscopical techniques. Spectroscopy experiments are powerful to extract unique information on electronic states in matter. In addition, also the heritage from the early atomic spectroscopy experiments can be found in the conventional terminology of quantum mechanics, like the terminology for the electronic quantum states, that we use nowadays.

The earlier mentioned *s*-orbital is an example. The conventional label '*s*' was taken from the description of spectroscopic lines of alkali metals. Further labels are '*p*' for principle, '*d*' for diffuse and '*f*' for fundamental. The precise properties of those orbitals are also linked to their principle quantum number '*n*', addressing shells, in addition to the orbital quantum number '*l*'. Here, particular properties of the many electron systems will be related to those orbitals. Furthermore, the magnetic quantum number '*m*', divides the states of a particular angular moment into $2l+1$ orbitals.

Throughout the present thesis, several discussions about the different orbitals will be presented. Also the intrinsic spin of an electron, a well-known fermion[2], is of relevance. Fermions have different properties than bosons[3] since they have to obey to the Pauli exclusion principle. This imposes that fermions within the same system, like in the same orbital, must have at least one quantum number, e.g. n, l, m or s, *not* in common. A fundamental consequence of this is that only two electrons with opposite intrinsic spin can occupy the same orbital. It should be highlighted that the Pauli exclusion principle is

[2]particles with on half numbered intrinsic spin

[3]particles with an integer intrinsic spin

probably one of nature's laws with the most important consequences for us. One example are the magnetic properties of matter. But even the physics of macroscopic objects like stars can be determined and explained by the Pauli exclusion principle. For example white dwarf stars, the expansion driven by the fusion processes has ended and their resistance to the gravitational compression is only given by its electron-degenerate matter, e.g. the Pauli exclusion principle. In addition, the exclusion principle is linked to spin and gives an explanation to the existence of neutron stars. In those stars, electrons and protons are merged to neutrons and the total gravitational collapse is prevented by the exchange interaction, too.

The electrons in the atoms follow the Aufbau principle, which basically states that the occupation of orbitals with electrons follows certain physical trends. The latter ones are motivated by the minimization of energy by occupying the energy levels with the lowest energy first.

Relativistic effects are included in the Dirac equation. The spin-orbit coupling is a consequence of this relativistic description. Generally, the moving electron with an orbital momentum l different from 0 creates an effective magnetic field which interacts with the spin of the electron. The strength of the coupling depends on the motion of the electron. Therefore, electrons closer to the atomic core have a stronger spin-orbit coupling than the valence electrons, which are electrons of the outermost shell. Experimental effects of this can be seen, for example, in the so-called L_3-L_2 splitting of X-ray Absorption Spectroscopy (XAS) measurements or the $p_{3/2}$ and $p_{1/2}$ splitting in X-ray Photoelectron Spectroscopy (XPS)[14].

While this brief description of many important quantum mechanical characteristics of fermionic systems is far from complete, it intends to provide a basis for the remaining discussion. In depth explanations of these and other important phenomena, like the uncertainty principle by Heisenberg, can be found in the standard literature of detailed introductions to the quantum mechanics of atoms, for example, in Ref. [15] and [16].

2.1 Density functional theory

As pointed out before, to find an analytic solution to the Eq. (2.2) for many-electron systems is, apart from a few exceptions, not possible. To describe realistic materials, which typically have many electrons, approximations concerning the wavefunction and the operators, are essential.

Early developments in this direction were the Thomas-Fermi theory, based on the electronic density, and the Hartree-Fock method, based on the antisymmetric fermionic wave functions. However, the essential step on the way to a quantitative description of real materials was taken by the formulation of the Density Functional Theory (DFT).

The Hohenberg-Kohn theorems

The Hohenberg-Kohn theorems [17] are the foundation of DFT. They show formally that the knowledge of the exact electronic density is sufficient to uniquely determine the total energy of the ground state of a many electron system. Briefly, the two theorems state:

(a) "[..] $v_{ext}(r)$ is (to within a constant) a unique functional of $\rho(r)$; since, in turn, $v_{ext}(r)$ fixes H we see that the full many-particle ground state is a unique functional of $\rho(r)$. [..]"

(b) "[..] for a system of N particles, the energy functional [..] has a minimum at the correct ground state $|\Phi\rangle$, relative to arbitrary variations [..] in which the number of particles is kept constant. [..]"

The first theorem has the important consequence that the ground state density $\rho(r)$ uniquely determines the external potential $v_{ext}(r)$. By knowing the external potential, the Hamiltonian of an N electron system is fully determined. Therefore all ground and excited state properties can in principle be obtained from $\rho(r)$. In practice, the ground state density is obtained via the variational principle, which relies on the second theorem, which states that the true ground state density minimizes the total ground state energy of the electronic density functional. Even though the original formulation was only exact for systems with nearly constant or slowly varying densities [17], the DFT approach has been extremely successful for computing the properties of a huge number of systems including atoms, molecules, clusters or crystals in materials theory.

DFT includes the correlation energy, which is missing in the Hartree-Fock theory as a consequence of the missing Coulomb correlation in the single-determinant ansatz. Then, the Hartree-Fock total energy is an upper-bond in the variational principle applied to DFT. This is used to define the correlation energy E_c, introduced by Löwdin, as difference between true total energy E and the total energy of Hartree-Fock limit. However, since the true total energy and the correlation energy are unknown, this formulation is of limited practicality.

The Kohn-Sham scheme

A practical and successful ansatz to perform DFT calculations was introduced by Kohn and Sham [18]. The Kohn-Sham approach, a simplification to the many-body problem, is widely used to solve the Schrödinger equation for many-electron systems.

The Kohn-Sham formalism introduces the same orbitals used in the Hartree-Fock scheme into DFT. Unlike in the Hohenberg-Kohn theory, the kinetic energies and the density are calculated directly from the single electron states $|\varphi_i\rangle$. The static Schrödinger equation Eq. (2.2) is modified into the Kohn-Sham equation

$$\widehat{h}_{eff}\,|\varphi_i\rangle = \varepsilon_i\,|\varphi_i\rangle \tag{2.3}$$

where $|\varphi_i\rangle$ is an one-electron wave function replacing the many-body wave function $|\Psi\rangle$, $\hat{h}_{eff}$ is an effective Hamiltonian which includes the electronic density via the mean-field approximation in an effective electronic potential and ε_i are the eigenvalues to the one-electron wave function $|\varphi_i\rangle$.

The effective Hamiltonian $\widehat{h}_{eff}$ for the free electron is given by:

$$\widehat{h}_{eff} = \left(-\frac{\hbar^2}{2m}\nabla_i^2 + v_{eff} \right) \tag{2.4}$$

which is the sum of the kinetic energy of a free electron and an effective potential v_{eff}. The effective potential v_{eff} is the sum of three components

$$v_{eff} = v_{ext} + v_{xc} + v_H \tag{2.5}$$

with the external potential v_{ext} which describes the Coulomb interaction between the electrons and the nuclei. The Hartree term, or direct term, v_H accounts for the Coulomb repulsion between electrons, but it also includes the so-called *self-interaction*[4] of the orbitals. The density ρ is obtained from the N occupied single electron orbitals:

$$\rho = \sum_i^N |\langle \varphi_i | \varphi_i \rangle|^2. \tag{2.6}$$

The exchange-correlation term v_{xc} is defined as

$$v_{xc} = \frac{\delta E_{xc}}{\delta \rho} \tag{2.7}$$

which accounts for the exchange-correlation energy. The exact, explicit form for the exchange-correlation potential is not known but it has to include a term for the exchange energy, known from the Hartree-Fock (HF) theory, and one for the correlation energy, which is absent in the HF theory.

In the Hamiltonian the kinetic energy of the nuclei is omitted. This is the so-called Born-Oppenheimer approximation [19] and as a result the Hamiltonian is reduced to the electronic problem and the positions of the nuclei are assumed to be fixed.

The total energy E_{KS} can be expressed in terms of the eigenvalues, the density, the Hartree energy E_H and the exchange-correlation potential

$$E_{KS} = \sum \varepsilon_i - E_H[\rho] + E_{xc}[\rho] - \int \frac{\delta E_{xc}[\rho]}{\delta \rho} \rho d\mathbf{r}. \tag{2.8}$$

where summation and integration run over occupied states.

The Kohn-Sham Eq. (2.3) describes in practice an electron moving in an effective potential due the external potential and the effects of the Coulomb

[4] It is an artifact of the method, resulting in the inclusion of the interaction of an electron with itself

interactions between the electrons [18]. This turns DFT into a theory of N independent single electrons, where the many-body effects are included via the exchange-correlation potential [20]. It is important to observe that the Kohn-Sham Eq. (2.3) is an exact equation. All contributions except the exchange-correlation potential v_{xc} are explicitly known, while v_{xc} is introduced in approximated forms, of which a large number have been so far proposed [21–23]. The many body problem is reduced to determine a self-consistent field of N electrons in an external potential.

The fundamental question in DFT is the form of the exchange-correlation functional. An analytic expression was derived for the exchange contributions. It relies on the homogenous electron gas. Its correlation part instead, was obtained through Quantum Monte-Carlo calculations. The resulting functional depends on the local density at a point $\mathbf{r}$, and therefore it is called local density approximation [21, 22] (LDA). Also a spin-polarized functional in that form exists. It is referred to as local spin density (LSD) functional [21], which has been a very popular approach so far. In systems with inhomogeneous densities, the generalized gradient approximation [23–26] (GGA) was proposed to account for variations in the density in the exchange-correlation functional.

However, there are problems related to these approximated functionals. DFT suffers from an artificial problem of the *self-interaction* (SI) of an electron with itself. The Hartree-Fock theory, in contrast, is free of this problem. Also, London dispersion forces [27], e.g. spontaneously induced dipole-dipole interaction, are not captured by standard DFT. Finally, the energy- or band-gap problem is very likely the most notorious weak spot of DFT. The latter is simply the systematical underestimation of the fundamental gap in molecules as well as in crystalline solids in DFT calculations. This is closely linked to the *derivative discontinuity* of the exchange-correlation functional [28, 29]. We can express the fundamental gap as energy difference between two characteristic energies. One of them is the first ionization energy (IE), the least energy required to remove an electron from the material. The other is the electron affinity (EA) which is the energy released when an electron is added to a neutral material. Eventually, based on Koopmans' theorem mapped to DFT, the eigenvalues of the highest valence state (HVS) and the one of the lowest conduction state (LCS) would correspond to the experimental energies. However, DFT typically underestimates the difference of both by 20% to 50% [28, 29]. Also the absolute energies are not accurately described. At the same time keeping in mind, that DFT is defined for the N electron system in its ground state, comparing the energies to an N-1 and N+1 electron systems appears to be outside the capability of DFT.

Besides all shortcomings of DFT, it is well established in materials calculations. It has become a very efficient tool, for example, to determine the atomic and electronic structure of various materials. New achievements in material science can be based on DFT. The prediction of transparent dense sodium is an example [30]. When the limitations of DFT results become evident, other

methods need to be used. Many-body Green's function techniques as employed in the GW method and the dynamical mean-field theory (DMFT) are examples of those [31]. But also for them, DFT is an important contribution, since the starting points for many methods are taken from DFT. However, another ansatz is to improve the approximations in the only unknown part of DFT itself, the exchange-correlation functional. This is attempted, for example, by so-called hybrid functionals [21, 32–38]. Another consequence of the local nature in the exchange-correlation functional is the lack of van der Waals interaction, which can be addressed in sparse-matter methods [39–48].

In the following, relevant methods will be outlined. The spectroscopic techniques relevant for this thesis are discussed in Chapter 3 and their connection to DFT and to methods to simulate spectra is introduced in Chapter 4. Finally, Chapter 5 summarizes the results published in the articles I to XII.

2.2 Hybrid functionals

While DFT employs an approximate expression for the exchange contribution, the HF theory uses an exact expression. It is an easy conclusion to question the performance of the DFT counterpart. For molecular systems, neither DFT at the LDA/GGA level nor HF theory could obtain sufficient agreement with experimental data for important properties like, for example, the atomization energies and the ionization potential [33, 49]. The reasons for this are linked to the approximations made in the two theories. While the pure Hartree-Fock results miss correlation effects, the local and semi-local approximations do not capture all of the physics in systems with fast varying density.

It turned out that for molecular systems, the inclusion in the functional of a part of exact exchange could dramatically improve the results [33, 38, 49]. The combination of DFT with exact exchange yields the very successful approach of hybrid functionals, of which a large variety exist today. With the partial exchange contributions in common but with different amounts, they differ in the complex interplay between the correlation and exchange. Particularly successful hybrid functionals are, for instance, B3LYP [21, 33–35] and PBE0 [50, 51]. In the latter one, the exchange-correlation contributions to the total energy functional are given as

$$E_{xc} = E_c^{GGA} + \frac{3}{4}E_X^{GGA} + \frac{1}{4}E^{HF} \tag{2.9}$$

with 25 % exact exchange E^{HF} and 75 % exchange from GGA (E_X^{GGA}) while the correlation energy E_c^{GGA} is taken from GGA only. This parameterization is motivated by perturbation theory. B3LYP instead has 20 % exact exchange and an additional mix of LDA and the GGA exchange correlation terms, whose parameterization gives the best results for various experimental references for a test set of molecules. This can be seen as *one-for-all* functional philosophy.

Although very successful in the computation of several properties, also hybrid functionals like B3LYP have functional typical weak spots: charge transfer excitations, polarizability for long chain molecules and time-dependent excitations are examples for B3LYP [32]. Improvements have come with the range-separated hybrids [32, 36, 37]. These use a division of the Coulomb operator r^{-1} in a short-range (SR) and a long-rang (LR) part, often through an Ewald split. In detail, the short and long range part can be expressed through the error function as

$$\frac{1}{r} = \frac{1-(\alpha+\beta erf(\gamma r))}{r} + \frac{\alpha+\beta erf(\gamma r)}{r} \tag{2.10}$$

where α, β and γ are adjustable parameters[32].

The exact-exchange is applied to one part and the DFT exchange counterpart on the other one. Details depend on the particular ansatz and the system of interest [32, 36, 37, 52, 53]. Also, a variety of different range-separated hybrid functionals has been proposed; CAM-B3LYP [32] and HSE [36, 52] are well known representatives. The latter functional, for instance, applies exact-exchange at short-range.

Another ansatz searches for the optimal functional for each system individually, a *one-for-one* kind of approach. By determining the best interplay between Hartree-Fock and DFT exchange potentials via providing those parts with a longer or shorter effective range, an optimally tuned range separated hybrid functional (OT-RSH) can be obtained [54]. In practice, this can be achieved through a suitable choice of the range-separation parameter γ and the mixing parameters α and β. To avoid ambiguity, the ionization potential theorem (IPT) motives the choice of the parameters, which have to be obtained for each system independently. In practice, the residual J between the IE and the corresponding electron eigenvalue are minimized according to

$$J^2(\gamma) = \sum_i \left(\varepsilon^{(\gamma)}(N+i) - IE^{(\gamma)}(N+i)\right)^2. \tag{2.11}$$

The IPT for DFT is equivalent to Koopmans' theorem and makes the scheme therefore non-empirical [54]. The OT-RSH approach has been very successful; the ionization energies, for example, can be obtained within 0.05 eV from measured values for molecules [53, 55, 56].

2.3 DFT and van der Waals interactions

Van der Waals (vdW) interactions play an important roll in many fields of science and are even observable in normal life. Although the vdW based chemical bonds are very weak, the vdW interactions are responsible for several macroscopic effects. For instance certain small animals can stick on walls without the need to use claws or any kind of glue. Examples are arthropods

like spiders and insects like ants, but for sure the most impressive case is a reptile, the gecko. In spite of being much heavier than most arthropods, geckos can stick on vertical walls thanks to the vdW interaction between their feet and a wall, which are strong enough to defeat the gravitational pull. It has been estimated that the vdW forces between surfaces and the feet of geckos can reach values of a few tens of N.

A part from the inspiring phenomena in nature, vdW interactions need to be considered to understand important technological fields. For example they affect the self-assembly of molecules [57, 58], the surface-molecule interface [59–61] and the polymorph structures of molecular crystals [62]; systems which are of high relevance for molecular electronics [63] and drug design [64, 65]. Implementing efficient methods to compute vdW interactions in materials theory simulations has become a crucial aspect of modern research, and it has gained increasing interest in recent years [66, 67]. Van der Waals models have been developed from an empirical potential to today's state of the art *ab initio* descriptions of various kinds [46, 68, 69].

The first time that the interaction between non-polar and non-charged molecules was described goes back to Johannes Diderik van der Waals[5] in 1869. The field was further developed in the 1930's by Fritz London, who employed perturbation theory in the framework of quantum mechanics [27]. In his consecutive works, he could derive a potential decaying with R^{-6} on the ansatz of spontaneous polarization [27].

The Kohn-Sham equation (Eq. 2.3) is exact, but the unknown exchange-correlation potential v_{xc} in the local and semi-local approximation, e.g. LDA and GGA, as well as in hybrid functionals like B3LYP, does not cover the dispersion effects at the long range scale, like the vdW interactions. Thus, the predictive power of DFT and the realistic description of materials, in which those interactions are important, with DFT are diminished. It is well known for example that LDA typically underestimates bond lengths of weakly interacting systems, while GGA overestimates them [59].

The steady development in the understanding and modeling of vdW interactions has generated a large variety of methods to be coupled to DFT that will be introduced in the next paragraphs.

Pair-potential approaches

The pair-potential based methods (C_6R^{-6}) follow the idea of adding a long range correlation term E_{vdW} to the total Kohn-Sham energy E_{KS} of Eq. (2.8). The new total energy can be expressed as

$$E_{KS+vdW} = E_{KS} + E_{vdW}. \tag{2.12}$$

[5] Johannes Diderik van der Waals received the Nobel Prize in physics in 1910 for "for his work on the equation of state for gases and liquids" - the discovery of the van der Waals interaction

A general form for E_{vdW}[40] may be written as

$$E_{vdW} = s_0 \sum_{i,j \neq i} C_6^{ij} R^{-6} \times f(R, R_{6i}, R_{6j}) \tag{2.13}$$

with an empirical scaling constant s_0 for each DFT functional, the damping function f, the dispersion coefficients C_6^{ij} and the vdW radii R_{6i} and R_{6j}. The indices i and j run over the atoms. The pairwise term C_6^{ij} can be derived in several ways [70] for example with the adiabatic connection fluctuation dissipation (ACFD) theorem [71] in the random phase approximation (RPA) [41]. Common features of all pair-potential methods are the strictly additive character of the dispersion energies [39] and the use of dispersion coefficients (C_6 and R_6) for each element. The C_6 coefficient accounts for the interaction through induced dipole moments, which depend on the polarizability as can be seen from the Casimir-Polder integral [72]. The vdW-radii instead are not a quantum mechanical observable [39], but they act as a scaling factor of the separation distance in the damping function f.

Within the pair-potential approaches, different schemes to determine E_{vdW} have been elaborated. Due to the force field-like design, the C_6R^{-6} methods are highly efficient allowing investigations of large systems with applications in technology [66] and medicine [62].

A method which has been very successfull is the DFT-D2 method by Grimme [40], which is a successor of a previous DFT-D1 implementation [73]. This method has obtained very good results for many systems like dimers [74] as well as for the adsorption on surfaces [75]. The C_6 are computed with atomic ionization potentials and with atomic static dipole polarizabilities obtained from DFT/PBE0 calculations. The values for the R_6 reference coefficients are calculated from electron density contours which are obtained from restricted open shell Hartree-Fock calculations [40].The pairwise C_{6ij} dispersion coefficients are of the form

$$C_{6ij}^{D2} = \sqrt{C_{6i} C_{6j}} \tag{2.14}$$

which is motivated by empirical tests [40]. This vdW correction, however, is known to underestimate bond lengths and to overestimate adsorption energies for molecules on some metal surfaces [59, 76].

Another very successful pair-potential-like vdW implementation is the Tkatchenko-Scheffler (TS) method which includes a density dependence in the C_6 coefficients. An expression for the pairwise C_{6ij} coefficient can be derived from the Casimir-Polder integral [39, 72] The C_{6ij} coefficients are evaluated according to

$$C_{6ij}^{TS} = \frac{2 C_{6i} C_{6j}}{\frac{\alpha_j^0}{\alpha_i^0} C_{6i} + \frac{\alpha_i^0}{\alpha_j^0} C_{6j}} \tag{2.15}$$

where $\alpha^0_{i/j}$ are the static polarizabilities; clearly indicating a certain ambiguity among the pair-potential methods. The Hirschfeld partitioning of the ground state density generates the density dependence of the pair coefficients. TS is constructed in a way that the only empirical parameters, which are d, a fitting parameter, and s_0 the scaling constant, are part of the damping function f. Similar to DFT-D2, the R_6 reference coefficients are derived from atomic ground state densities while reference data of α^0 and C_6 are obtained from self-interaction corrected time-dependent DFT calculations [77].

A common drawback of the C_6R^{-6} method is constituted by the purely additive pairwise C_{6ij} coefficients [39] and by the resulting overestimation of the correlation term E_{vdW} with increasing system size [41]. This is a result of neglecting the correlation of higher order multipoles and of missing screening effects [69]. Another aspect of the TS method is the influence of the static polarizability α^0. It has been shown that dispersion coefficients of nanomaterials are not necessarily constant for a specific element [67]. For instance, the diversity of existing carbon based materials like graphene, carbon nanotubes, or organic molecules and their differences in dimensionality also cause large complexity in the electronic structure [67]. The resulting differences in the electronic density can change polarizability and therefore different interaction strengths can be a consequence.

Further improvements to account for the systems dependence can be gained if many-body effects are included in the vdW methods. The TS-SCS method considers electromagnetic screening of the polarizabilities of atoms in molecules and solids [41]. By considering electrons in atoms as quantum harmonic oscillators, the screened polarizabilities α^{SCS} can be obtained which effectively reduce the interaction strength between pairs of atoms.

Rutgers-Chalmers vdW-density functionals

The sparse-matter density functionals (vdW-DF) aim to improve the description of the long-range correlation in a density dependent fashion [42, 43, 45–48]. In this way, they are considered to be a non-local density functional. The exchange-correlation term E_{xc}^{vdW-DF} of the sparse-matter functionals can be split into three contributions:

$$E_{xc}^{vdW-DF} = E_x^{GGA} + E_c^{LDA} + E_c^{nl} \tag{2.16}$$

with the GGA exchange potential E_x^{GGA}. E_c^{LDA} and E_c^{nl} account for the correlation potential. In detail, the correlation has a local (E_c^{LDA}) and a non-local (E_c^{nl}) term. The interplay between the three terms is complex and an appropriate choice aims in resulting in an universal functional that can go beyond the existing local and semi local ones. The *"unknown"* term in this case is the E_c^{nl}. Finding a simplified and accurate expression for E_c^{nl} is essential and non-trivial, and the ACDF theorem in the so-called full potential approximation [46] is used to derive an expression for E_c^{nl}.

The Rutgers-Chalmers density functions, also called vdW-DFs, have been successfully applied among many other systems, to layered systems [45], to the adsorption of molecules on surfaces [78] and on other weakly bonded systems [48]. Dion *et al.* proposed a non-local functional, the vdW-DF [46], for systems with arbitrary geometries as a generalization of the vdW-DF for layered systems [45] like graphite. However it has been observed that vdW-DF suffers from an overestimated adsorption distance for the molecules on surfaces, and an overestimation of the lattice constants of molecular crystals [42, 79]. Improved many-body scaling and electron-hole conservation yielded the long-range correlation of DF2 [47], usually named vdW-DF2, which represents an improvement in the performance of the vdW-DFs [47, 59].

A detailed analysis conducted by Klimeš et al. have shown that the too repulsive Pauli wall leads to overestimated distances between weakly interacting systems [43]. Improvements can be achieved by changing the exchange potential [43] which aims to gain a reduction of the Pauli repulsion strength. Several alternative sparse-matter functionals were proposed as for example vdW-DF-09, optB88-DF and optB86b-DF [42–44].

3. The physical background of spectroscopy

UV and X-ray spectroscopies are widely used techniques in materials science. These experimental methods have the capability to unveil the states of complex quantum systems like the electrons in an atom, molecule or solid crystal, giving unique element specific information. Several different techniques have been developed during the years, which can nowadays be performed at synchrotron radiation facilities like the MAX IV facility in Lund, Sweden [80].

X-rays, discovered by Wilhelm Röntgen[1] in 1895, are a versatile spectroscopic probe that allows the examination of a vast range of materials in many fields of science, in industry and in medicine for diagnostic purposes. Today, X-ray spectroscopy is an important method in state-of-the-art materials research. Several experimental techniques have been developed, which are widely used to obtain insights into the structure [81–83], chemical com- position [84] and electronic states [85] of materials such as molecules, surfaces and solids [86]. The combination of experimental results and theoretical simulations, which has been used in several works of the present thesis, is an especially powerful combination. The theory via accurate simulations of the materials and of the physical processes at the basis of the spectroscopy can in many cases describe the measured spectra at a detailed level, and different materials properties can be explained. Many UV based and soft X-ray based experimental spectroscopic techniques exist [87–89], with photon energies in the range between a few to a few thousands of eV.

The fundamental physical process at the basis of all these spectroscopies is the interaction of photons with electrons. Since the photon energy can be chosen across a wide energy window, very different events can be generated, as will be briefly illustrated in the following part. At low energies, an excitation caused by light in the visible range, e.g with an energy between c:a 1.7 and 3.3 eV, can promote a valence electron into an unoccupied state. At energies a bit larger and in the order of tens of eV, valence electrons can usually leave the system. This is the basics of PES of valence electrons described by the so-called outer photoelectric effect, the one explained by Einstein. The excitation radiation can in this case be UV or X-rays. At even larger photon energies, also core electrons can be excited into unoccupied states. This is XAS which triggers neutral excitations since the total charge of the system is unchanged. At energies larger than those of XAS experiments, the core electrons can leave the system, as in the PES experiment sketched in Fig. 3.1, also called XPS.

[1] Wilhelm Conrad Röntgen (1845-1923) was a German physicist. He obtained the first Nobel Prize in Physics in 1901 for the discovery of X-rays.

The Fermi golden rule

The absorption of soft X-ray radiation is a specific example of the light matter interaction. The Hamiltonian H_{el} describing the electron interacting with the electromagnetic field may be written as

$$H_{el} = H_0 + H_A \tag{3.1}$$

where H_0 is the Hamiltonian and H_A represents the perturbation caused by the electromagnetic field. This form is well-known from linear response theory. In detail,

$$H_A = \frac{e}{mc}\mathbf{A}\cdot\mathbf{p} \tag{3.2}$$

expresses the interaction between the electron with momentum $\mathbf{p}$ and the electromagnetic field of the photon.[2] The complex vector potential $\mathbf{A}$ is expressed by:

$$\mathbf{A} = A_0\mathbf{E}\left(e^{i(\mathbf{k}\cdot\mathbf{r}-t\omega)} + e^{-i(t\omega+\mathbf{k}\cdot\mathbf{r})}\right). \tag{3.3}$$

where A_0 is the intensity, $\mathbf{E}$ is the polarization vector, $\omega = 2\pi\nu$ is the frequency and $\mathbf{k}$ is the wavevector of the electromagnetic field. With time-dependent perturbation theory, it is possible to derive the so-called Fermi's golden rule. It describes the transition of an electron from an initial into a final state due to an excitation process induced by the absorption of a photon. The Fermi golden rule expresses the transition rate w as

$$w = \frac{2\pi}{\hbar}|\left\langle\phi_f\right| H_A \left|\phi_i\right\rangle|^2\delta(E_i - E_f + h\nu). \tag{3.4}$$

Assuming that the wavelength of the photons is much longer than the dimension of the atoms, the transition probability w can be approximated in the dipole approximation as:

$$w_D = \frac{2\pi}{\hbar}|\mathbf{E}\left\langle\phi_f\right| \hat{T} \left|\phi_i\right\rangle|^2\delta(E_i - E_f + h\nu). \tag{3.5}$$

for which the expansion of Eq. (3.3) is of first order. The transition occurs between the initial state $|\phi_i\rangle$ with the energy E_i to the final state $\left\langle\phi_f\right|$ with the energy E_f. It is promoted by the transition operator $\hat{T}$, which can be represented in real and reciprocal space. The dipole approximation implies the dipole selection rules Δl=$\pm$1, Δm_l=0,$\pm$1 and Δm_s=0.

A simplification can be applied if the transitions can be understood in a single particle picture. In the sudden approximation, the final state is assumed to be almost unaffected by the excitation and is therefore identical to the initial state. Then, the orbitals in the initial state are unchanged upon excitation to the final state and a single electron picture can be applied. Instead of employing

[2] This particular form assumes a gauge invariance of $\nabla\cdot\mathbf{A} = 0$

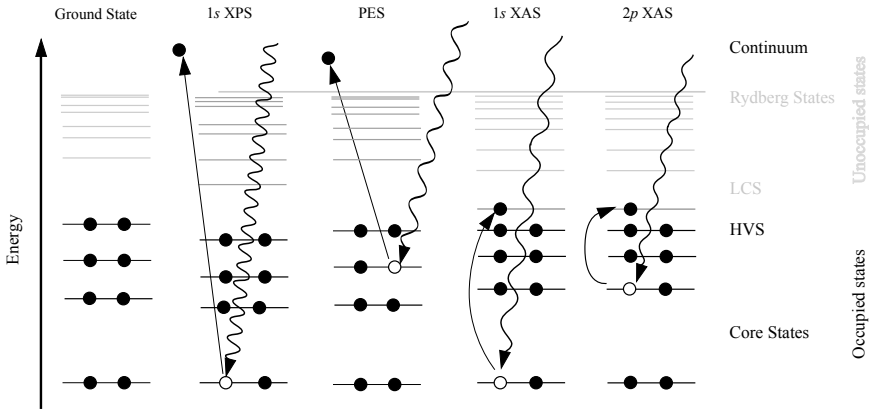

Figure 3.1. Illustration of the ground state energy level, the ionization process via XPS excitation, the PES related ionization of valence electrons and the electron transition from an occupied to an unoccupied orbital during XAS excitations. The core state, highest valence state (HVS) and the lowest conduction state (LCS) are depicted. Electrons are shown as filled and holes as empty circles.

the full wave function, the transition probability can be expressed in terms of the initial one-electron orbital $|\varphi_i\rangle$ and the final state $|\varphi_j\rangle$ as

$$w_{SP} = \frac{2\pi}{\hbar}|\mathbf{E}\langle\varphi_j|\hat{T}|\varphi_i\rangle|^2\delta(E_i - E_f + h\nu). \tag{3.6}$$

Photoelectron spectroscopy

In Photoelectron spectroscopy (PES), an atom in a material is ionized by the absorption of photons via the photoelectric effect. The final state of the system in Eq. (3.4) is described in this case by a free electron. The process can be explained with different models, like the one-step model which we have considered in the present work. When illuminated with photons of energy $h\nu$, electrons in the orbital $|\varphi_i\rangle$ with binding energy E_i can absorb a quantum of energy. As known from the photoelectric effect, the photon energies need to be larger than the binding energies (plus the work function) to be able to excite the electrons. When the electrons are excited to become free electrons, the system is ionized and a vacancy, e.g. a hole, is left. Figure 3.1 illustrates the process. Following the energy conservation, and neglecting secondary processes like satellite excitations etc, one obtains the following equation

$$h\nu = E_{kin} + E_i + \Phi. \tag{3.7}$$

with E_{kin} the kinetic energy of the free electron after it has left the system and Φ the work function. When the photon energy, e.g. wavelength Eq. (2.1), and

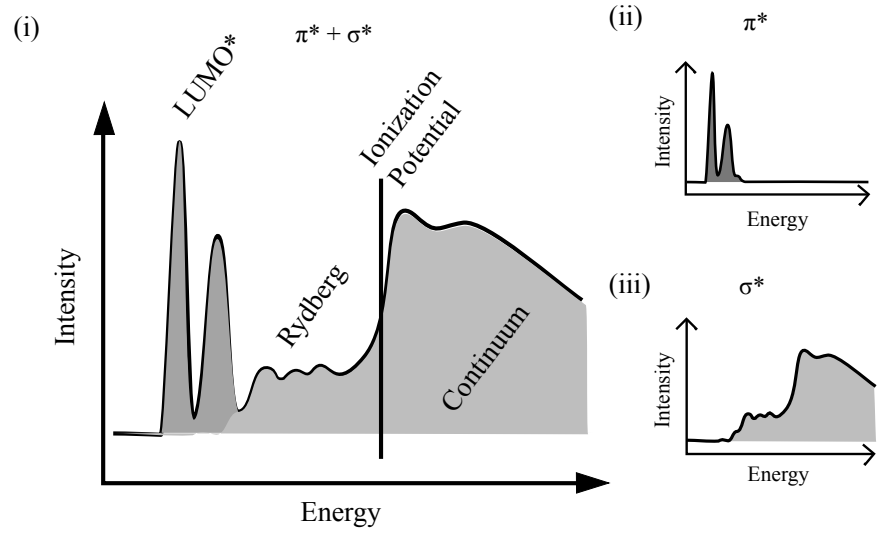

Figure 3.2. Illustration of the idealized π^* and σ^* transition probability. (i) shows that total spectrum; equivalent to disorder, (ii) shows the π^* and (iii) the σ^* transitions probabilities.

the work function are known, the binding energy is obtained by measuring the kinetic energy of the expelled electron.

PES can be used to excite any electron in the system, from valence to core states. However, to excite the valence states even photon sources of low energy can be used, like UV sources, while to excite core levels soft X-rays need to be used (hard X-rays in case of core excitation of electrons with BE of some thousands of eV). In the cases when X-rays are employed as an excitation source, the experimental technique is usually called XPS. The valence electrons have binding energies of just a few eV and are crucial for understanding important properties of a material, like the chemical bonds, the conductivity and electrical, magnetic and optical properties that determine the possibility to employ a certain material in practical applications. The core-electrons have much larger binding energies. Due to the influence of the large Coulomb attraction between nucleus and core electrons, the difference between binding energies of different elements is large and the XPS technique can therefore provide element specific information and is routinely applied in surface science [90]. The ionization process of XPS is illustrated in Figure 3.1. The key advantage, which goes back to the development by Kay Siegbahn[3] from Uppsala University, is the sensitivity of XPS peaks to the chemical environment of the atoms.

[3] He received the Nobel Prize in 1981 for his contributions to high-resolution electron spectroscopy.

1s XPS

The differences in the chemical environments surrounding different atoms produce shifts in the binding energy of up to a few eV called core level shifts. These variations in the BE are caused by charge transfer effects, or by different binding potentials, in connection to adsorbate-substrate topographic or structural changes [91, 92]. This is the type of information which one can obtain by the XPS of the 1s electrons.

2p XPS

The excitation of 2p core electrons, for example in 3d transition metals like Fe or Co, underlines a more complex process with respect to the 1s electrons. A characteristic feature of the 2p XPS is the splitting of the core-level lines. The splitting can be explained with the spin-orbit coupling taking place in the 2p subshell in the final state. Since one electron is unpaired, the moment of an unpaired 2p electron can couple to the orbital moment and, due to the proximity of the nucleus, the spin-orbit coupling is strong. Therefore, the line shape of 2p XP spectra splits into two well separated peaks with branching ratios of 2 to 4 corresponding to the $2p_{1/2}$ and $2p_{3/2}$ components, respectively. Due to the wave function overlap between 2p and 3d states, the simplification of the single particle approach is not valid to understand the transitions and a wave function based approach considering the multiplets of the d states must be applied [93]. The complexity of the process causes more complicated spectral profiles with respect to the 1s XPS, which are more difficult to interpret in terms of electronic states involved.

XAS and NEXAFS

XAS is another very important spectroscopic technique, where, in contrast to XPS, the system remains electrically neutral. In fact, in XAS unlike in XPS, the excited electron is promoted into an unoccupied orbital and does not leave the system [93]. Due to the dipole selection rules, specific information on the unoccupied electronic states can be obtained, and the orientation of the electronic orbitals are accessible. The XAS experiment is carried out by scanning the photon energy within energy windows, since due to the energy conservation, only certain photon energies can cause a resonance. When the photon energy is close and below the ionization threshold, also called transition edge, XAS is referred to as Near Edge X-ray Absorption Fine Structure (NEXAFS) spectroscopy [94], and this is the technique which is related to the studies presented in this thesis. At larger energies, scattering effects can occur and at this energy region XAS is referred to as Extended X-ray Absorption Fine Structure (EXAFS).

According to the shell structure of the atomic orbitals, core-level excitations can be divided into different adsorption edges, following the notation by Charles G. Barkla [95]. Excitations from the 1s orbital are addressed as K-edge excitations, e.g. n=1. With increasing n, the excitations edges follow the alphabet, e.g. L, M and so on.

K-edge NEXAFS

K-edge NEXAFS spectroscopy probes the transition of a 1s electron into an unoccupied p-like orbital. Information about the unoccupied states in the presence of a core-hole can be obtained with this technique. One of the key features of K-edge measurements in planar organic molecules containing C and N atoms is the ability to extract information about the orientation of unoccupied orbitals [96]. This can be easily seen when the transition operator $\hat{T}$ is written in real space where it acts as $\mathbf{r}$. Due to the selection rules, if the transition is at the K-edge, e.g. from a 1s orbital, the final state orbitals must be of the p-type. This can be seen from the dipole selection rules which dictate that the orbital momentum must change as $\Delta l = 1$. The p-type orbitals have three different directions (p_x, p_y and p_z), but can also hybridize with the 2s, forming different types of bonding geometries. By selecting the polarization vector of the incoming light $\mathbf{E}$ in a certain polarization plane and expressing the transition operator in terms of $\mathbf{r}$, a direction selective excitation process follows according to $\mathbf{r} \cdot \mathbf{E}$ in Eq. (3.6).

This property is often employed to investigate the orientation of molecular bonds. In planar molecules, like phthalocyanines, generally the lower unoccupied orbitals are directed perpendicular (π^*) to the molecular plane. The unoccupied in-plane states are even higher in energy (σ^*) giving the spectra a characteristic profile: an illustration of this can be found in Figure 3.2. If adsorbed on substrates, the K-edge NEXAFS can be employed to determine whether the molecules form ordered and quasi-ordered architectures.

In 1s NEXAFS, the focus is on those electronic states below the ionization edge, see Figure 3.2 which gives a sketch of a NEXAFS spectrum for a molecular system. As shown in Figure 3.2 (i), a NEXAFS spectrum has distinct regions below the ionization edge. The first peak of the spectrum corresponds, when allowed by the selection rules, to a transition into the LUMO, and further peaks correspond to transitions into higher lying orbitals with high principle quantum numbers, the so-called Rydberg states. Above the ionization edge, the spectra represent several effects such as multi-scattering processes with excitations into the continuum. The excitations between orbitals above HOMO and the Rydberg states have long life times and sharp excitation peaks while the short lived structures on the continuum are much broader [94].

L-edge NEXAFS

L-edge NEXAFS probes the transition of a $2p$ electron into an unoccupied state in the $3d$ shell according to the dipole selection rules. This technique is in particular useful to study, for example, transition metal compounds like oxides or molecules such as enzymes and metal-organic complexes [97, 98]. In many cases, the electronic properties can be altered if the transition metal is exchanged or the electro-magnetic surrounding is modified. This contributes to understanding the physics of these systems. Since they have many applications in technological and biological fields such as in solar cells, drugs design and molecular electronics, gaining insights into electronic structures from $2p$ XAS experiments may lead to further developments and achievements.

The electrons in the d-shell have a strongly correlated behavior due to spatial confinement effects and this results in the multiplet features seen in the NEXAFS spectra. In contrast to the K-edge, a single-particle picture cannot be applied to interpret the spectra. The final states of the $2p$ XPS and XAS have the core-hole in common. The L-edge signal has for the same reason two components, L_3 and L_2, which are a consequence of the spin-orbit coupling of the hole. The branching ratios can be very different from the static 4:2 ratio in XAS [93], which is a consequence of the dipole selection rules; in particular $\Delta m_l = 0, \pm 1$ is relevant and details depend on the electronic structure. The latter can be subject to crystal fields, charge transfer and ligand effects [93].

Like for the K-edge, also in for the L-edge further information can be obtained from polarized light interacting with the sample. In particular, the use of circular polarized light is important since it is used to obtain information on the magnetic properties of a sample [99].

4. Theoretical modeling of spectra

4.1 PES

In a rough approach, PE spectra can be computed with the sudden approximation stating that the expulsion of an electron is instantaneous and the other electrons of the system do not have time to relax. Nevertheless, identifying the Kohn-Sham eigenvalues with the valence band spectra can be in reasonable agreement for many systems. However, depending on the functional, the positions of the eigenvalues can differ and therefor the results of PES computations depend on the functional used.

Another approach includes the electronic relaxation of the remaining electrons in presence of the hole, the so called ΔSCF calculations. The binding energy of an electron can be expressed as

$$E_{SCF} = E_{N-1} - E_N \tag{4.1}$$

where E_N is the total energy of the system with N electrons and E_{N-1} is the system where one valence electron has been removed. In practice, this method is applied to obtain the ionization energy, as it is employed, for example, in the OT-RSH ansatz in Eq. (2.11).

4.2 *The* GW approach

In many cases, the description of the valence band and of the excitations from the valence states, obtained by DFT methods need to be improved, and more accurate methods are being developed. It is well known that the direct comparison of Kohn-Sham eigenvalues with, for example, experimental PES data does not necessarily provide good agreement. A well-known example is of course the infamous band-gap problem, as Kohn-Sham band gaps are normally underestimated by 30-50% [100]. This issue is also present in Koopmans' theorem. The theorem states that the first excitation energy in the restricted Hartree-Fock approximation is equal to the eigenvalue of the first orbital. However, this is based on the frozen orbital assumption in which the orbitals of the ion are the same as those of the neutral system. However, neglecting the relaxation effects might lead to large discrepancy from the experiment. Fortunately, the framework of many-body approaches can provide an accurate description of excitations.

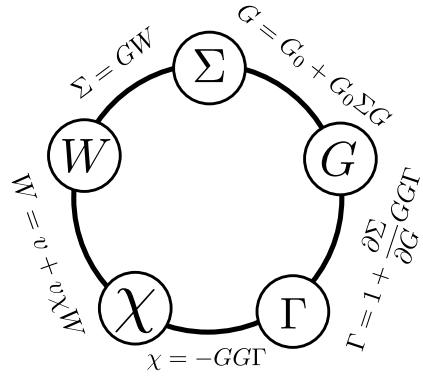

Figure 4.1. Hedin's wheel

Many-body perturbation theory (MBPT) techniques have been a successful alternative/extension of DFT calculations to obtain excited state properties; in particular by employing the Green's function approaches to describe the propagation of electrons. The Green's functions have not only an easy to grasp physical interpretation, but also represent a theoretically well-motivated and systematic approach to the excited state problem [101]. Within this framework, excitations of electrons are generally expressed as transition amplitudes linked to the propagation of electrons in an interacting system of electrons.

In 1964, Lars Hedin formulated a method to evaluate the self-energy Σ of the high-density electron gas, e.g. of a metallic system [102]. The self-energy, a non-local, frequency-dependent and non-Hermitian operator, represents the complicated electronic correlations containing all information of the many-body interactions between the N electrons in the system, though the calculation of Σ is a non-trivial task. Hedin's proposed perturbation method contains a set of five self-consistent equations, which can be given as the so-called Hedin's wheel shown in Figure 4.2. It is based on the expansion of Σ in terms of the full Green's function G and the dynamically screened potential W [103].

The wheel begins with the construction of the Green's function G in terms of the non-interacting Green's function G_0 and Σ in the Dyson equation (4.2)

$$G = G_0 + G_0\Sigma G. \tag{4.2}$$

The Dyson equation expresses the connection between the non-interacting and the interacting system. In this context, G_0 and G are referred to as bare and dressed Green's function. Their poles correspond to their quasiparticle energies. As shown in Figure 4.2, G and Σ are used to compute the vertex function Γ, the response function χ, which is also known as polarizability, and the screened potential W to eventually evaluate Σ. The explicit equations of Hedin's wheel are given in the Appendix A. The key features are briefly discussed in the following paragraphs. When the Green's function is constructed, in principle the only further needed term is the dynamically screened potential

W, containing most of the physical phenomena of the GW approach (GWA). The screened potential is evaluated in a Dyson-like equation

$$W = v + v\chi W. \tag{4.3}$$

and it appears dressed compared to the bare potential v due to the polarizability[1] χ. The resulting interactions can be understood as those of a quasiparticle, here an electron dressed by a polarization cloud [103, 104]. While the electron is repelling other electrons, it creates an attractive surrounding around it, the exchange-correlation hole, with an effective positive charge [20] which screens the bare Coulomb repulsion. The polarization cloud together with the electrons is the quasi-particle. The equations in Hedin's wheel have to be solved self-consistently which can be rather involved.

In the GWA [31, 102, 105], the set of self-consistent integral equations is simplified through the truncation of Hedin's wheel. This is achieved by simplifying the functional definition of Γ as Γ^{GWA}=$\delta(1,2)\delta(1,3)$ [102, 106]. As a consequence, electron-hole interactions are neglected and the polarizability is evaluated in the RPA [107]. The dynamically screened potential and consequently the self-energy are also affected. Eventually, Σ can be expressed in the form

$$\Sigma(12) = iG(12)W(12) \tag{4.4}$$

where the integer used indicates the coordinates in space $\mathbf{x}$ and time t, for instance 1=($\mathbf{x}_1$,t_1). This gives the GW method its name. It might be noted that replacing W with v in Eq. (4.4) represents the Hartree-Fock equation.

In practice, the Green's function is constructed from Kohn-Sham wave functions and eigenvalues as unperturbed G_0. Alternatively, the ones from Hartree-Fock calculations can be used. The initial self-energy is set to zero, causing the use of G_0 in the evaluation of χ and W. The latter is then referred to as RPA screened potential W_0. The resulting Σ is given by the so-called G_0W_0 method, which is used in most practical computations. Then actually, Γ corresponds to the non-interacting case and in this sense the GWA corresponds to the evaluation of the complete wheel for the non-interacting case, at least for the first iteration. The set of self-consistent integral equations in the G_0W_0 method is shown in Figure 4.2.

The self-energy is used to determine the quasiparticle energy ε_i^{GW} via a correction of the underlying DFT eigenvalue ε_i for each state $|\Psi_i\rangle$. If the difference between the exchange-correlation potential and the self-energy is small [108], the quasiparticle energies ε_i^{GW} can be written as corrections of the Kohn-Sham eigenvalues by Σ, Eq. (4.5)

$$\varepsilon_i^{GW} = \varepsilon_i + Z\Re(\langle\Psi_i|\Sigma(\varepsilon_i) - v_{xc}|\Psi_i\rangle) \tag{4.5}$$

[1] also known as density response function

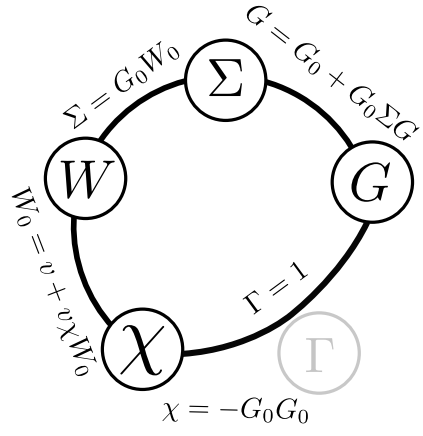

Figure 4.2. Hedin's truncated wheel in the G_0W_0 method.

where the contributions of the exchange-correlation potential v_{xc} are replaced by the self-energy. Since the self-energy accounts for the many-body effects, the DFT exchange-correlation contributions to the energy need to be removed. The renormalization factor Z arises from the perturbation ansatz of the GW correction to the Kohn-Sham eigenvalues ε_i.

The DFT starting point

Since GWA was formulated for the interacting G but in contrast the non-interacting G_0 is employed in G_0W_0, the question of the implicit consequences arises naturally. G_0 is constructed from DFT eigenvalues and wave functions. However different functionals like LDA, GGA and hybrids can be used. While the G_0W_0 ansatz yields often very accurate results, the dependence on the DFT starting point is too strong in many cases. Then, a *one-shot* G_0W_0 calculation is not sufficient and self-consistent GW calculations [109, 110] can achieve better accuracy. Especially for molecules, considerable improvements are obtained through self-consistent calculations [100, 111, 112].

Self-consistent GW methods

The dependence on the starting point can be reduced by performing self-consistent GW calculations. Different self-consistent schemes for GWA have been proposed [100, 109–112]. Either updating the Green's function or the screened potential in so-called GW_0 and G_0W calculations, or updating both in scGW. On the other hand, the way G and W are updated can also follow different methods. Since the quasiparticle energies and wave functions can be

obtained [113, 114] via

$$(\hat{t} + v_{ext} + v_H)\Psi_i(r) + \int d^3r' \Re(\Sigma(r,r'))\Psi_i(r') = \varepsilon_i^{GW}\Psi_i(r) \tag{4.6}$$

where $\hat{t}$ is the kinetic energy operator. Then, quasiparticle energies and wave functions, can be determined self-consistently [100] via restarting the evaluation of Σ. The simplification in the vertex function, however, can result in difficulties within self-consistent GW cycles. Also the RPA ansatz is strictly speaking only valid for metals while with increasing fundamental gap, a certain ambiguity is introduced [107].

One way to update G and W is to replace the eigenvalues used to construct them with the new self-energy corrected eigenvalues. Equation (4.5) gives insights on how it can be performed. The residuals between the many-body effects are reduced by each iteration. Of course, after the first iteration the exchange-correlation potential drops out and the quasiparticle energies are updated through the self-energies. The updated eigenvalues reenter the start of Hedin's truncated wheel in the next iteration. Then the new self-energy is obtained. This is repeated until convergence of the self-energies is reached. Since the wave functions are kept constant, the density remains the same. In another approach both, quasiparticle wave function and eigenvalues, can be updated. The quasiparticle equation (4.6) allows to obtain ε_i^{GW} alternatively to Eq. (4.5). Then, the quasiparticle wave functions and eigenvalues are updated. However, due to the missing vertex function, the obtained results have to be interpreted carefully.

4.3 Optical absorption - the Bethe-Salpeter equation

"If I could remember the names of all these particles, I'd be a botanist."
– Enrico Fermi

In PES measurements, information about a materials is extracted by removing an electron from it. This is caused by the adsorption of a photon with a certain energy. Additional information can be gained if the excitation energy is not sufficient to separate the electron from the materials. In that case, the excited electron is propagating into an unoccupied or virtual orbital still belonging to the same material. In this neutral kind of excitation, involved correlation effects can occur [115, 116]. Photons in the visible and UV range can promote an electron from valence levels to unoccupied levels.

The interplay between the excited electron, the left-behind hole and the remaining electronic system causes screening effects. They are the main contributors to its observable physical effects [117]. In particular bound excitons can form [107]. In general, no strict convention is established to differentiate between excitons and bound excitons [107, 118], here however the bound

exciton [107, 114, 117–120] is an electron-hole state forming within the fundamental gap, while an exciton can also exceed the fundamental gap.

In general, absorption in the optical energy range, with a photon with wavelengths of c:a 380 to 750 nm and the resulting excitations caused by it, are an essential part of life as we know it. Most commonly known examples occurring in nature might be the photosynthesis process [121, 122], but also in technological applications such as organic solar cells [123], quantum dots [124–127] and LEDs [128], energy harvesting and conversion [129–133], quantum information [126, 134, 135] and other optical technologies [134–136].

A general theory to describe these excitations is given by linear response theory. The absorption spectrum can be understood as response to an external field E_{ext} influencing the density $\rho(r)$. How much the density is consequently changed is described through the macroscopic dielectric function ζ_M [137]. The macroscopic dielectric function ζ_M connects the external field E_{ext} to the field E inside a material

$$E(r,\omega) = \int dr' \zeta_M^{(-1)}(r-r',\omega) E_{ext}(r',\omega). \tag{4.7}$$

From an atomic point of view, this can also be related to the microscopic dielectric function. The latter ansatz has the advantage that the microscopic dielectric function is accessible through DFT calculations [138] . In detail, the microscopic electric field e can be expressed as

$$e(r,\omega) = \int dr' \zeta^{-1}(r,r',\omega) E_{ext}(r',\omega). \tag{4.8}$$

with the dielectric function ζ. Then, ζ is related to the reducible polarizability χ [139], already known from the previous chapter, via

$$\zeta^{-1}(r,r',\omega) = \delta(r,r') + \int d^3r'' v(r,r'') \chi(r'',r',\omega). \tag{4.9}$$

It turns out that the interaction of the photon field with a material can be understood as perturbation of the electronic state caused by an external field and the optical absorption spectra can be computed as imaginary part of the macroscopic dielectric function [114]. On a length scale much larger than the atomic distances, the macroscopic dielectric function can be expressed as the reciprocal head of the inverted microscopic dielectric function.[2] Here it might be noted that the macroscopic dielectric function ζ_M can be calculated with and without local field effects [138]. Local fields effects express the dependence of the electronic response on the local electronic properties [113]. While the slowly varying field of the photon[3] has no effect on the microscopic properties

[2] That simply means, if both are represented in reciprocal space through a Fourier transformation, the non-locality (r,r') in ζ is reflected in a dependence on different reciprocal vectors G and G'. The reciprocal head of ζ is at G=G'=0.

[3] compared to the dimensions of typical systems

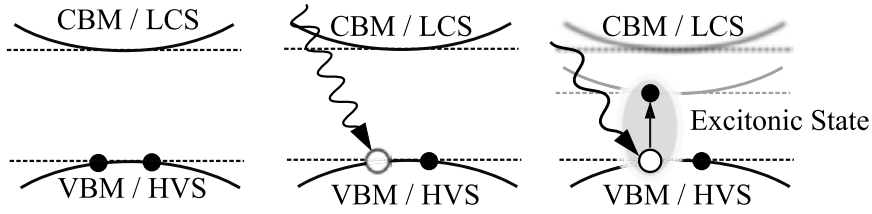

Figure 4.3. Illustration of the electron-hole interaction; while no hole is in the ground state (left), a valence hole can be created be PES in the highest valence state (HVS) and described by GW (middle), but only if the excited electron remains in the system, it can interact with the hole and form an excitonic state (right).

of the homogeneous electron gas [138], the density response can show large local fluctuations in systems with anisotropy in the induced density, [138], the so-called local field effects. Especially for systems of low dimensionality, local field effects can result in blue shifts and feature reorganization in adsorption spectra [113].

The main question remaining is how to compute the microscopic dielectric function. The RPA ansatz as used in the GWA, e.g. the evaluation of the polarizability as if the electrons were non-interacting to the total effective field [104], can be successfully used to compute absorption spectra for metals, since the screening at the fermi surface suppresses the formation of excitations [107]. Then the electron-hole interactions can be neglected. In semiconductors and insulators, the RPA is less successful since the response functions related to the external perturbation cannot any longer be understood as an effect represented by independent particles [140, 141]. Then, since the electron-hole interactions were neglected in the GWA, e.g. Γ^{GWA} is used, often agreements with optical absorption experiments are not satisfying. In optical excitation processes where the left-behind hole is not completely screened by other electrons as it can occur in semiconductors and insulators, the electron, which is propagated into a valence state, is attracted by the hole. Consequently, electron-hole interactions need to be taken into consideration [107]. This situation is depicted in Figure 4.3, in which the formation of a bound exciton within the fundamental gap is shown.

The Bethe-Salpeter equation (BSE) can be seen as natural MBPT extension of the GW approach to a two particle scheme by a second iteration in Hedin's wheel [142]. Then, the polarizability χ, or also called the density correlation function $L(1234)$, goes then beyond RPA and takes explicitly the interaction between the excited electron and the hole into account through a screened nonlocal potential W. In detail, the four-point electron-hole correlation function can be expressed as

$$\begin{aligned} L(1234) &= L_0(1234) + \\ L_0(1234)\,(v_x(57)\delta(56)\delta(78) - W(56)\delta(57)\delta(68))\,L(7834) \end{aligned} \tag{4.10}$$

where 1(3) and 2(4) describe the propagation of an electron (hole). This is known as Bethe-Salpeter equation [142]. L(1234) includes the evaluation of the vertex function but it neglects higher order terms in W. In the end, including the vertex correction in L(1234) includes effectively exchange (v_x) and the electron-hole screened attraction (W) and corrects the dielectric function [120]. Therefore, the Bethe-Salpeter equation can capture correctly the bound excitonic states and the change in the absorption strengths in optical absorption spectra associated to excitonic contributions [107].

It was shown that Eq. (4.10) can be transformed into an effective BSE Hamiltonian [120] H_{BSE} written as

$$H_{BSE} = h_e + h_h + v_H + v_x \tag{4.11}$$

where h_e and h_h refer to the single particle electron and hole states, which are coupled through the direct term v_H and the exchange contributions v_x. The latter two terms, which are doped in the Tamm-Dancoff approximation known from TDDFT, result in electron-hole coupling while the former two correspond to the resonant part of the Hamiltonian. Effectively, this translates into an eigenvalue problem [120]. The imaginary part of macroscopic dielectric function ζ_M represents the absorption spectrum. It is evaluated as a function of the effective Hamiltonian and the dipole operator. The absorption spectrum can be finally expressed as

$$\Im(\zeta_M(\omega)) \propto \sum_{\lambda} |\sum_{\alpha\beta} A^{\lambda}_{\alpha\beta} \langle\beta|\hat{T}|\alpha\rangle|^2 \delta(E^{\lambda} - \omega) \tag{4.12}$$

where the summation over the initial states $|\alpha\rangle$ and $|\beta\rangle$ with the energies ε_β and ε_α runs in the case of periodic system implicitly over k-points, too. $A^{\lambda}_{\alpha\beta}$ are the transition amplitudes computed as the overlap between the eigenstates of Eq. (4.11) in an electron-hole basis and E^{λ} are the eigenvalues of H_{BSE}. The transition elements are evaluated in the dipole approximation with the corresponding operator $\hat{T}$. Equation (4.12) resembles to some extent the Fermi golden rule, Eq. (3.4), but considers also excitonic effects.

In practice, the GW corrected eigenvalues ε_i^{GW} for the states of the holes and electrons enter the diagonal of H_{BSE}. The statically screened potential W_s is employed in the direct term. Therefore, GW and BSE calculations are frequently combined in a GW+BSE approach.

Bright and dark excitons

So far, optically active excitons, the so-called bright excitons with a finite transition amplitudes $A^{\lambda}_{\alpha\beta}$, were considered. Their excitations follow the dipole selection rules and they have finite and system-dependent lifetimes typically in the order of 10^{-12} to 10^{-9}s [143]. Another category of excitons are optically inactive excitons, the dark excitons [124, 134, 144–147]. Considering

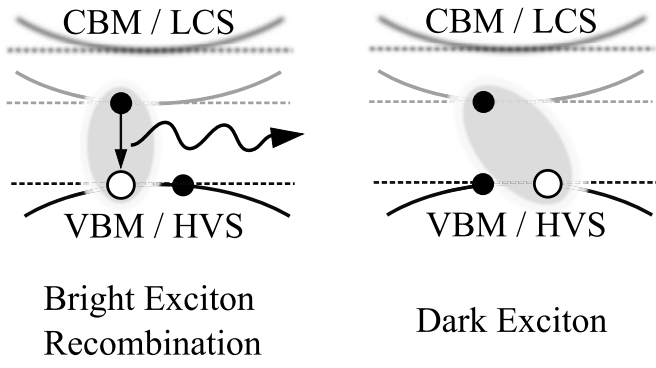

Figure 4.4. Illustration of a bright and a dark exciton. Filled (empty) circles represent electrons (holes). In the left case the electron and hole can recombine and emit a photon. In the right case, the recombination is Pauli forbidden since excited electron and the electron in HVS have the same spin.

the situation depicted in Figure 4.3 where the excited electron of the exciton formed by a transition from the highest valence state (HVS) to lowest conduction state (LCS) is shown, the recombination of hole and electron is allowed as long as both electrons have opposite spin. However, the spin of the excited electron can be changed [145]. Then the recombination is Pauli forbidden and the exciton is optically inactive, e.g. a dark exciton. The lifetime of the dark exciton at 0 K is directly linked to the time the spin needs to flip back. In realistic systems with non 0 K temperature, additional effects like scattering events with phonons [143] can reduce effectively the lifetime by introducing further non-radiative decay channels.

The dark excitons are extremely fascinating due to their lifetimes in the order of microseconds [134] which can open up for some interesting technological applications. Examples of the latter are the coherent writing and reading of states in quantum dots [126, 134, 135].

Excitons in low dimensional materials

Of particular interest are materials with low dimensionality, for example 2D networks, 1D nanowires and and 0D quantum dots [134, 148]. It was shown, that they can inhibit particular promising excitonic characteristics [115, 116, 149]. Large exciton binding energies are one of them. They are essential to observe and finally employ excitons in any kind of application. In particular, the exciton binding energies should be large compared to the thermalisation energy which is in the order of 25 meV at room temperature. While this energy is not drastically exceeded in many bulk semiconductors [140], exciton binding energy in most 2D materials is much larger than 25 meV [150–161]. Figure 4.5 illustrates the electronic interaction between an excited electron and

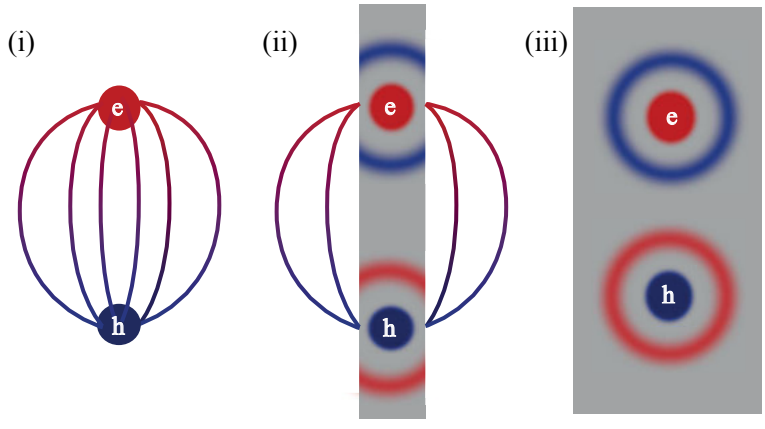

Figure 4.5. Illustration of the direct term screening between electron (e) and hole (h) in materials of different dimensionalities; for a electron-hole pair being not screened in (i), (ii) in a 1D (2D) material being partly screened and (iii) for the case of complete screening in, for example, a metal. Within the gray areas, red areas represent charge accumulation and blue areas represent charge depletion.

a hole. If they are less screened, the resulting electron-hole interaction is consequently stronger, leading to larger binding energies. Similar effects can be found in 1D materials like nanotubes, -wires and -chains as well as quantum dots [115, 116, 149].

4.4 The transition potential - a *K*-edge NEXAFS approach

The 1*s* NEXAFS spectra are often satisfyingly computed within a single particle picture. Actually, the core-hole can cause strong relaxation effects and the sudden approximation might not be the best choice. But a full treatment is computationally very demanding since the spectra representing transitions into states of the unoccupied electronic structure would consist of a huge number of transitions to match the energy window of a few tens of eV which are usually used in experiments according to equation (3.4). A very successful approximation for this issue is the Slater transition potential [162]. It allows handling the problem in a single particle picture and simultaneously accounts for electronic relaxations during the core level excitations. It has been successfully applied to many systems [60, 163, 164].

In this single particle approach, the effects of electronic relaxation are taken into account by replacing a fully occupied orbital $|\varphi_i\rangle$ with a half-occupied orbital, e.g. the charge of one electron is replaced by half the charge of an electron, in the performed self-consistent field procedure. The remaining electrons experience an increased potential of the nucleus on the excited site. This re-

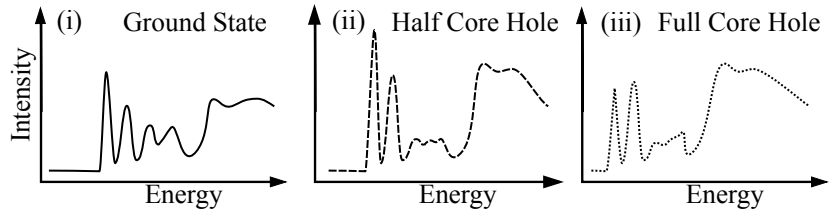

Figure 4.6. Comparison of the effects of the core-hole size, e.g. shifts to lower energy and feature reorganization, on the unoccupied electronic structure for (i) the ground state, (ii) the transition potential (half core hole) and (iii) full core hole calculations after electronic relaxation.

sults in a downwards shift of the entire unoccupied electronic structure towards lower energies which is accompanied also by changes in the structure of the density of states, see Figure 4.6 (ii). The energies of the electronic levels are even more shifted to lower energies if the half occupied orbital is replaced by a fully unoccupied orbital, see Figure 4.6 (iii). The latter full-core hole approach has been successfully applied in some cases when different core-hole screening effects need to be modeled [165, 166].

Not all transitions from occupied to unoccupied orbitals are possible due to the dipole selection rules. If polarized X-ray beams are used, only transitions with non-vanishing projections of the field vector $\mathbf{E}$ with the transition operator $\mathbf{r}$ contribute to the resonances, e.g. components which also satisfy the condition $\mathbf{E} \cdot \mathbf{r} \neq 0$. The $\mathbf{E}$-vector can be decomposed into out-of-plane ($\mathbf{E}_\perp$) contributions, e.g. perpendicular to the molecular plane, and in-plane ($\mathbf{E}_\parallel$) contributions. When two different polarized photon beams are used in a measurement, one for in-plane polarization ($\mathbf{E}_\parallel$) and the other one for $\mathbf{E}_\perp$, two different spectra are measured that depend on the orientation of the orbitals with respect to the orientation of the $\mathbf{E}$-vector. The two different spectra correspond to the out-of-plane transition intensities

$$I_\perp \propto |\mathbf{E}_\perp \langle \phi_f | \mathbf{r} | \phi_i \rangle|^2 = \cos(\gamma)^2 |\langle \phi_f | \mathbf{z} | \phi_i \rangle|^2 \tag{4.13}$$

with γ being the angle between $\mathbf{E}$ and $\mathbf{r}$. The in-plane transition intensities can be expressed similarly

$$I_\parallel \propto |\mathbf{E}_\parallel \langle \phi_f | \mathbf{r} | \phi_i \rangle|^2 = \sin(\gamma)^2 \left(|\langle \phi_f | \mathbf{x} | \phi_i \rangle|^2 + |\langle \phi_f | \mathbf{y} | \phi_i \rangle|^2 \right) \tag{4.14}$$

and both intensities sum up to the total intensity

$$I = I_\parallel + I_\perp. \tag{4.15}$$

These two contributions can be employed to determine the orientations of molecules in ordered films.

4.5 *L*-edge NEXAFS approaches

"Before I came here I was confused about this subject.
Having listened to your lecture I am still confused. But on a higher level."
– Enrico Fermi

The calculations of *L*-edge spectra of XA measurements on 3*d* transition metal (TM) compounds must be done in a many-body approach. Due to the overlap of the 2*p* wavefunction with the 3*d* orbitals and the arising multiplet effects, single particle approaches are doomed to fail in most cases [93]. This can be seen if the density of states (DOS) is compared to experimental XAS data. This is generally most obvious in the branching ratio between the L_3 and L_2 peaks, which does not follow the statistical value.

Approaches with model hamiltonians

Based on the work of Sawatzky et al [167–169], Gunnarson and Schönhammer [170], Jo and Kotani [171] and Fujimori and Minamo [172], a model Hamiltonian approach similar to the Single Impurity Anderson model (SIAM) [173] is today a frequently used method to obtain insights into XAS measurements [174–176]. The SIAM describes the physics of a local problem. It has the advantage to consider the interaction with ligand states which can be large in 3*d* TM compounds. In addition, symmetry aspects and additional charge transfer effects can be included [93]. In the case of 3*d* TMs, only the correlated *d*-orbitals and the ligand orbitals in the central field approximation enter the calculation which is performed for a local cluster. The SIAM Hamiltonian including spin-orbit (LS) coupling can be written in 2^{nd} quantization as

$$\begin{aligned}\hat{H}_{init} = \sum_{ij} \varepsilon_{3d} \hat{d}_i^\dagger \hat{d}_j + \sum_{ij} \varepsilon_L \hat{L}_i^\dagger \hat{L}_j + \sum_{ij} T_{ij}^{3dL} \left[\hat{d}_i^\dagger \hat{L}_j + \hat{L}_j^\dagger \hat{d}_i\right] + \\ \sum_{ijkl} U_{ijkl}^{3d3d} \hat{d}_i^\dagger \hat{d}_j^\dagger \hat{d}_l \hat{d}_k + \lambda_{3d} \hat{\vec{L}}_{3d} \cdot \hat{\vec{S}}_{3d} - D.C.,\end{aligned} \tag{4.16}$$

where the indices label the orbitals, which can be either localized *d*-states (d) or ligand states (L). The creation/annihilation operators for these orbitals are $d^\dagger$ and d for the *d*-states and $L^\dagger$ and L for the ligand states with the one-particle energies ε_d and ε_L, respectively. The first term in Eq. (4.16) accounts for the crystal field effects, which can also be described by a crystal-field Hamiltonian. The crystal-field in its initial formulation is generated by the distribution of charges around the metal center. This lifts the degeneracy of the d states. In a O_h symmetric crystal field, for example, the *d*-states split into t_{2g} and e_g states which are separated by 10Dq, e.g. the crystal-field strength. With

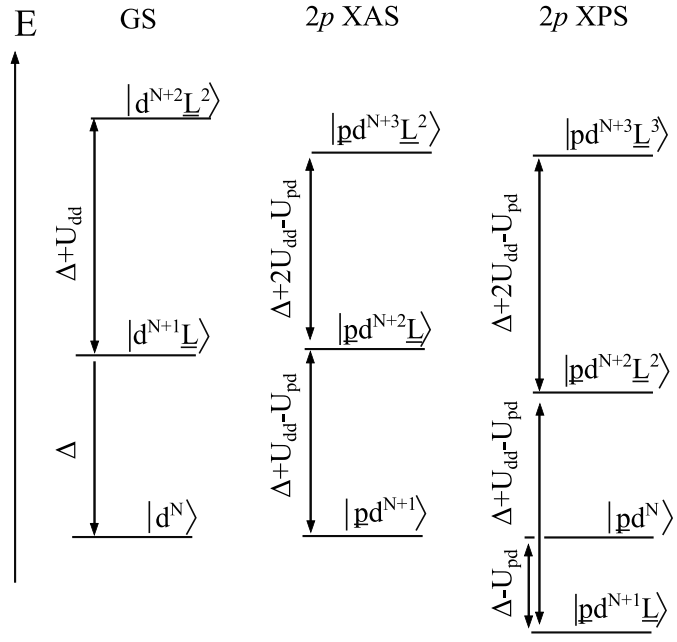

Figure 4.7. Illustration of the different configurations and how they relatete to the on-site energies U_{dd} and U_{pd} as well as the charge transfer energy Δ for the ground state (GS) and in XAS and XPS calculations. The core-hole in a p-state is denoted as $\underline{p}$. Adapted from Ref. [169].

decreasing symmetry, these two branches split further and with additional parameters, Ds and Dt, the splitting of the d-states can be described. The second term in Eq. (4.16) represents the ligands states which adopt the same symmetry as the d-orbitals [177]. The third term is the coupling between ligands and correlated orbitals in form of hopping rates T^{3dL}. The on-site correlation energy of the d-electrons in the fourth term is described by the Hubbard U-term, which can be expressed by Slater-Condon terms F^0, F^2 and F^4. Finally, the double counting (D.C.) is removed in the last term.

A configuration of N $3d$-electrons, $\left|3d^N\right\rangle$, can be represented as Slater determinant. In the charge transfer state, an electron is transfered from the ligands to an unoccupied d-orbital. The state can be written as $\left|3d^{N+1}\underline{L}\right\rangle$.[4] Both configurations are interacting via a monopole transition and their energy separation is Δ, the charge transfer energy. This is illustrated in Fig. 4.5. Considering more than one configuration is basically configuration interaction [178]. Even a state with two ligand hole can be included. This is particularly important for $2p$ XPS calculations.

Also in this approach, the transition probability between initial state and final state can be calculated according to Eq. (3.5). Since the initial state of

[4] $\underline{L}$ denotes a ligand hole

the quasiatom is defined by Eq. (4.16), the final state needs to be constructed in a similar fashion.

The final states, spanned by the configurations $\left|2p^5 3d^{N+1}\right\rangle$ and $\left|2p^5 3d^{N+2}\underline{L}\right\rangle$, are characterized by a propagated electron from the $2p$ level into an unoccupied $3d$ state. Thus, additional terms have to be considered. In the final state Hamiltonian H_{XAS}, the $2p$ states are created ($p^\dagger$) and annihilated (p) at energy ε_{2p}. A strong spin-orbit coupling, resulting in the splitting of the L_3 and L_2 components in the XA spectra, is expressed with the coupling constant λ_{2p} and the operators $\hat{\vec{L}}_{2p} \cdot \hat{\vec{S}}_{2p}$. The core-hole valence interaction between $2p$ and $3d$ states of the TM is expressed by the interaction term U_{pd}. This interaction results in the multiplet splitting [179]. Multiplets are essentially a consequence of the different overlap of a p-orbital with the d-orbitals, resulting in 6 different configurations [180]. The final state Hamiltonian can then be written as

$$\hat{H}_{XAS} = \hat{H}_{init} + \sum_{ij} \varepsilon_{2p} \hat{p}_i^\dagger \hat{p}_j + \sum_{ijkl} U_{ijkl}^{2p3d} \hat{d}_i^\dagger \hat{p}_j^\dagger \hat{p}_l \hat{d}_k + \lambda_{2p} \hat{\vec{L}}_{2p} \cdot \hat{\vec{S}}_{2p} \qquad (4.17)$$

which assumes to have the same crystal field strength and coupling to the ligands. This is approximately true since the $2p$ to $3d$ transition is almost self screened preventing a collapse of the valence wave functions in presence of the core-hole [93]. Then, the relative ordering of the configurations $\left|3d^N\right\rangle$ and $\left|3d^{N+1}\underline{L}\right\rangle$ is maintained.

Ab initio based methods for *L*-edge calculations for TMs

On way of performing $2p$ NEXAFS calculations are multi-determinant approaches solving a model Hamiltonian exactly. Nonetheless, DFT can be useful for those calculations as well. In particular, it opens an alternative path in the parametrization of the electronic interactions and solve the model problem exactly.

A variety of theoretical approaches emerged over the last years to simulate the XA spectra of the *L*-edge, one of them is to solve the Bethe-Salpeter equation. It was shown that the Bethe-Salpeter equation can be applied to compute the neutral $2p$ to $3d$ excitations in $3d$ TMs [117, 181–185]. To handle the computational demands, the manifold of initial electronic states is reduced to the $2p$ core states and the unoccupied $3d$ states span the valence manifold. However, the strong spin-orbit coupling of the $2p$ hole has to be considered and the effective BSE Hamiltonian in Eq. (4.11) must be complimented with an additional LS-term [184]. Also the multiplet effects need to be accounted for which can be achieved through additional configurations, a crystal field potential [184] or through all electron calculations [185]. In any case, it was demonstrated that the BSE ansatz can be applied to compute, among others,

the *L*-edge XA spectra of 3*d* TMs. This includes, for example, MnO, CoO, TiO_2 and CaF_2 [184, 185].

Another method that has successfully been used to compute 2*p* XA spectra is Time-Dependent DFT (TDDFT) [186–190]. The transitions from occupied to unoccupied states can be computed with TDDFT in a linear response formalism. Also a full configuration interaction is capable to capture the XAS features. Restricting the active space can reduce the computational costs, yielding the restricted active space (RAS) method [191], which has been successfully used to compute *L*-edge spectra [192, 193] of molecular systems like ferricyanide [194], similarly to combinations of DFT and configuration interaction (DFT-CI) [195].

Krüger et. al presented a method based on the a multi-channel and multiple scattering theory [196]. In particular, the Wannier-orbital approach combined with multiplet ligand-field theory (MLFT) calculations by Haverkort *et al.* has been very successful [177].

Combining the hybridization function and multiplet ligand-field theory

While the model Hamiltonian in Eq. (4.16) depends on a fitting procedure to experimental results, as an alternative insights from DFT can be employed, in principle, to give an estimate of the ground state parameters in Eq. (4.16). The crystal field splitting and the hybridization in terms of ligand state hopping can be estimated by ground state calculations. The stunning advantages are obvious if the two approaches are combined successfully: (i) the exact solution of an (ii) *ab initio* parameterized and less ambiguous, Hamiltonian (iii) with relatively low computational demands and (iv) the possibility of obtaining predictive powers and (v) of the extension to arbitrary geometry.

The theoretical approach will focus on the metal center, since the 2*p* to 3*d* transitions in TMs are of local nature. The 3*d* orbitals of 3*d* TM are fairly localized at the site of the TM. Therefore, the global problem can be simplified by constructing a local description corresponding to a single impurity. The remaining question of how the crystal- and ligand-field effects can be included into the local description will be addressed in the following.

The global Green's function $\hat{g}$ is given as the inverse of the global Hamiltonian $\hat{h}_{DFT}$ aligned at the chemical potential μ and evaluated at the frequency ω.

$$\hat{g} = \frac{1}{(\omega + \mu) - \hat{h}_{DFT}} \tag{4.18}$$

The local Green's function $\hat{G}$ is obtained at a particular site R in real space by acting with projector operators on $\hat{g}$,

$$\hat{G}_R = \hat{P}_R \hat{g}(\omega) \hat{P}_R. \tag{4.19}$$

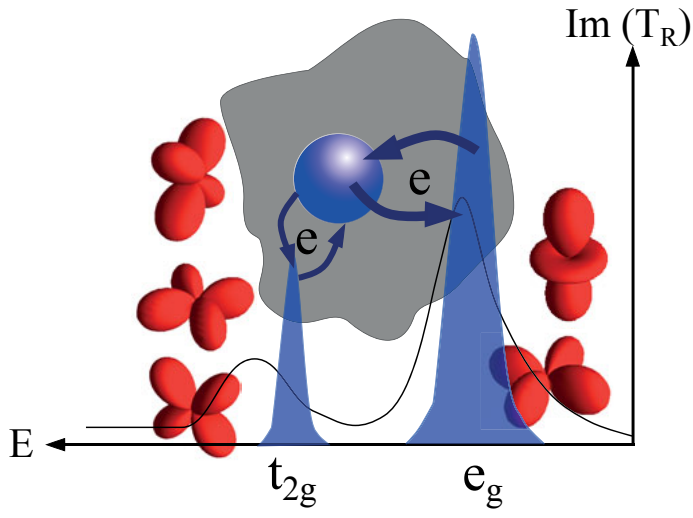

Figure 4.8. Illustration of the imag. part of the hybridization function T_R (black curve) of a metal ion in a bath. The fitted hybridization function for e_g and t_{2g} orbitals is shown as blue filled curve.

The projectors are constructed from a particular choice of correlated orbitals, e.g. d-states, represented by full-potential linear muffin-tin orbitals [197]. The resulting local Green's function $\hat{G}_R$ contains all relevant electronic information of the localized d-states for the on-site problem. Similarly, the local Hamiltonian $\hat{H}$ can be obtained by projecting $\hat{h}_{DFT}$ onto a local site R via the same projectors

$$\hat{H}_R = \hat{P}_R \hat{h}_{DFT} \hat{P}_R. \tag{4.20}$$

This Hamiltonian already contains the crystal-field splitting. With these quantities, the hybridization function $\hat{T}_R$ can be defined, which describes the difference in interactions of the isolated site R to the same site R situated in the atomic environment of the global problem

$$\hat{T}_R = \omega - \hat{G}_R^{-1} - \hat{H}_R. \tag{4.21}$$

The impurity, which can be represented by d-orbitals of a transition metal, can interact with the bath-orbitals in form of electrons hopping between both states. The bath itself mimics the electronic effects of the environment surrounding the impurity. This model is well known from Dynamical Mean Field Theory [198]. The strength of this process, e.g. the hopping probability, is expressed as the hybridization strength V known in the form

$$\hat{T}_R = \sum_B \frac{V_B^\dagger V_B}{\omega - \varepsilon_B} \tag{4.22}$$

summed over all bath states (B). In practice, $\hat{T}_R$ is fitted with at least one bath state per d-orbital. Figure 4.5 illustrates $\hat{T}_R$ for a metal ion in an environment

(bath) of O_h symmetry. The d-states are split in e_g and t_{2g} levels which have different interaction strength with the bath.

The initial state Hamiltonian $\hat{H}_{init}$ can be constructed similarly to Eq.(4.16), but the ligand orbitals are replaced by bath orbitals, a concept known from DMFT. Then the initial state Hamiltonian takes the form

$$\begin{aligned}\hat{H}_{init} = \sum_{ij} \varepsilon_{3d} \hat{d}_i^\dagger \hat{d}_j + \sum_{ij} \varepsilon_B \hat{B}_i^\dagger \hat{B}_j + \sum_{ij} V_{ij}^{3dB} \left[\hat{d}_i^\dagger \hat{B}_j + \hat{B}_j^\dagger \hat{d}_i\right] + \\ \lambda_{3d} \hat{\vec{L}}_{3d} \cdot \hat{\vec{S}}_{3d} + \sum_{ijkl} U_{ijkl}^{3d3d} \hat{d}_i^\dagger \hat{d}_j^\dagger \hat{d}_l \hat{d}_k - D.C.\end{aligned} \tag{4.23}$$

which defines the ground state problem. This corresponds to the initial state Hamiltonian in Eq. (4.17), but with bath operators/states instead of ligand operators/states which is not surprising since both are based on the SIAM. The main difference is, however, the use of the hybridization function instead of hopping parameters. Also the projection of DFT quantities enter the model Hamiltonian. The final state Hamiltonian follows simply Eq. (4.17).

Since all parameters but U_{dd}, U_{pd} and Δ are explicitly estimated in an *ab initio* fashion, this method combines the benefits of both, e.g. solving a model problem exactly with a well-motivated description of the physical picture.

The XAS intensity $I(\omega)$ can be computed as the imaginary part of the Lorentizain expressed in

$$I(\omega) = -\Im \left[\langle i | \hat{D}^\dagger \frac{1}{\omega - \hat{H}_{XAS} + i\Gamma/2} \hat{D} | i \rangle \right] \tag{4.24}$$

where the dipole operator $\hat{D}$ acting on an initial state yields a final state [199]. Γ is the imaginary offset from the real axis which results in a convolution of the transition intensities at energies ω.

4.6 Simulation of XP spectra

The binding energy shifts are closely related to charge transfer and XPS can give insights to understand charge transfer and energy level alignments at interfaces. Also information about the chemical surrounding and bonds can be obtained. [91, 92, 155, 200]. It should be noted that the theory predicts absolute energies which are at least a few eV mismatched with respect to the experiments, and this is true for all the theoretical approaches we have considered in the present work. The absolute energies, however, are less significant from a simulation perspective. What gives information, instead, are the relative binding energies, e.g. the core-level shifts, which can be simulated with an accuracy of a few meV [201]. The shape of the experimental core level spectra reflect life-time, Doppler shifts, and solid state effects, which altogether originate a broadening of the peaks. Usually in the C1s and N1s spectra of molecules like the biphenylene and the Pcs studied in this thesis, a resulting FWHM in the order of 1 eV is generally observed.

1*s* XPS

The so-called Δ Kohn-Sham approach is a method to calculate the core level XPS ionization energies, which gives far more accurate results than simply taking the frozen GS eigenvalues. The latter ones represent the initial state, while clearly also final state effects are important. Both, initial state and final state effects contribute to the core level shifts. While the former describe the contributions before the creation of a core-hole, the latter ones describe those after the creation of it. Chemical bonding is, for example, an initial state contribution while core-hole screening is a final state one. In the presence of a substrate, the surface potential and the image charge effects can also alter the binding energy shifts in XPS measurements. The binding energies also include effects due to the relaxation of the remaining electrons in the presence of the core hole. In the calculations, they are obtained by replacing the fully occupied orbital of interest $|\varphi_i\rangle$ with an (partially) unoccupied orbital and performing the electronic relaxation keeping it unoccupied [202–204]. The core-level binding energy E_B is then obtained as the total energy (Eq. 2.8) difference between the system with N electrons and the one with a hole in a core level (N-1), e.g.

$$E_B = E_{N-1} - E_N \tag{4.25}$$

which is basically the same approach as the ΔSCF method, but for core states [205].

Many DFT codes employ the frozen core [206] or pseudo-potentials, then the treatments of the core states require specialized techniques. Either specialized basis-sets like the igloo-III [207] can be applied or, in all-electron methods the core electron is explicitly described [202] or in PAW [204] the

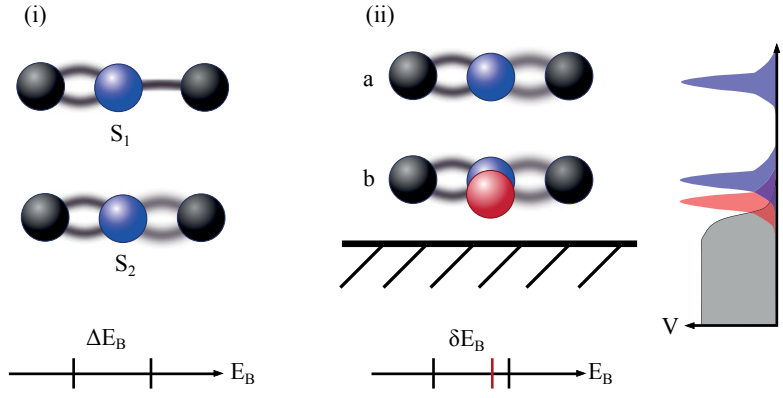

Figure 4.9. Illustration of the difference between ΔE_B and δE_B initial state contributions (see text) of a particular element (blue atom) in (i) and (ii), respectively. Note that additional structure deformation, red atom in (ii), can also cause shifts in the binding energy.

core treatment can be modified. In periodic codes, however, the core electron is either placed in a conduction state or as a uniform background charge, which then requires a supercell approach.

The core-level shift is associated with the same kind of atom in different environments. This can address a specific element in different materials or even the same atom in different conditions as, for example, before and after adsorption on a substrate. The initial state effects for those cases are illustrated in Figure 4.9. Here, both shifts are considered as ΔE_B and δE_B, respectively. They can be obtained via

$$\Delta(\delta)E_B = E_B^{S_2(b)} - E_B^{S_1(a)} \tag{4.26}$$

as difference between the binding energy before (b) and (a) after adsorption or as difference between the chemical binding at the sites S_1 and S_2. If the electronic relaxations are included in the calculations, most of the final state effects are considered.

$2p$ XPS

As for the XAS, the $2p$ XPS of $3d$ TMs cannot be computed in a single particle approach. While XAS is symmetry sensitive, XPS is a charge transfer sensitive technique [93, 208]. Therefore more than one and often even three configurations, e.g. $|3d^N\rangle$, $|3d^{N+1}\underline{L}\rangle$ and $|3d^{N+2}\underline{L}^2\rangle$ shown in Fig. 4.5, must be taken into account in the initial state to accurately reproduce experimental details. As a simplification, the multiplet ligand field theory can be modified to compute XP spectra. In the final state, the excited free electron occupies an s-orbital which is not subject to any correlation effect [93], therefore not interacting with the remaining system. Also in XPS, the different configurations

have an influence on the spectral shape of the measurement and multiplet as well as ligand effects influence the initial and final states.

5. Summary of the results

"In God we trust,
all others must show data."

– Unknown

In this chapter, the results of the conducted studies are summarized. The most significant results are highlighted and the individual studies are related to their purpose and an overall context. The studies cover experiment-theory collaborations, evaluations of theoretical methods and predictions of material's properties.

Considering that many devices employ characteristic electronic or/and optical properties of materials, a solid understanding of them is essential to further develop and improve existing technologies. Since excited states are employed in most devices to design functionality, their theoretical description is of particular importance. These excitations can be caused by, for example, photons or electrons which interact with materials. Fundamental questions can concern, for example, transport properties, interface renormalization and energy level alignment effects in different materials [209, 210]. Nonetheless, the importance of the structure should not be forgotten. This applies particularly to molecular based materials, following the simple rule that structure determines functionality.

5.1 Adsorption of the metal-free pthalocyanine on Au(111)

The study of metal-free phthalocyanine is of high importance. They can obtain a metal center through direct metalation [211] opening new possibilities to obtain molecular films. Moreover, the H_2Pc is the only phthalocyanine without a metal center. The fact that all phthalocyanines have the organic macrocycle in common promotes the H_2Pc into a fundamental role. It allows to estimate the organic contributions to the electronic structure and to the spectroscopic results. This allows also to analyse the effects of the metal center in metal phthalocyanines in relation to various physical properties, like optical response or conductivity.

In Paper I, the results of NEXAFS experiments and DFT calculations suggest that even on the weakly reactive Au(111) surface, the electronic structure

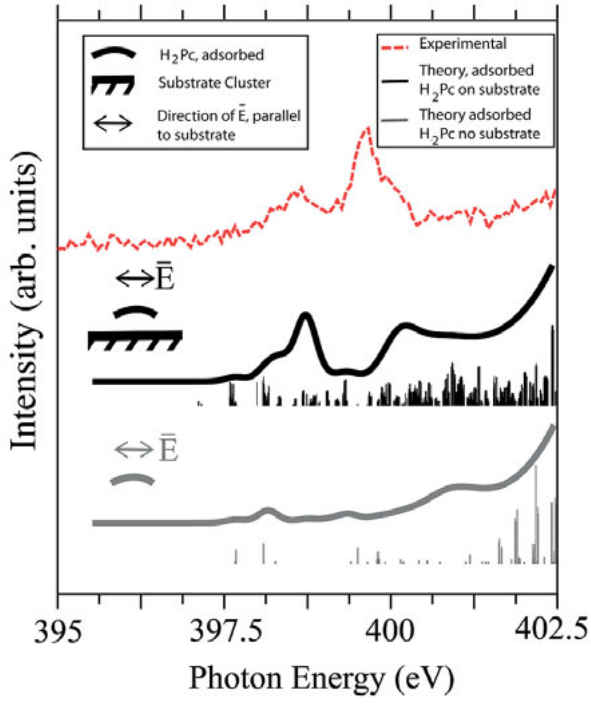

Figure 5.1. Comparison between the pre-peak NEXAFS of a H_2Pc monolayer on Au(111) with the E vector parallel to the substrate. The experiment (dashed red curve) is compared to the calculations, which include (exclude) the surface shown as black (gray) curve. After adjusting the main peak intensity, the theoretical curves were multiplied by 10 to facilitate comparison of the peak region between 395 and 402 eV. Bars indicate transition intensities according to Eq. (4.14). The figure was taken from Ref [60].

of the H_2Pc is noticeably affected by the substrate. Moreover, the molecules stay parallel oriented to the surface in thin as well as thick films. The interaction between molecule and metal was observed to affect the line profiles in the case of incident light with polarization parallel to the substrate. While the main peak is at about 406 eV, two new peaks appear in the pre-peak region in the spectra of on a monolayer of H_2Pc on Au(111). The pre-peak region is shown in Figure 5.1 in which the experiment (dashed red curve) is compared to theoretical results (solid curves). The molecule undergoes a slight deformation upon adsorption. The contribution to the pre-peak due to this deformation, gray curve, is small. Only if the surface is included in the calculations, the transition probabilities in this region increase drastically (black curve).

In order to better understand the adsorbed system in Paper II, various recent methods to include van der Waals interactions are compared for the adsorption of H_2Pc on Au(111). A precise determination of the adsorption distance, for example, can influence the results of all other properties. It was shown that the work function changes caused by the benzene molecule adsorbed on metal substrates can be correctly reproduced by DFT functionals if the adsorption distance is correct [212, 213].

Especially for weakly reactive substrates, the binding energy is often underestimated by GGA functionals [59, 214]. The Au(111) surface can be considered a weakly reactive metal surface, therefore it is an excellent system to study the vdW interactions between molecules and weakly adsorbed molecules [61, 215–219].

In the case of H_2Pc/Au(111) the adsorption energies were analysed for GGA functionals, pair-potential methods and vdW-DFs. The notation follows Chap. 2.3, while the DFT-D2 method was performed with two different C_6 coefficients labeled as PBE-D2T and PBE-D2A. Figure 5.2 shows the differences in the results between the methods. Apparently, GGAs overestimate the binding distance and underestimate to adsorption energy compared to the other methods. Evaluating the differences between the remaining methods is, however, not straight forward. Reference calculations with more accurate methods, e.g. those higher in the Jacob's ladder, do not yet exist for systems this large. Also experimental data do not exist for H_2Pc/Au(111). However, normal incident X-ray standing wave measurements of the CuPc/Au(111) determined an adsorption distance of about 3.3 Å [220]. Under the assumption that H_2Pc will be adsorbed at a similar distance, the TS and the vdW-DF provide very accurate results, while the D2 method by Grimme slightly underestimates the adsorption distance.

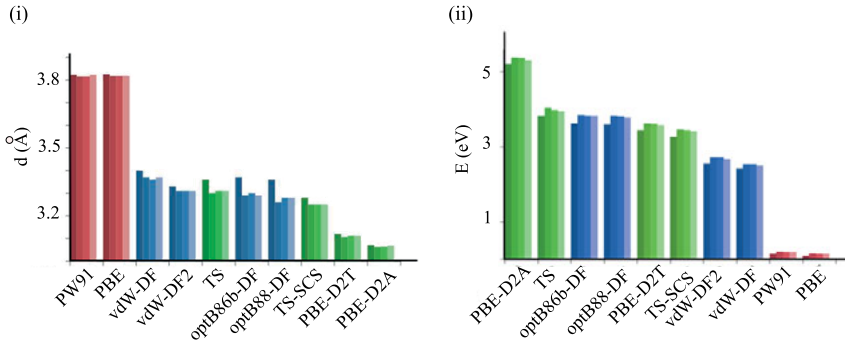

Figure 5.2. Comparison of the adsorption distance d and the adsorption energy of H_2Pc on Au(111) for GGA functionals (red), pair-potential methods (green) and vdW-DF's (blue) at different adsorption sites (shades). The figures were adopted from Ref [59].

5.2 Molecular architectures of lutetium-bis-phthalocyanine on surfaces

$LuPc_2$ is a so-called double-decker phthalocyanine with lutetium, a lanthanide, as metal center. Its structure was first determined by X-ray diffraction experiments [221]. It is compared to the DFT/B3LYP optimized structures in Figure 5.3, and the agreement between theory and experiment is rather good. Other lanthanide metals like Nd and Y are also known to form this kind of double-decker structures [222].

Differences to molecules with a single phthalocyanine ring arise for $LuPc_2$ from its low oxidation potential [223]. As a consequence, this double-decker phthalocyanine has an up to 6 times larger conductivity compared to other metal phthalocyanines [224]. In fact, $LuPc_2$ was one of the first discovered intrinsic molecular semiconductors [2] with some interesting consequences: $LuPc_2$ can change its electronic properties through adsorption of gases via reversible reduction or oxidation [225].

These properties can be used to design gas sensors [222, 226] or organic field effect transistors [227, 228]. However, there is a long way from a single molecule to a working device. Several questions need to be addressed and the mechanisms behind them need to be understood. Examples are the interaction with substrates and how it affects the architecture of molecular films, as well as how the electronic properties are affected within a film and at an interface. Investigations of molecule substrate interactions are motivated by the assumption that a working device would use some substrate. Moreover, the precise properties might be modified through the interaction with the substrate. Of particular interest for the purpose of gas sensing might be the orientation of the $LuPc_2$'s in ordered films. This will directly affect the mechanisms behind the interaction between $LuPc_2$ and gases.

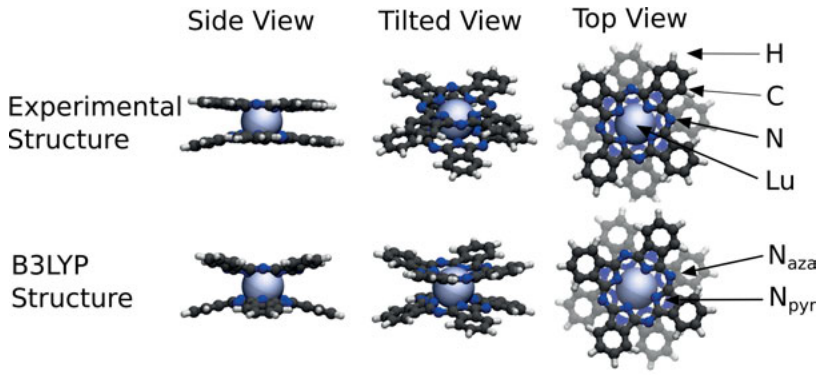

Figure 5.3. Experimental structure determined by X-ray diffraction experiments [221] on small crystals of $LuPc_2$ and its B3LYP optimized single molecule structure.

$LuPc_2$ on hydrogenated vicinal Si(100)2×1

In Paper III, a combined experimental and theoretical study was performed to investigate the molecular film of $LuPc_2$ on a hydrogenated silicon substrate. Using polarized NEXAFS measurements and DFT calculations, insights about the molecular and the electronic structure of $LuPc_2$ in films of different thicknesses on passivated vicinal Si(100)2×1 was determined. Both, the molecular architecture in the films and the influence on the electronic states could be investigated. The calculations of the N1s NEXAFS spectra were performed within the TPA, see chapter 4.4. The calculations were performed on a single molecule, which is a justified simplification since the passivated substrate is only weakly interacting with the molecule.

The experiments were conducted on thin and thick layers of $LuPc_2$ and obvious differences in the film architecture were revealed. In particular, in thin films, the molecules lie flat on the substrate while in thick layers they appear to be disordered. These insights into the orientation of the molecules on the surface were obtained from the polarized NEXAFS measurements conducted with two different orientations of the **E**-vector relative to the sample. Also in the submonolayer, the molecules are aligned parallel to the surface. Several film thicknesses of 0.3, 1.5 and 2.4 nm also displayed molecules with parallel orientation. The good agreement between the theoretical and the experimental spectra of the submonolayer, shown in Figure 5.4, confirmed the weak interaction with the passivated vicinal Si(100)2×1 surfaces. In the case of a submonolayer, the parallel alignment of the molecules with the substrate is supported by the DFT calculation, shown in Figure 5.4 (i). in the experiments performed on films of various thicknesses, a transition of the orientation of the $LuPc_2$ molecules was observed. However, when the film thickness reached a bulk-like magnitude, the orientation of the molecules began to head towards an approximated tilt angle of 45°, shown in Figure 5.4 (ii). The thick layer is considered to be less than 10 nm thick.

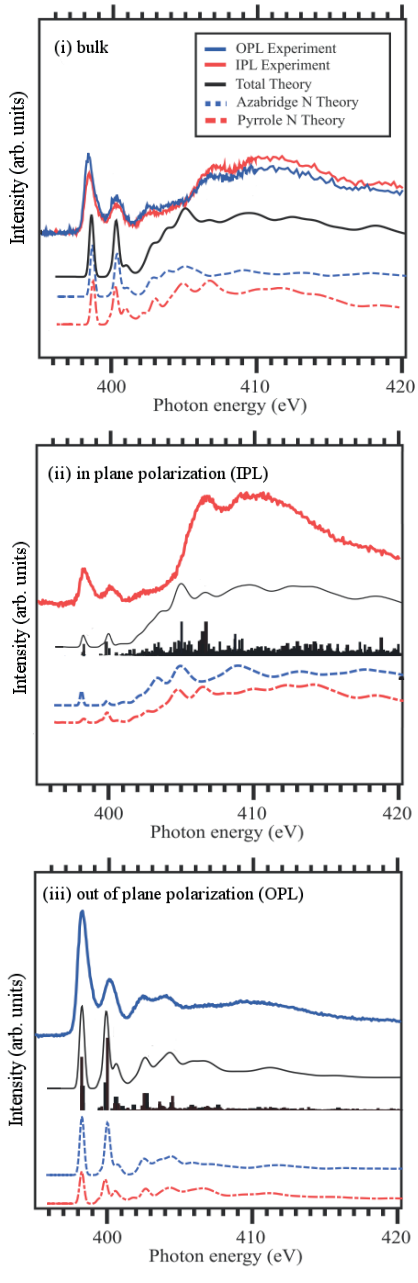

Figure 5.4. Comparison of the experimental polarized measurements (solid blue and red curves) and the theoretical (black curves) N1s NEXAFS for $LuPc_2$ adsorbed on hydrogenated vicinal Si(100)2×1 surface. The thick film (i) and the submonolayer for in in-plane (ii) and out-of-plane (iii) polarized light, e.g. with $I_{\parallel}$ and $I_{\perp}$, respectively, are compared. The contributions from the different kinds of N atoms are provided as blue and red dashed curves.

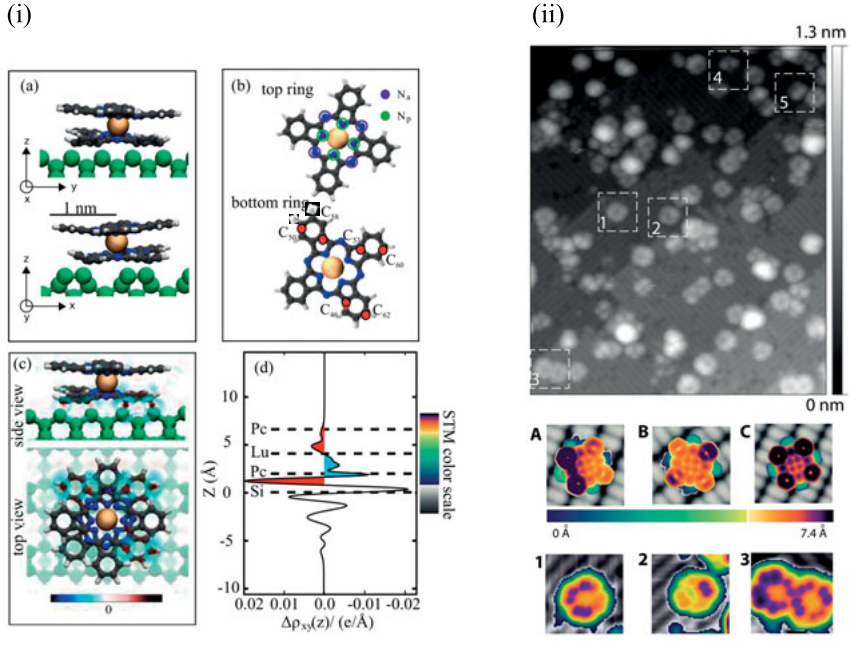

Figure 5.5. One of the adsorption structures of LuPc/Si(100)2×1 from different perspectives in (i-a and -b). Also shown is the adsorption induced charge redistribution (i-c) and the charge transfer curve between surface and molecule (i-d). Red areas represent charge accumulation and blue areas represent charge depletion. The positions of the Lu atom, the two Pc rings and the substrate are indicated in (i-d). The experimental (1-3) and theoretical (A-C) STM images are compared in (ii) where different calculated adsorption structures were chosen to resemble the experimental ones.

Further insights into the unoccupied electronic structure were gained from the detailed analysis of the contributions to the total NEXAFS spectra from individual N atoms, e.g. pyrrole N atoms (N_{pyr}) and azabridge N atoms (N_{aza}) see Figure 5.3. Those contributions are shown in Figure 5.4 in which data from of the N_{pyr} and the N_{aza} are the red and the blue curves, respectively. Apart from a projection of the out-of-plane transitions below the IP due to the bending of the phthalocyanine rings, the relative intensity ratio is inverted between the contributions of the two types of N atoms in the in-plane transitions. This is attributed to the transition into N_{pyr} in the first NEXAFS peak of $LuPc_2$. However, the total pre-edge features are very similar to those of other metal phthalocyanines [60, 229].

$LuPc_2$ on clean Si(100)2×1

A consecutive study was performed in Paper IV, in which the adsorption of $LuPc_2$ onto the reactive Si(100)2×1 surface was investigated. Of course, the

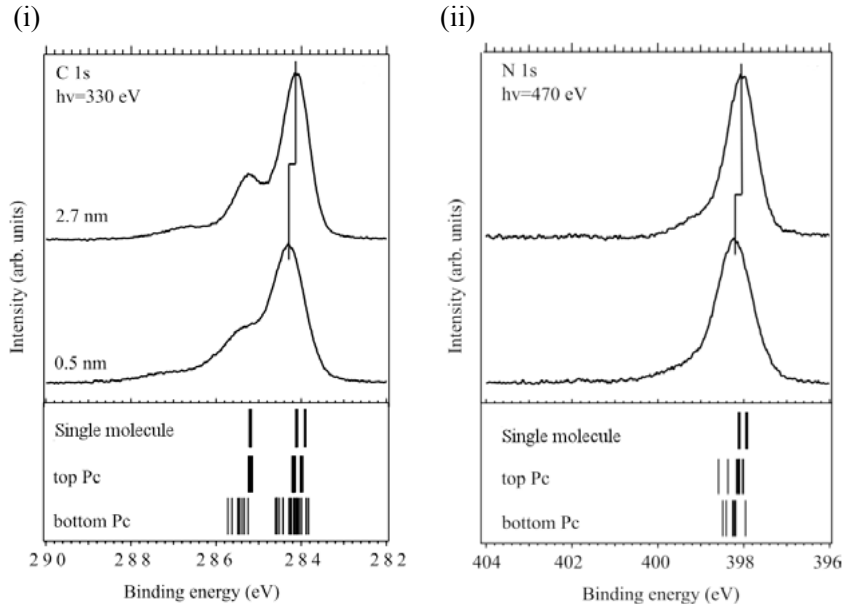

Figure 5.6. Measured XPS line profiles of C1s and N1s in (i) and (ii), respectively, compared to binding energy shift calculations for the single molecule and for the adsorbed molecule. For the latter case the contributions of the upper and lower Pc ring in a $LuPc_2$ are separated.

adsorption mechanisms are very different between the clean and the passivated Si(100)2×1 surface, due to the very different chemical reactivities of the latter surfaces. The remaining questions are, how the electronic properties of $LuPc_2$ are affected and if the molecular architectures show differences on a reactive substrate compared to a passivated Si(100)2×1.

Through the analysis of STM images, core level shifts and DFT calculations, several insights were obtained. The DFT optimized adsorption structures, one of them is presented in Figure 5.5 (i-a), show large deformations due to the strong binding to the surface. Especially the lower Pc rings, e.g. those directly bonded to the Si substrate, experience large distortions, while the upper ones are rather indirectly affected through the lower Pc rings. This becomes understandable through the bonds forming between the surface and the molecule. These are indicated on the 6 carbon atoms marked red in Figure 5.5 (i-b) which shows bonds forming between those C atoms and Si atoms in form of charge density accumulations, see Figure 5.5 (i-c). Furthermore, the charge transfer curve in Figure 5.5 (i-d) suggests a charge transfer of about 0.28e/molecule.

As seen in the measured and simulated STM images, more than one adsorption structure can be found. Moreover, the displayed computed STM images

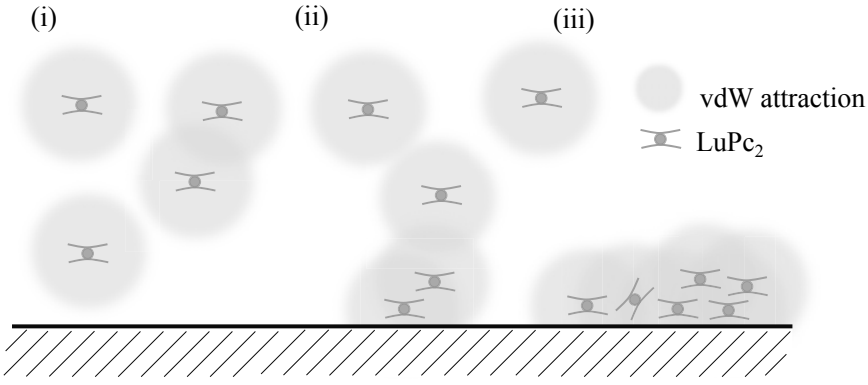

Figure 5.7. Illustration of the adsorption of LuBisPc on Si(100), (i) in which the molecules have a vdW attraction to each other, (ii) while if they are adsorbed, they direct other molecules to the surface and (iii) from clusters as a consequence.

resemble to a large extent the measured ones. This indirectly confirms the observation that the lower Pc rings deform more than the upper ones.

Both, geometric and electronic changes will influence the binding energy shifts. A comparison between experimental C1s and N1s line profiles and computed XPS binding energy shifts are shown in Figure 5.6. The calculations were performed according to Eq. (4.26). Three cases were considered, the single molecule, the upper Pc ring (top) and the lower Pc ring (bottom). Compared to the single molecule calculation, the binding energy shifts for the adsorbed molecule show large changes. The fact that the changes are larger for the lower Pc rings than for the top Pc rings demonstrates that the interaction with the substrate is the cause for this. Also the fact that the C atoms, which form bonds with the substrate, show larger changes than the N atoms, which do not form direct bonds to Si atoms, supports this conclusion. The experiment provides a similar picture. The measurement on the thin layer appears broader than the one on the thick film. This points to a stronger change of the binding energies on the thin film.

In Figure 5.5 (ii), the experimental STM image shows the clustering of $LuPc_2$ molecules in the submonolayer. To elucidate this interesting physical situation, closely linked to the self-assembly phenomena, we modeled the most relevant intermediate steps which can occur during the adsorption process of more than one $LuPc_2$ molecule on the pristine Si surface. One important aspect for the adsorption and molecule-molecule interaction is the long-ranged van-der Waals interaction. The experimental STM images suggest that the molecule-molecule interaction is strong, and at the same time the surface-molecule interaction is also strong. Even though they might compete, it is unlikely that the molecules exhibit a high mobility after adsorption, which points towards larger surface-molecule than molecule-molecule interaction after adsorption. The molecules can initially land on any adsorption site. Although,

the adsorption might be regarded as a random process, there was no experimental observation of a uniform molecule distribution on the surface. This suggests the possibility of a van der Waals guided clustering of the molecules on the surface. The adsorption process might include the following steps depicted in Figure 5.7 (i) to (iii). While still not adsorbed, but within the vicinity of already an adsorbed molecule, the long-ranged vdW interaction attracts the "free" molecule to an already adsorbed one. This is supported by a large vdW adsorption energy of 2.7 eV[1] between two staggered $LuPc_2$ which is of similar order as other adsorption energies of phthalocyanines [59]. From here, it might be argued that processes linked to temperature/vibrations and collisions with other "free" molecules cause the upper molecule to be pushed to the site where it then can interact with the surface resulting in a larger adsorption energy (up to 4.63 eV) thus gaining energy. Therefore, the complex interplay between the double decker structure of the $LuPc_2$ molecule and different kinds of attractions (vdW and formation of covalent bonds) with different length scales and energy regimes per atom might, in the case of $LuPc_2$ on pristine Si, cause complex adsorption processes.

5.3 The biphenylene project

"If you fail to plan,
you are planning to fail! "

– Benjamin Franklin

The bottom-up growing process with biphenylene

The results of the Papers VIII, IX, X and XI are discussed. The biphenylene project itself has the aim to investigate possible paths to obtain a novel molecule-based 2-dimensional (2D) material through a bottom-up growing process. The investigation and searching for novel 2D materials might lead to a variety of technological applications which is inspired by the fascinating physics of graphene, a carbon allotrope, and a variety of other 2D materials like monolayers of MoS_2, and hexagonal boron nitride [131, 151, 153, 157, 158, 161, 230, 231] in this section.

One of the most important differences between low dimensional materials and their bulk equivalents is caused by quantum confinement effects [149, 232, 233]. These effects appear if the extensions of the system in a particular dimension is lower than a critical value which is often in the range of a few

[1] It might be noted, that even though the vdW energy of 2.7 eV and the adsorption energy of 4.63 are very similar, the both energy should take the atoms participating in the adsorption. In our context, however, total energy should be compared.

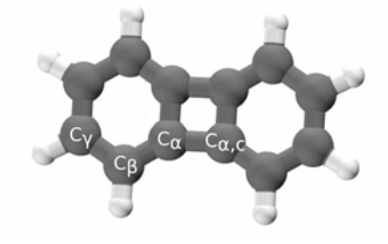

Figure 5.8. Illustration of the biphenylene molecule. The figure was taken from Ref. [234].

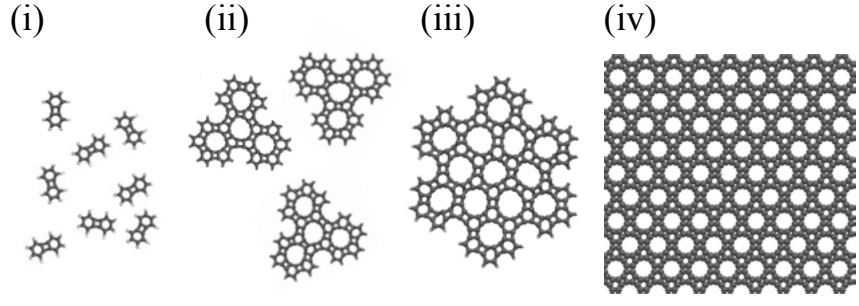

Figure 5.9. Illustration of a possible bottom-up growing path of biphenylene carbon. Starting with $C_{12}H_8$ in (i), nanoflakes of growing size form (ii) and (iii) which eventually build a monolayer (iv) only consisting of C atoms but remain a biphenylene-like basis in a (4,6,12) ring structure.

nm or less. The quantum confinement effects may lead to tunable properties, e.g. varying with size, which are *not* possible to describe by classical theories.

The biphenylene molecule ($C_{12}H_8$), shown in Figure 5.8, is a promising candidate to build a new 2D carbon network, the biphenylene carbon (BPC), in a bottom-up growing process. Several biphenylene molecules are shown in Figure 5.9 (i). Starting with several molecules, biphenylene nanoflakes, shown in Figure 5.9 (ii), can be formed after dissociation of H atom and if ordered structures start to assemble. If this process is continued, larger nanoflakes form and eventually a complete sheet is obtained, shown in Figure 5.9 (iv).

To understand and be in control of these processes it is important to know the initial electronic structure of the biphenylene molecule which we have investigated by means of a joint experimental theoretical work in Paper IX and X. Also its interaction with substrates, which can have catalytic effects during the formation process, is important to study (Paper XI). Even though all these investigations may lead to a processing path, the properties of BPC are unknown. However, by theoretical means the properties of BPC can be predicted. Paper VIII investigates the electronic, optical and excitonic properties of the BPC.

Planar organic molecules with rings structures can be distinguished as either aromatic molecules like benzene or as anti-aromatic molecules. The aromatic and anti-aromatic molecules have very different properties. While the aromatic ones like benzene and phthalocyanines have large delocalized frontier orbitals and are chemically and thermally very stable, the anti-aromatic molecules like cyclobutadiene and biphenylene have more localized frontier orbitals and are not necessarily very stable, both chemically and thermally [235]. In particular, the cyclobutadiene molecule, planar square rings of four carbon atoms, is very unstable and decays within seconds due to the large angular and torsional strain in its bonds. The latter facts cause major challenges in studying anti-aromatic molecules.

The gas phase biphenylene molecule

In Paper IX, the electronic structure of the biphenyelne gas-phase molecule was investigated by a joint experimental and theoretical study. The valence states were probed by photo-electron spectroscopy and the hybrid functional DFT calculations complemented the experimental insights. The 1s core levels were calculated according the ΔSCF calculations using Eq. (4.25) and (4.26). The 1s to p^* transitions probing the unoccupied p-orbitals were based on the transition-potential approach according to Eq. (4.15). The experimental corresponding techniques were PES, XPS and NEXAFS spectroscopy, respectively. This combination of techniques provided comprehensive insights into the occupied and unoccupied electronic structure of the biphenylene molecule.

Our investigation of the biphenylene molecule in Paper IX has identified the atomic contributions to the electronic states, seen in Figure 5.14. Due to the anti-aromatic character, the valence orbitals are not completely delocalized over the whole molecule, but they are more localized at the C_α and C_γ atoms of the two benzyne rings. The molecular orbitals of the biphenylene are characterized by some nodal planes crossing the square rings, which contribute to the localization of electrons on the benzyen-rings. This particular characteristics of the orbitals is at the origin of the anti-aromatic character of the biphenylene molecule. In other words, since less electrons are on the square-rings, the orbital strain is reduced within the biphenylene molecule.

Further evidence of the accumulation of charge at certain parts of the molecule is given by the XPS calculations, which are compared to the experimental XPS peaks, shown in Figure 5.14 (ii). The theoretical broadening was done for two cases, a symmetric Gaussian broadening and an asymmetric one with a skew Gaussian to effectively account for vibrations. Due to the broadening and the very closely lying C1s binding energies, only one peak can be seen in the experiment. The calculations showed that the three C1s binding energies are very close in energy. At the same time, theory showed that charge is not

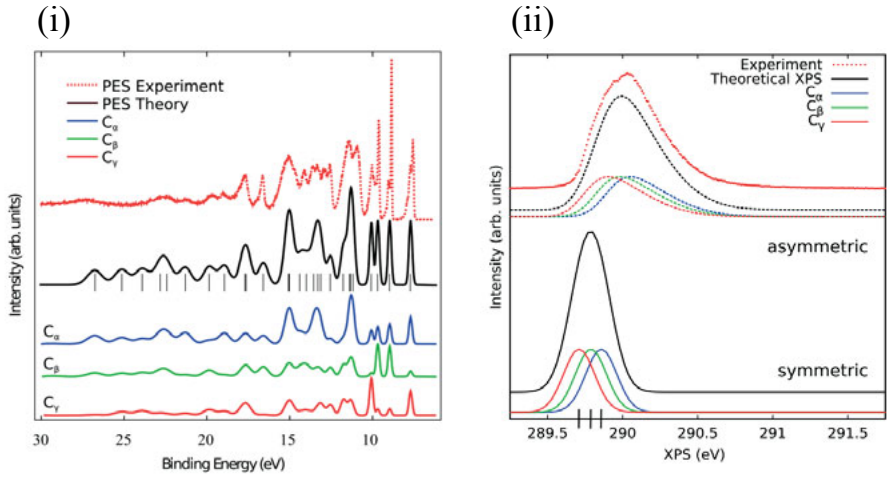

Figure 5.10. PES (i) and XPS (ii) results for the biphenylene molecule; comparison between experiments and theory. The figures were taken from Ref. [234].

equally distributed among the C atoms but accumulated at the C_β while the C_γ have less charge.

Ordered and disorder biphenylene films on Cu(111)

The adsorption of biphenylene molecules on the Cu(111) surface at low temperature (90 K) was studied in Paper XI. The purpose was to investigate the molecular architecture of biphenylene molecular films by combining NEXAFS, XPS, PES and DFT results.

The NEXAFS results of Paper IX can be compared to the NEXAFS data of Paper XI. Figure 5.11 compares the NEXAFS spectra of the gas phase molecule in (i) to the molecule in films adsorbed on Cu(111) in (ii). In the gas phase, the transitions into π^* and σ^* orbitals are averaged over all orientations. This is represented by the random orientation of the molecules. With this in mind, experiment and theory have excellent agreement in Figure 5.11 (i).

The molecular architecture of the biphenylene molecular films on Cu(111) is dependent on the film thickness. At low coverages, the molecules align relatively flat on the substrate. This can be seen in the huge polarization dependence between π^* and σ^* transitions in Figure 5.11 (ii-1). However, at high and intermediate coverages, the molecules form disordered films. If an intermediate film is annealed, the probed molecules on the film show order again, see Figure 5.11 (ii-3).

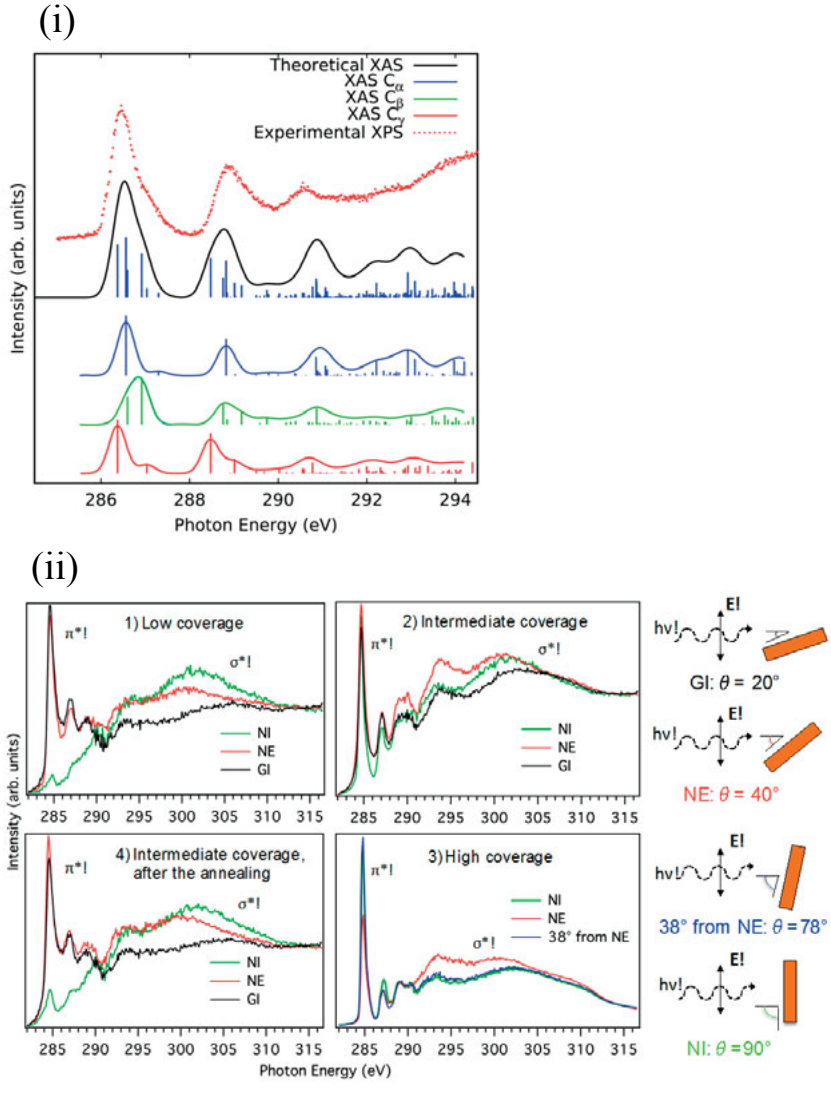

Figure 5.11. NEXAFS of the gas-phase biphenylene molecule (i) and the adsorbed biphenylene molecule on Cu(111) for different film thicknesses (ii). The figure was taken from Ref. [234].

Theoretical study of many-body effects in the biphenylene molecule

A theoretical investigation regarding a quantitative description of the electronic state of biphenylene was conducted in Paper X. An accurate description can be important to properly describe electronic processes within a material. In Figure 5.12 (i), the accuracy of different theoretical methods is compared. The investigation comparing results of the ionization energy (IE) and the electron affinity (EA) obtained with hybrid functionals, GW, ΔSCF calculations and the OT-RSH approach, showed that several methods can reach similar accuracy. In particular, OT-RSH and GW give similar EA's and IP's. Also the ΔSCF method yields those accurately. The latter fact is even relatively independent of the underlying functional.

These findings can also used to determine the electronic attributes of intermediate steps in the formation of BPC. Moreover, biphenylene may not be the ideal candidate to build BPC, and a halogenated substitute may perform better. Then the accurate theoretical description can be used in conjunction with experiments to investigate the bottom-up growing process and additionally to estimate the efficiency.

The excitonic and many-body effects in the 2D biphenylene carbon

2D carbon networks have captured a considerable amount of attention in science and industry research and applications. Graphene [236, 237], graphane [238] and graphyne [239] are only three examples out of many. They promise low production costs compared to materials based on expensive elements due to the abundance of carbon. The development of the bottom-up process to build a complete sheet based on biphenylene is not yet completed. Many challenges and obstacles, like the chemical processing, need to be understood and solved. Also their solutions will eventually be optimized. The adsorption on substrates, which may act as a catalyzer in the chemical reactions, is one aspect. How the biphenylene molecule arranges on the substrates when adsorbed on the surface, also with regards to self-organization, is another one. The stability of the final system and its intermediate structures during the growth process also deserve consideration. Facing all of these and other challenges, the development is coupled to great efforts, time and resources. With the theoretical methods available, a close look at possible outcomes can be taken, e.g. the electronic properties of the hypothetical biphenylene sheet can be investigated. This has the advantage of estimating what is waiting at the end of a perhaps long development. At same time, it motivates to continue the experimental efforts.

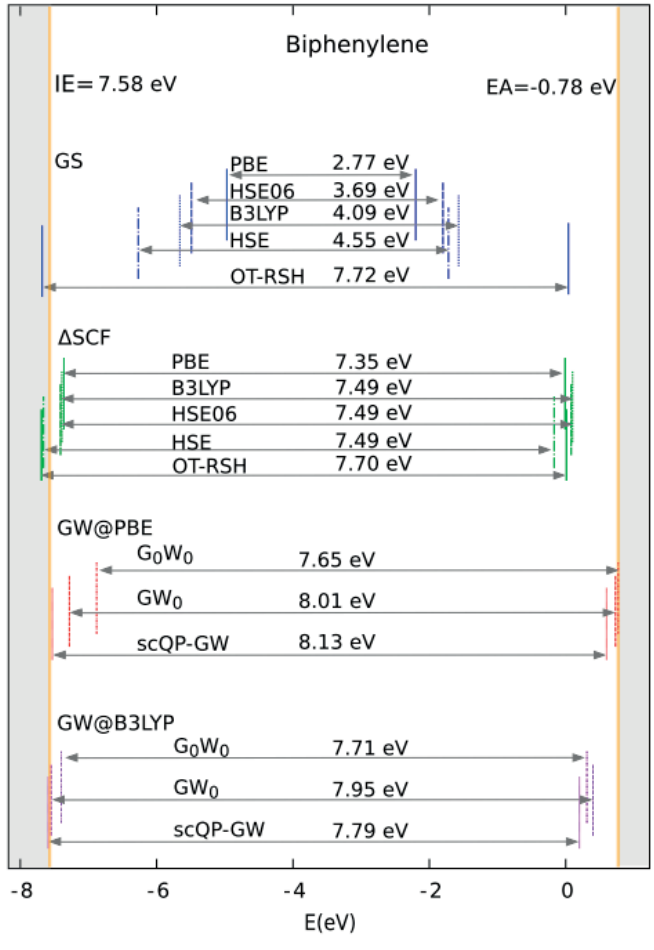

Figure 5.12. Comparison between different theoretical approaches to determine the ionization energy (IE) and the electron affinity (EA) of biphenylene.

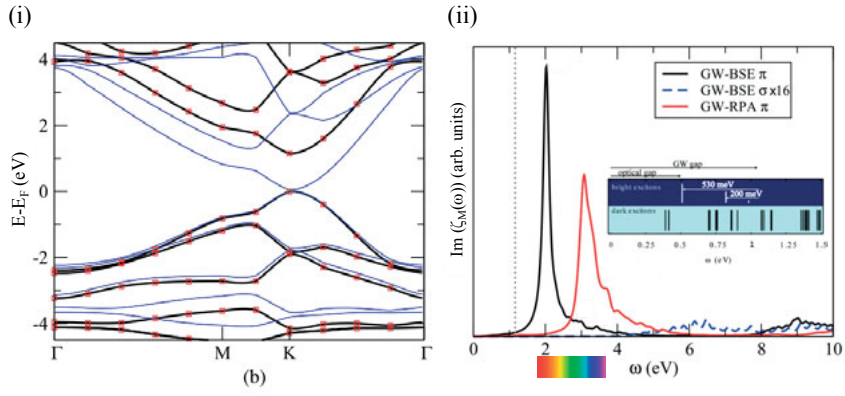

Figure 5.13. The GW corrected band structure (black bands) of BPC compared to the DFT band structure (blue bands) in (i) and the absorption spectrum of biphenylene carbon in (ii). The adsorption spectrum compares the GW-BSE (black profile) and the GW-RPA (red profile) spectrum for the interaction with light polarized perpendicular to the BPC plane. Also the visible energy range is indicated in (ii). The adsorption (GW-BSE) with light polarized parallel to the BPC is shown as blue dashed curve. The absorption of visible light is indicated. The insert shows the bright and dark exciton contributions. The figures were adapted from Ref. [155].

The BPC, or biphenylene sheet, is a periodic 2D carbon network with a 4, 6 and 12-ring structure. The material was first described by Balaban [240]. With the predictive study about the electronic and optical properties of the biphenylene sheet in Paper VIII, the questions were addressed concerning what properties the hypothetical biphenylene sheet may have, where it could find applications and if development efforts would eventually pay off. In detail, the one-particle self-energy was evaluated with the GW approach to obtain accurate band structure results. The results of the latter, e.g. the quasi-particle corrected states according to Eq. (4.5), were used in the Bethe-Salpeter ansatz, a two-particle approach, to calculate the optical absorption spectrum and excitonic levels, Eq. (4.11) and (4.12), respectively.

Figure 5.13 shows the GW corrected quasiparticle band structure in (i) and the adsorption spectrum in (ii). The direct band gap, e.g. the fundamental gap, is about 1.0 eV in the GW calculation. Small changes in the dispersion can also be seen. The optical gap of BPC obtained from GW-BSE calculations is 0.5 eV, thus the bound exciton has a binding energy of 0.5 eV. This large exciton binding energy is a result of the decreased screening in the 2D materials, illustrated in Figure 4.5 (ii). Also a variety of dark excitonic states form within the fundamental gap; most of them have larger binding energies than the bright exciton. This could lead to applications of BPC in quantum information technology.

The adsorption spectrum of BPC has parts in the visible light range. Since the material also has a direct gap, BPC may find application in solar en-

ergy harvesting. Typically for 2D materials, BPC has a strong adsorption anisotropy, e.g. it adsorbs more light with perpendicular polarization (π^*) than with parallel polarization (σ^*). For light harvesting, the excitonic effect might be useful and could be made more efficient in heterogeneous structures.

5.4 About the spin-state manipulation of iron-phthalocyanine through adsorption

Paper V, VI, and VII investigate the FePc molecule, and in particular its electronic properties. While the gas phase of the FePc (Paper V) can be regarded to be an unperturbed system, its electronic and magnetic states can be modified when adsorbed on substrates or when interacting with a so called modifier molecule. The interest in the FePc molecule is generated by its possible applications in many fields of technology. Organic field effect transistors, photoelectric devices, and molecular switches are only a few examples [241, 242]. In these devices, the characteristic electronic, optical and catalytic properties of FePc could be employed.

The gas phase FePc molecule

In Paper V, the electronic states of the gas phase FePc molecule were studied. This is of particular importance as a reference for situations in which the molecule is adsorbed on a substrate or when it interacts with other molecules.

The XPS experiments where conducted and they were complemented by Fe $2p$ multiplet XPS calculations. The gas phase results were compared to measurements performed on FePc films with a thickness of about 10nm. A comparison between gas-phase, film measurements and calculations is shown in Figure 5.14. The calculations suggest a triplet ground state, which give a good agreement with the $2p$ XPS measurements, both for the gas-phase molecule and the film. For the film a specific ground state, ^3E_g, could be suggested while the increased broadening in the gas phase measurements did not allow for a clear distinction.

The adsorption of FePc on Cu(111)

The FePc adsorbed on a Cu(111) surface forming a 0.5 monolayer (ML) was investigated in Paper VI. Through adsorption on substrates, subtle changes in geometric and electronic properties can be induced. In particular in Paper VI, we have investigated the main reason for this symmetry breaking whether it is of electronic or geometric nature for the FePc/Cu(111).

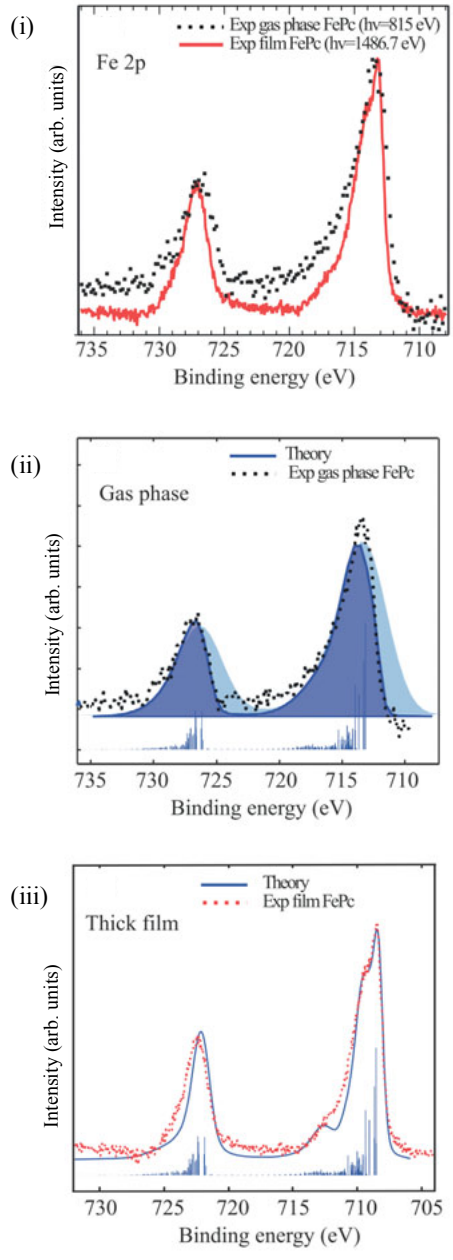

Figure 5.14. Comparison between gas phase and thick film Fe 2*p* XPS measurement (i), between theory and experiment for the gas phase and the film in (ii) and (iii), respectively. The figures were taken from Ref. [243].

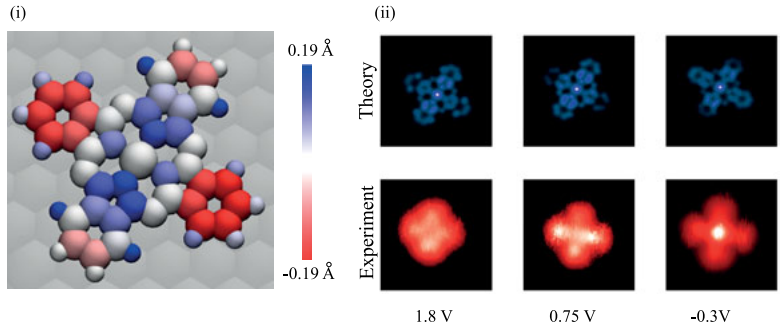

Figure 5.15. (i) FePc adsorbed on Cu(111) shown in a relative height profile. (ii) Experimental and simulated STM images at different bias voltages. The figures were taken from Ref. [92].

The experimental STM and XPS measurements were supported by DFT calculations. The calculations of STM images were performed in the Tersoff-Hamann approach [81]. The XPS simulations of the C1s binding energies were performed employing Eq. (4.25) and their relative shifts according to Eq. (4.26).

Figure 5.16 (i), shows the adsorption geometry of FePc on Cu(111) as a relative height profile of the molecule. As can be easily seen, the symmetry of the molecule is reduced from D_{4h} to C_2 due to deformations out of the molecular plane. Two of the isoindole rings are more bend to the surface than the others. Especially, the carbon atoms are attracted to the surface while the N atoms have a larger distance. Also the simulated STM images are shown in Figure 5.16 (ii). Therein, the height differences are also visible, but the results are convoluted with the electronic contributions. This applies also for the experimental STM images, since effectively the charge density is probed. As may be seen, the comparison with the experimental STM images is good.

Figure 5.16 shows the analysis of the effective Bader charges. The charge transfer analysis reveals that the symmetry is reduced and that a different amount of electrons can be found on the isoindole rings. The influences of the nonisotropic charge transfer is also seen in the core-level line shapes, shown in Fig. 5.16 (ii). Two C1s XPS line profiles are compared in this figure. One is from a multilayer of FePc on highly oriented pyrolytic graphite (HOPC), the other one is from the 0.5 ML FePc/Cu(111). The comparison shows that the interaction of the FePc on Cu(111) is more involved than the one for the multilayer of FePc on HOPC. This is reflected in the increased broadening of the peaks for the FePc/Cu(111) case compared to FePc/HOPC. The calculations of the XPS line shapes, support this finding. Due to the electronic and geometric influences the binding energies are altered for FePc/Cu(111). In detail, the C atoms of the two different symmetry axises across the molecule show distinct differences in their 1*s* binding energies, shown in Fig. 5.16 (iii) by the shifts between the red and the blue curves. The larger contributions arise

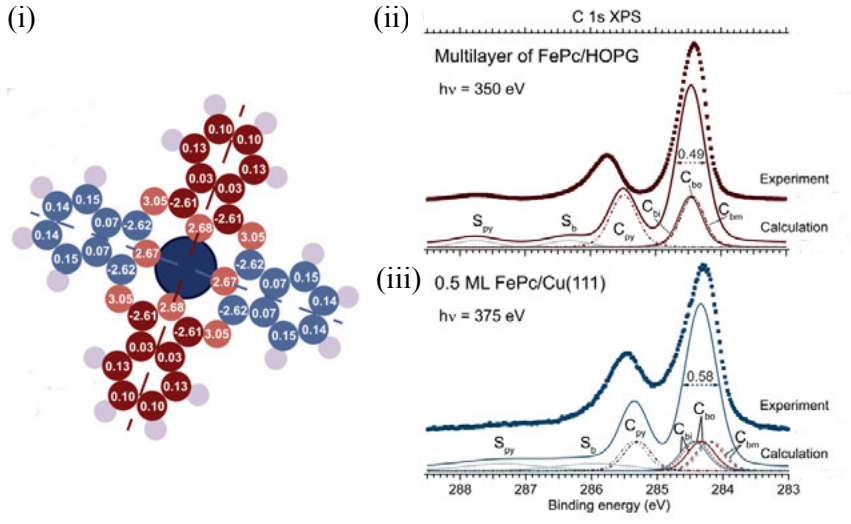

Figure 5.16. (i) Effective Bader charges and symmetry axises (blue and red) are indicated. (ii) Computed and measured C1s binding energies for FePc/HOPC and compared to FePc/Cu(111) (iii). Also in (iii), the calculated contributions according to the symmetry axises are indicated as blue and red curves. The figures were taken from Ref. [92].

from the final state effects, especially from the interaction with the substrate. Also the deformation of the molecule by itself causes a reorganization of the electronic density which also affects the binding energies.

Therefore, one may conclude that the symmetry reduction of the FePc adsorbed on Cu(111) is of mixed nature, e.g. there are electronic and geometric factors which influence each other. The final result is a C_2 symmetry of the FePc molecule. This was suggested by experimental data and confirmed by DFT results.

The adsorption of FePc and Py/FePc on Cu(100)$c(2\times2)$-2N/Cu(111)

Furthermore, the possible modifications of the electronic structure of FePc by changing the substrate and by applying a modifier in form of a pyridine (Py) molecule were investigated in Paper VII. In detail, the adsorption of FePc forming a monolayer onto the copper nitride, e.g. Cu(100)$c(2\times2)$-2N/Cu(111), surface was investigated and the results were compared to the adsorption of this system onto Cu(111) and onto Au(111).

The FePc has an adsorption site dependent spin state if it is adsorbed directly on Cu(100)$c(2\times2)$-2N/Cu(111). In detail, the FePc has a larger multiplicity when the Fe ion is above a Cu atom than adsorbed on a N atom.

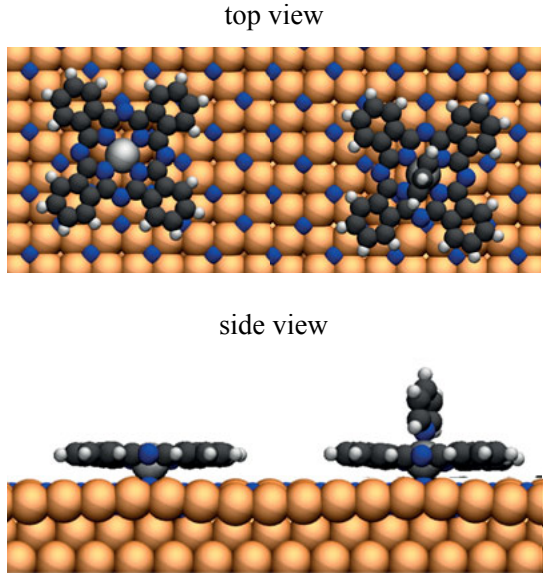

Figure 5.17. A selected adsorption structure of FePc (left) and Py/FePc (right) on Cu(100)$c(2\times2)$-2N/Cu(111) in comparison.

Figure 5.17 shows the FePc on Cu(100)$c(2\times2)$-2N/Cu(111) adsorbed directly on a N atom. The Fe atoms is pulled towards the surface and the qualitative Bader charge analysis suggested alteration of the electronic configuration of the metal ion driven by a charge transfer to the N atom. Moreover, the interaction between the Fe and N atoms appears stronger than for Fe and Cu. This is seen in a smaller adsorption distance for the former case. As a consequence the magnetic moment on the iron atom is reduced.

The adsorption energy difference is about 1 eV between the adsorption site with the largest and smallest adsorption energy. However, the monolayer formation energy[2] is about 1.8 eV and is therefore larger than this energy difference. Even though potential barriers between the adsorption sites, which are larger than the latter energy, might exist, it is an indication that more than one adsorption site might get occupied in a monolayer.

The adsorption of pyridine on FePc that in turn is adsorbed onto the copper nitride quenches the magnetic moment on the iron ion. An adsorption structure of Py/FePc/Cu(100)$c(2\times2)$-2N/Cu(111) is shown in Fig. 5.17. This can be understood from the lone-pair electron of Py which hybridizes with the metal center of FePc. These changes have also influence on the XPS line shapes of the C1s, N1s and the Fe2p levels. This is shown in Figure 5.18 (i). In general the modifier tends to adsorb on the central metal ion, quenching the magnetic moment for all adsorption sites. The charge transfer from the iron ion to the

[2]The monolayer formation energy is here defined as the exothermic energy which is released when free molecules form a periodic free-standing monolayer.

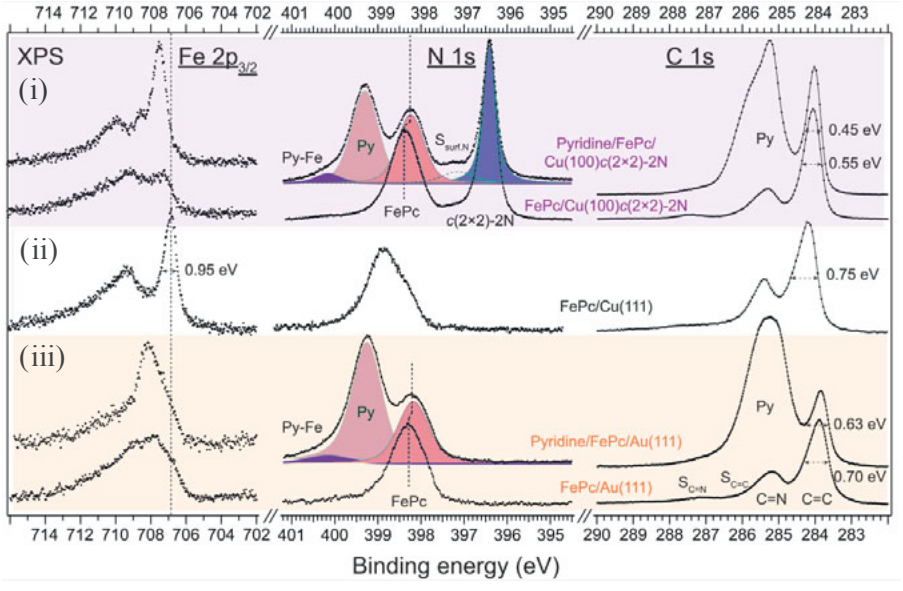

Figure 5.18. XPS C1s, N1s and Fe $2p_{3/2}$ line profiles of FePc and Py/FePc on Cu(100)c(2×2)-2N/Cu(111) in comparison with the equivalent ones on Au(111) and Cu(111) in (i), (ii) and (iii), respectively. The figure was taken from Ref. [92].

surface and to pyridine is larger than in the case without pyridine. Also the changes in the electronic states contribute to the quenching of the magnetic moment. These changes are also apparent in the Fe $2p$ XPS line profiles.

However, also the spectral shapes of the N and C atoms change if pyridine is adsorbed onto FePc/Cu(100)c(2×2)-2N/Cu(111). Apart from the stoichiometric changes induced essentially from the presence of pyridine in the measurement, the FePc shows different interaction strength with different substrates. Again, the line width provides important insights into the hybridization strength between molecule and surface. While for the adsorption onto Cu(111) the line widths are largest, they are smaller for the Au(111) case and smallest for the adsorption onto Cu(100)c(2×2)-2N/Cu(111). The latter fact can be explained from the electronic decoupling of the FePc from the Cu(111) since Cu(100)c(2×2)-2N/Cu(111) is insulating. These changes in the full width at half maximum (FWHM) indicate charge density redistributions upon pyridine adsorption. These results showed that the pyridine, e.g. a modifier, can have significant influence on the electronic and magnetic properties of FePc.

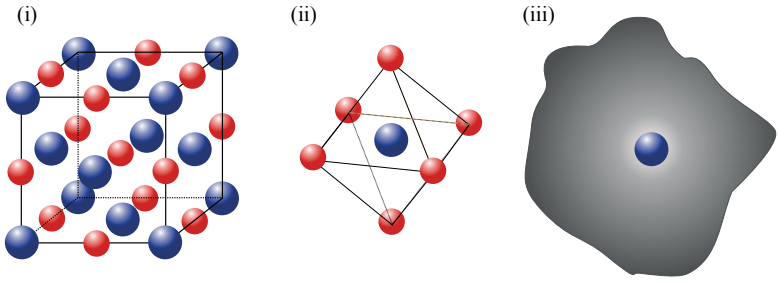

Figure 5.19. Lattice of a TMO XO (X=Ni,Co,Fe,Mn) in (i), the TMO in the cluster model in (ii) and the TM in the bath model in (iii). Blue atoms are TM atoms, red atoms are oxygen atoms and the gray area represents the bath.

5.5 X-ray absorption of transition-metal oxides

For the approach proposed in Paper XII, e.g. the study of the *L*-edge absorption spectra employing the hybridization function Eq. (4.22) in the multiplet approach from Chapter 4.5, we chose to test the method on well studied systems with plenty of experimental and some theoretical references, i.e. the well known fcc Transition Metal (TM) oxides; NiO, FeO, CoO and MnO [175, 180, 195, 244–246, 246–249]. Their crystal structure is shown in Fig. 5.19, which also illustrates the cluster approach in which the solid is reduced to the TM atom with the surrounding O atoms. The figure also shows the TMO-bath that is used in our approach. TMOs are of huge technological interest and they find (possible) applications in many fields, for example, in energy storage and conversion [250–253], or in devices for memories [254, 255].

All these 3*d* TMOs contain strongly correlated *d*-electrons and their respective multiplet effects in XAS measurements are large. Several cluster calculations including multiplet crystal field, charge transfer and ligand field theory calculations were conducted to analyze the experimental spectra [176, 195, 256].

The XAS spectra of NiO, FeO, CoO and MnO have been computed according to Eq. (4.24). Details of the calculations are given in Paper XII. The DFT results, summarized in Tab. 5.1, yielded the crystal-field parameter 10Dq, the ligand splitting through fitting of the hybridization function (Eq. 4.22) while the on-site energies U_{dd} and U_{pd} as well as the charge transfer energy Δ were taken to fit the experiments.

The difference between the crystal-field calculation, e.g. without hopping from the ligands, and the calculation including the coupling to the bath states (Eq. 4.22) are shown in Fig. 5.20 and 5.21. The results without hopping from the ligands are the black curves and those including hopping from the ligands are the filled curves. For the purpose of better comparison, the spectra are aligned at the largest peak. The plots show the results for different choices of the crystal-field strength beginning from 0.1 eV and increasing in 5 steps to 1.5eV. With increasing crystal-field strength, the spectra become in general

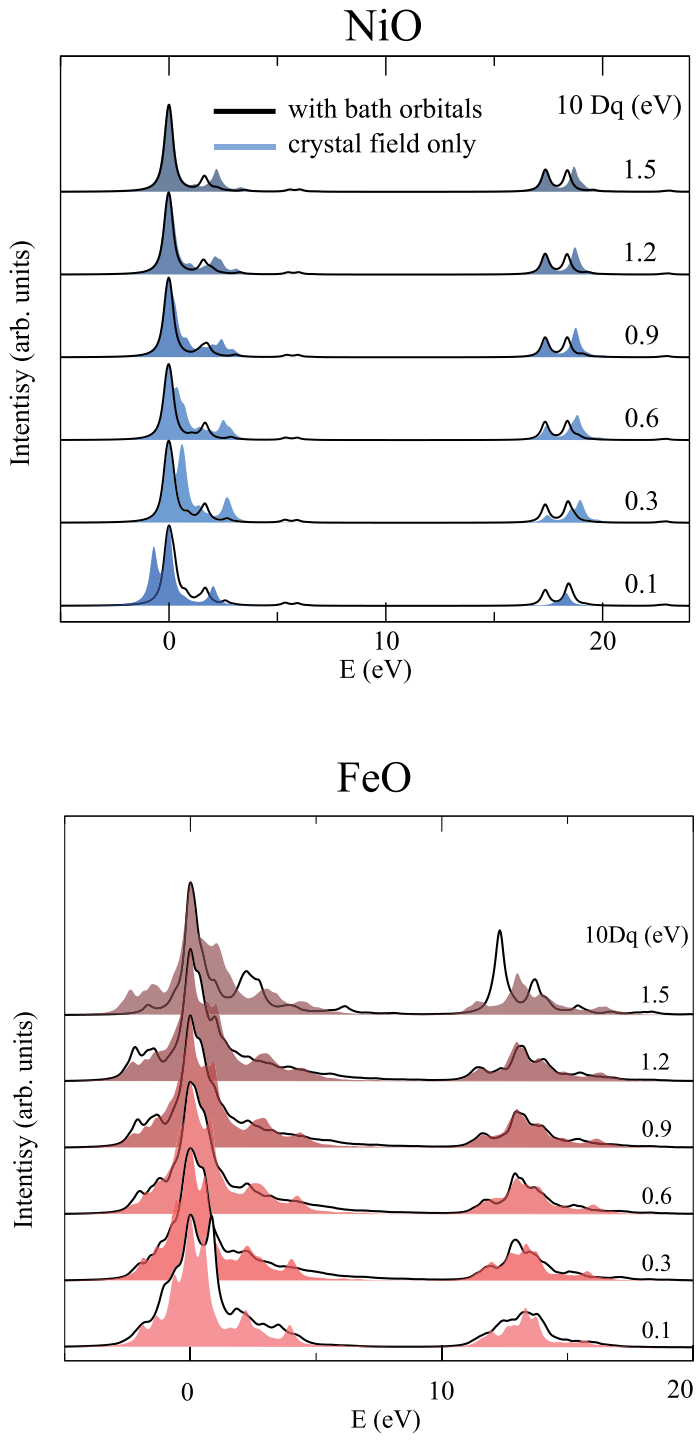

Figure 5.20. Comparison between the computed XAS with (black solids curves) and without charge transfer effects (filled curves) of NiO (blue) and FeO (red).

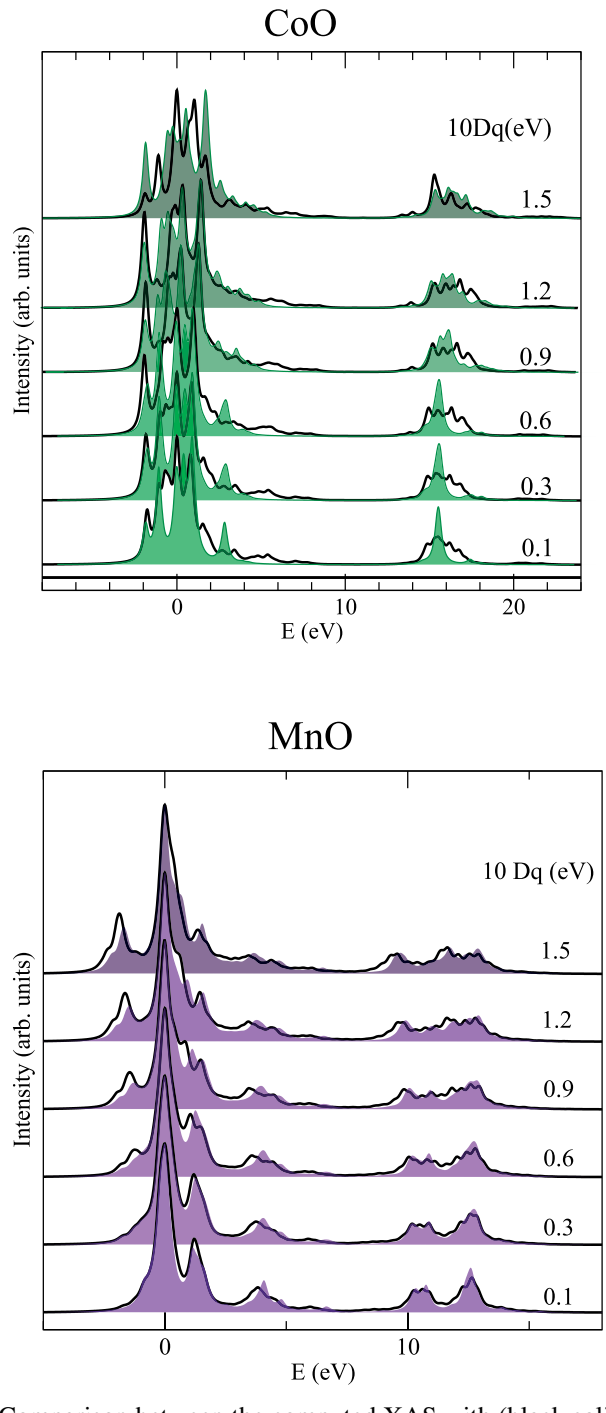

Figure 5.21. Comparison between the computed XAS with (black solids curves) and without charge transfer effects (filled curves) of CoO (green) and MnO (purple).

Table 5.1. *Summary of the used parameters and the results in the MLFT calculations.*

	NiO	CoO	FeO	MnO
F^0(eV)	7.5	7.0	6.5	6.0
F^2(eV)	10.1	10.0	9.2	9.0
F^4(eV)	6.7	6.7	6.2	6.1
Δ(eV)	4.7	4.0	4.0	8.0
U_{pd}(eV)	10.5	8.4	9.6	7.2
10Dq(eV)	0.65	0.79	0.85	0.86
V_{e_g}(eV)	2.07	2.62	2.12	1.80
$V_{t_{2g}}$(eV)	1.08	1.44	1.18	0.90
n_d	8.17	7.18	6.18	5.08

broader. This shows a connection between the sub-edge width and 10Dq. However, 10Dq cannot be taken directly from experimental result [178].

In general, the charge transfer effects are most obvious to result in a contraction of the spectral shape as well as resulting in small satellite contributions [93]. In NiO, the contractions is very strong for small values of 10Dq. In MnO, CoO and FeO, the effect is less obvious. Also new ground states can be the result of the charge transfer [257].

In Figure 5.22, the computed spectra are compared to experimental measurements [246–249]. Excellent, but still improvable, agreement with experiments were obtained for most TMOs. Clearly, the branching ratio can be reproduced to a good extent even though a constant broadening was applied in the calculations. Experimental reality includes additional complex mechanisms like the Coster-Kronik decay and the Super Coster-Kronik decay and interactions with phonons which generally cause non-uniform broadenings. Especially, the L_2 sub-edge is often broader than the L_3 one [195]. On the other hand, background is contributing to the L_2 intensities in the XAS of FeO, CoO and MnO. However, the presented calculated and experimental spectra agree in the strong deviations from the statistical branching ratio (4:2).

The largest differences between measurements and calculations are found for the CoO and FeO cases. For the former one, charging effects while for the latter one crystal defects and off-stoichiometry are possible causes for the seen differences. For NiO and MnO, most for the details can be reproduced. In the case of NiO, the sub-edge L_2 shows remarkable agreement. Both peaks have the correct separation in relative peak intensity. Also L_3 has these attributes. Even the small shoulder at 856.5 eV can be seen. For MnO, L_3 shows all prominent features in the calculations including the pre-peak at 638.5 eV, the main feature at 640 eV and its shoulder as well as a minor peak at 641 eV and small contributions at 643 eV and higher. L_2 instead is a broad peak due to the

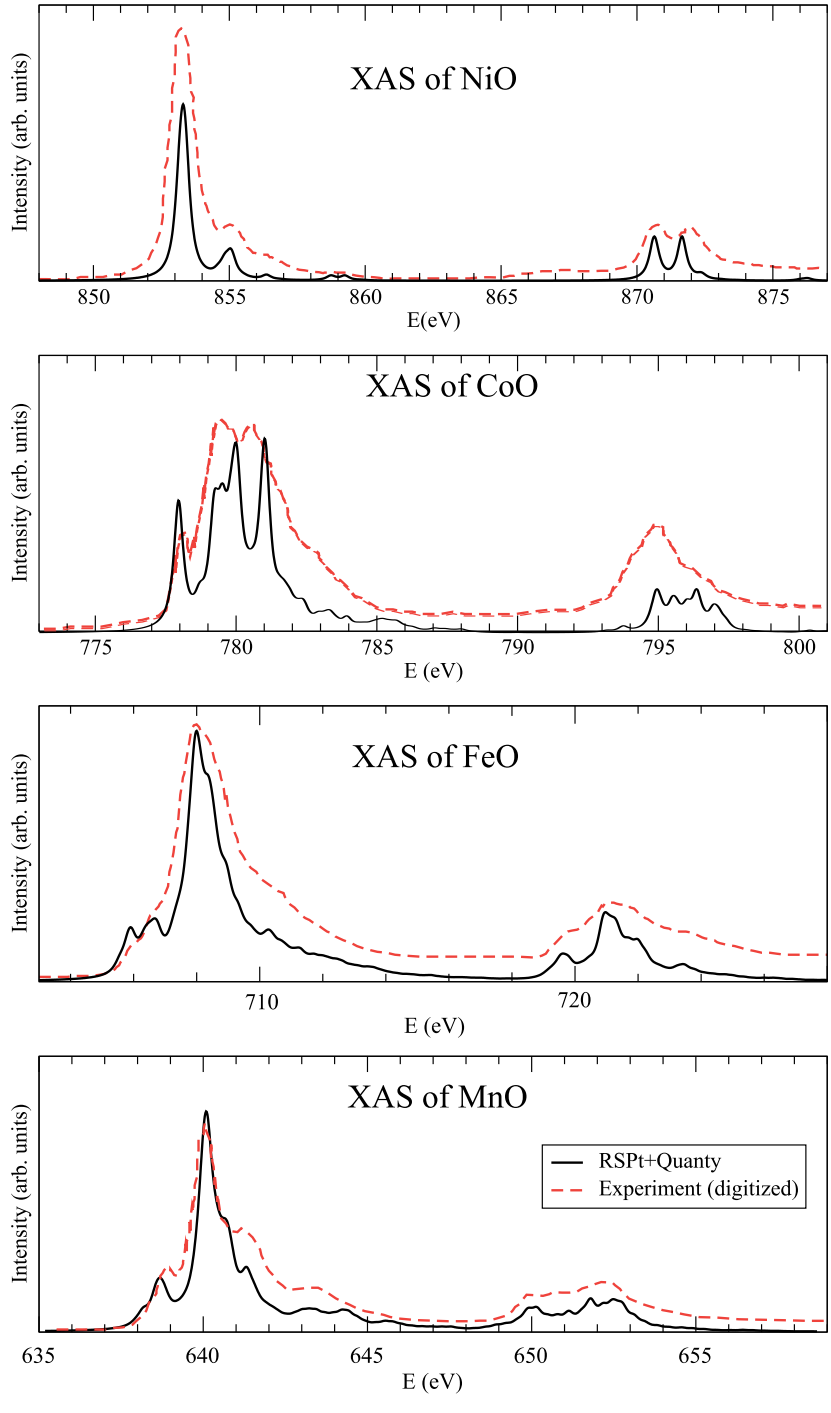

Figure 5.22. Comparison between experimental [246–249] (red dashed curves) and theoretical XAS (black curves) spectra of NiO, CoO, FeO and MnO.

vicinity of many small contributions. Most importantly, the ansatz employing the hybridization function and the local Green's function appears to work for the calculation of $2p$ XAS of TMO.

6. Concluding remarks and outlook

The phthalocyanines and their interactions with substrates were studied by means of soft X-ray spectroscopy and DFT calculations. Their molecular architectures and the adsorption induced changes of the electronic structure were investigated.

In particular, the adsorption of metal-free phthalocyanine on the Au(111) surface was studied with DFT calculations including van der Waals (vdW) corrections. The calculations revealed differences among the vdW methods and the ones performing best this system could be determined. Moreover, in a joint experimental NEXAFS and DFT study, the influence of the substrate on the electronic states in the molecule was analysed. In future, it will be interesting to understand how the electronic interaction between substrate and molecule is modified by a metalation of metal-free phthalocyanine.

The structural and electronic adsorption induced changes in the iron phthalocyanine (FePc) were investigated by evaporating FePc on Au(111), Cu(111) and Cu(100)$c(2\times2)$-2N/Cu(111) and analyzing XPS and STM measurements and DFT results. The study revealed that FePc undergoes a symmetry reduction from D_{4h} to C_2 if adsorbed on Cu(111). The reasons can be found in structural effects caused by the substrate and in electronic charge transfer and charge reorganization. The spin state of FePc is adsorption site dependent on Cu(100)$c(2\times2)$-2N/Cu(111). In particular the magnetic moment is quenched if the Fe ion directly adsorbs on a N atom. The spin state can further be quenched if the modifier molecule pyridine is adsorbed on the iron ion. To manipulate the spin-state of the FePc in a controllable way can lead to applications of FePc in, for example, data storage devices for spintronics.

The architectures of $LuPc_2$ molecular films on hydrogenated Si(100)2x1 is dependent on the thickness of the films. While the molecules lie flat on the substrate in submonolayer coverages, they begin to randomly arrange with increasing thickness. On pristine silicon, the molecules form clusters and their XPS signals indicate a strong interaction with the substrate. DFT calculations showed that the lower ring is strongly affected and the electronic and structural changes in the upper Pc rings are a consequence of the changes in the lower rings. The $LuPc_2$ is a prototypical double-decker phthalcyanine with 14 f-electrons and the knowledge gained can help to elucidate the physics of other double-decker phthalocyanine with a not completely filled f-shell.

The electronic structure of the biphenylene molecule and the hypothetical biphenylene carbon (BPC) were studied. The BPC is a periodic 2D carbon network with a biphenylene-like basis. By means of DFT and GW calculations, an accurate electronic description compared to experimental PES data

of the gas-phase molecule could be obtained. Also DFT methods with GW-like accuracy were determined for the biphenylene molecule. Insights for the adsorption of biphenylene on Cu(111) were obtained by NEXAFS measurements, which showed that the biphenylene molecule adsorbs flat on the surface in low coverages while with increasing film thickness the adsorption angles between surface and molecule increase. If biphenylene can be used to build BPC, the GW and GW/BSE calculations predict a band gap of 1 eV and an optical gap of 0.5 eV in BPC, respectively. The obtained insights so far are promising and further modifications of BPC could lead to an increase or decrease of the band gap and the optical gap. Then, the properties of BPC can be optimized to suite a certain application. Although further investigations are required, BPC is a promising material for solar energy conversion and quantum information technology since it absorbs visible light and bright and dark excitons can be generated in BPC.

The approach to computed *L*-edges which was proposed here, adopts the hybridization function known from DMFT and it is used to parameterize a single impurity Anderson model including an additional excited state Hamiltonian. The results obtained for NiO, CoO, FeO and MnO are promising and it will be very interesting to extend the application to metal-organic systems like the iron phthalocyanine. The hope is that these calculations will allow to determine the changes in the magnetic properties induced in these compounds by adsorption on surfaces or by other chemical changes. Indeed, the method will be extended to compute XMCD signals to provide further insights.

7. Populärvetenskaplig sammanfattning

Innovationer kan förändra samhället. Införandet av datorer i nästan varje aspekt av det dagliga livet även representerar början av kisel perioden. Moores lag förutspådde tidigt utvecklingen av datorkraft. Var 18:e månad fördubblades datorkraft. Kontinuerliga framsteg gör detta möjligt. Här är sökandet efter nya material ett viktigt bidrag. 70% av alla innovationer beror på nya material. Detta gäller inte bara för kiselindustrin, men också många andra områden som medicin och rymdfärder.

Inflygning organiska föreningar, det vill säga material bestående huvudsakligen av grundämnena kol, syre och kväve, kan öppna nya vägar. Andra element kan vara av betydelse. Övergångsmetaller är kända för att förekomma i många organiska föreningar. Övergångsmetaller kan bestämma många egenskaper av metall-organiska föreningar. Viktiga fördelar kan vara låga produktionskostnader, sort och modifierbarhet av organiska och metallorganiska material. Frågan är vilka ämnen som kan användas och i vilket syfte. Spektroskopiska metoder, till exemple Röntgen fotoelektron- och absorptionsspektroskopi, kan användas att erhålla information om strukturen och elektroniska tillstånd. När de kombineras med beräkningar som baseras på täthetsfunktionalteori, för insikter på en atomär upplösning möjligt.

Ftalocyanin molekyler har väckt stort intresse på grund av deras robusthet mot värme och kemiska angrepp. Dessa molekyler kan även ha många olika metallcentrum, vilket ger dem ett slags variabilitet. Detta möjlig gör att anpassa deras särdrag after önskad användningssätt och att optimera för detta. Väsentligt är att förstå exakta växelverkan mellan molekylen och ytan. Den metall-fri ftalocyanin spelar en särskild roll. Nämligen, det är den enda ftalocyanin utan metallcentrum. Därför finns det möjlighet att studeras egenskaperna hos den organiska delen av molekylen. Järn-ftalocyanin molekyler (FePc) är på grund av på järnkärnas magnetiska moment en kandidat för användning i spinntroniska enheter, som en byggsten i lagringsenheter och organiska fälteffekttransistorer. Det har visat sig att egenskaperna hos FePc genom adsorption till ytor kan varieras. En riktad manipulation av egenskaperna är således inom räckhåll, antingen genom adsorption eller att ytterligare ändra molekyler som interagerar med FePc. Det finns också ftalocyanin biplan, som har ett lantanid metallcentrum i middel av två ftalocyanin ringar. Lutetium-bis-ftalocyanin är en av dem. Den kan tillämpas som en gassensor. Därför är det viktigt att veta den molekylära arkitekturen av molekylerna i filmerna, eftersom strukturen av de molekylära filmerna också kan påverka funktionen av gassensorerna.

Det finns också möjligheten att producera nya material med den så kallade *bottom-up* metoden. Molekylen bifenylen är en kandidat att producera två-dimensionell bifenylen Kol (BPC) med en *bottom-up* process. Teoretiska beräkningar har visat att BPC har ett bandgap av c:a 1 eV. Detta kan kanske användas i elektroniska komponenter. Också den beräknade absorptionen av synligt ljus är stora potentiella användningsområden för BPC.

8. Acknowledgements

When I was young and promising i got the opportunity to conduct PhD studies at the Division of Materials Theory at Uppsala University. I am very grateful for this unique opportunity and all the scattering events within this relatively short time window. During my studies, I encountered various correlation effects. In particular, my work was always supported by my supervisors who were always open to new ideas and critical discussions. Their responses were always helpful and the fruitful interactions resulted in a progressing development of my scientific knowledge. Therefore, I want to thank all of them: Olle Eriksson, Biplab Sanyal, Olle Björnholm and Barbara Brena. Thank you for sharing your knowledge, scientific experiences, advice, time and corrections during the last few years.

Also the interactions with the experimental teams were always pleasant, while sometimes scientifically challenging. First of all, I would like to thank Carla Puglia who directed me to the Materials Theory Division many years back. Ieva and Nadine, thank you for the very pleasant collaboration on the $LuPc_2$. The experimental insights were astonishing and I really think it helped to set up the calculations. I also appreciated to work with Jan Rusz who helped me to use Wien2K and for the fruitful discussions. We obtained some nice insights. Olesia and Prof. Joachim Schnadt, working with you has been challenging in a good way. Pushing limits farther is fun and even a nice thing to do if it works out. Fortunately it did, and I really like the insights we got on the FePc.

On the scientific path, I met a lot of people sharing the same drive for scientific progress. David, Shira and Prof. Leeor Kronik, thank you for helping me to use the OT-RSH approach. Prof. Henrik Ottosson, I appreciated the discussions on the biphenylene carbon with you. I hope we can continue in this direction.

However, there are much more people to thank for their support: Nina, Roberta, Teng, Valeria, Cesare, Monica and Marcello, you did so many of the measurements. Visiting once at a measurement in Trieste was very interesting and to see how measurements are actually taken at the synchrotron answered some of my questions.

Iulia and Soumyajyoti, it was a nice collaboration with you and it helped to understand more about metal-phthalocyanines. The discussions I had with Rocio and Heike about the theoretical aspects, applied to some systems or in general, were always useful. Heike, thank you for all your feedback. I also want to thank Nina and Satadeep, who were sharing the office with me. I enjoyed the discussions with you about and not about physics.

The DMFT team but especially Inka, Diana, Johan, Samara, Wei Wei, Yaroslav and Igor, I would like to thank again for the help with RSPt. Yaroslav, the time in Dresden at the Max Planck Institute (MPI) was great! Maurits, thanks for being and awesome host at the MPI, I still have the MPI cup! Without you two, the *L*-edge project would not have come so far. Johan, thanks for the help with the Swedish.

Mattias, Ulf and Allan gave me the opportunity to teach which I appreciate. Working with the students was challenging and fun at the same time. At this point I would like to thank Lisa, Sofie, Johan, Jonathan, Gergana, Shirin and Erik with whom I have actively supervised students in the labs.

A big thanks goes to Beate Pfützner-Bechler for providing the X-ray image of a cat.

I would also like to thank any others who have helped me along this journey, although their names may not have been mentioned here.

Last but not least, a special acknowledgement goes to the Knut and Alice Wallenberg foundation (KAW) which provided the financial support for my studies.

Appendix A: explicit formulas of the GW approach

The explicit equations of Hedin's wheel are given:

$$G(12) = G_0(12) + \int d(34) G_0(13) \Sigma(34) G(42) \tag{8.1}$$

$$\Gamma(12;3) = \delta(12)\delta(13) + \int d(4567) \frac{\partial \Sigma(12)}{\partial G(45)} G(46) G(75) \Gamma(67;3) \tag{8.2}$$

$$\chi(12) = -i \int d(34) G(13) G(41^+) \Gamma(34;2) \tag{8.3}$$

$$W(12) = v(12) + \int d(34) W(13) \chi(34) v(42) \tag{8.4}$$

$$\Sigma(12) = i \int d(34) G(14^+) W(13) \Gamma(42;3) \tag{8.5}$$

References

[1] EUROPEAN COMMISSION - Directorate-General for Research and Innovation, "Technology and market perspective for future value added materials," (2012).

[2] P. Petit, Synthetic Metals **46**, 147 (1992).

[3] N. Ishikawa and Y. Kaizu, Coordination chemistry reviews **226**, 93 (2002).

[4] J. Janczak, R. Kubiak, J. Richter, and H. Fuess, Polyhedron **18**, 2775 (1999).

[5] N. Nombona, E. Antunes, C. Litwinski, and T. Nyokong, Dalton Trans. **40**, 11876 (2011).

[6] S. Uchida, J. Xue, B. P. Rand, and S. R. Forrest, Applied physics letters **84**, 4218 (2004).

[7] M. Mannini, F. Bertani, C. Tudisco, L. Malavolti, L. Poggini, K. Misztal, D. Menozzi, A. Motta, E. Otero, P. Ohresser, P. Sainctavit, G. G. Condorelli, E. Dalcanale, and R. Sessoli, Nat Commun **5** (2014), article.

[8] J. Huang, K. Xu, S. Lei, H. Su, S. Yang, Q. Li, and J. Yang, The Journal of chemical physics **136**, 064707 (2012).

[9] Y.-H. Zhou, J. Zeng, L.-M. Tang, K.-Q. Chen, and W. Hu, Organic Electronics **14**, 2940 (2013).

[10] M. Bouvet, Analytical and bioanalytical chemistry **384**, 366 (2006).

[11] K. S. Karimov, I. Qazi, U. Shafique, M. Mahroof-Tahir, T. A. Khan, and S. N. Haider, in *Signal Processing and Communications, 2007. ICSPC 2007. IEEE International Conference on* (2007) pp. 848–851.

[12] R. Bonnett, Chemical Society Reviews **24**, 19 (1995).

[13] H. S. Majumdar, A. Bandyopadhyay, and A. J. Pal, Organic Electronics **4**, 39 (2003).

[14] J. F. Moulder, J. Chastain, and R. C. King, *Handbook of X-ray photoelectron spectroscopy: a reference book of standard spectra for identification and interpretation of XPS data* (Physical Electronics Eden Prairie, MN, 1995).

[15] J. J. Sakurai and J. Napolitano, *Modern quantum mechanics* (Addison-Wesley, 2011).

[16] C. Cohen-Tannoudji, B. Diu, and F. Laloë, *Quantum mechanics* (2000).

[17] P. Hohenberg and W. Kohn, Phys. Rev. **136**, B864 (1964).

[18] W. Kohn and L. J. Sham, Phys. Rev. **140**, A1133 (1965).

[19] M. Born and R. Oppenheimer, Annalen der Physik **389**, 457 (1927).

[20] K. Capelle, eprint arXiv:cond-mat/0211443 (2002), cond-mat/0211443 .

[21] S. Vosko, L. Wilk, and M. Nusair, Canadian Journal of Physics **58**, 1200 (1980).

[22] D. M. Ceperley and B. J. Alder, Phys. Rev. Lett. **45**, 566 (1980).

[23] J. P. Perdew, K. Burke, and M. Ernzerhof, Phys. Rev. Lett. **77**, 01479 (1996).

[24] J. Perdew, J. Chevary, S. Vosko, K. Jackson, M. Pederson, D. Singh, and C. Fiolhais, Phys. Rev. B **46**, 6671 (1992).

[25] J. Perdew, J. Chevary, S. Vosko, K. Jackson, M. Pederson, D. Singh, and C. Fiolhais, Phys. Rev. B **48**, 4978 (1993).
[26] J. P. Perdew, K. Burke, and Y. Wang, Phys. Rev. **54**, 1 (1996).
[27] F. London, Z. Phys. Chem **B22**, 22 (1930).
[28] J. P. Perdew and M. Levy, Phys. Rev. Lett. **51**, 1884 (1983).
[29] L. J. Sham and M. Schlüter, Phys. Rev. Lett. **51**, 1888 (1983).
[30] Y. Ma, M. Eremets, A. R. Oganov, Y. Xie, I. Trojan, S. Medvedev, A. O. Lyakhov, M. Valle, and V. Prakapenka, Nature **458**, 182 (2009).
[31] K. Held, C. Taranto, G. Rohringer, and A. Toschi, ArXiv e-prints (2011), arXiv:1109.3972 [cond-mat.mtrl-sci] .
[32] T. Yanai, D. P. Tew, and N. C. Handy, Chem. Phys. Lett. **393**, 51 (2004).
[33] A. D. Becke, jcp **98**, 1372 (1993).
[34] C. Lee, W. Yang, and R. Parr, Physical Review B **37**, 785 (1988).
[35] P. Stephens, F. Devlin, C. Chabalowski, and M. J. Frisch, The Journal of Physical Chemistry **98**, 11623 (1994).
[36] J. Paier, M. Marsman, K. Hummer, G. Kresse, I. C. Gerber, and J. G. Angyan, The Journal of Chemical Physics **124**, 154709 (2006).
[37] A. V. Krukau, O. A. Vydrov, A. F. Izmaylov, and G. E. Scuseria, The Journal of Chemical Physics **125**, 224106 (2006).
[38] A. D. Becke, Phys. Rev. A **38**, 3098 (1988).
[39] A. Tkatchenko and M. Scheffler, Phys. Rev. Lett. **102**, 073005 (2009).
[40] S. Grimme, J. Comput. Chem. **27**, 1787 (2006).
[41] A. Tkatchenko, A. Ambrosetti, and R. A. DiStasio, J. Chem. Phys. **138**, 074106 (2013).
[42] J. Klimeš, D. R. Bowler, and A. Michaelides, Phys. Rev. B **83**, 195131 (2011).
[43] J. Klimeš, D. R. Bowler, and A. Michaelides, J. Phys.: Condens. Matter **22**, 022201 (2010).
[44] O. A. Vydrov and T. Van Voorhis, The Journal of Chemical Physics **130**, 104105 (2009).
[45] H. Rydberg, M. Dion, N. Jacobson, E. Schröder, P. Hyldgaard, S. I. Simak, D. C. Langreth, and B. I. Lundqvist, Phys. Rev. Lett. **91**, 126402 (2003).
[46] M. Dion, H. Rydberg, E. Schröder, D. C. Langreth, , and B. I. Lundqvist, Phys. Rev. Lett. **92**, 246401 (2004).
[47] K. Lee, E. D. Murray, L. Kong, B. I. Lundqvist, and D. C. Langreth, Phys. Rev. B **82**, 081101 (2010).
[48] D. C. Langreth, B. I. Lundqvist, S. D. Chakarova-Kï¿½ck, V. R. Cooper, M. Dion, P. Hyldgaard, A. Kelkkanen, J. Kleis, L. Kong, S. Li, P. G. Moses, E. Murray, A. Puzder, H. Rydberg, E. Schrï¿½der, and T. Thonhauser, Journal of Physics: Condensed Matter **21**, 084203 (2009).
[49] A. D. Becke, The Journal of Chemical Physics **98**, 5648 (1993).
[50] C. Adamo and V. Barone, The Journal of Chemical Physics **110**, 6158 (1999).
[51] J. P. Perdew, M. Ernzerhof, and K. Burke, The Journal of Chemical Physics **105**, 9982 (1996).
[52] J. Heyd, G. E. Scuseria, and M. Ernzerhof, The Journal of Chemical Physics **124**, 219906 (2006).
[53] S. Refaely-Abramson, S. Sharifzadeh, M. Jain, R. Baer, J. B. Neaton, and L. Kronik, Phys. Rev. B **88**, 081204 (2013).

[54] S. Refaely-Abramson, S. Sharifzadeh, N. Govind, J. Autschbach, J. B. Neaton, R. Baer, and L. Kronik, Phys. Rev. Lett. **109**, 226405 (2012).
[55] L. Kronik, T. Stein, S. Refaely-Abramson, and R. Baer, Journal of Chemical Theory and Computation **8**, 1515 (2012), http://pubs.acs.org/doi/pdf/10.1021/ct2009363 .
[56] D. A. Egger, S. Weissman, S. Refaely-Abramson, S. Sharifzadeh, M. Dauth, R. Baer, S. Kümmel, J. B. Neaton, E. Zojer, and L. Kronik, Journal of Chemical Theory and Computation **10**, 1934 (2014).
[57] J. Wyrick, D.-H. Kim, D. Sun, Z. Cheng, W. Lu, Y. Zhu, K. Berland, Y. S. Kim, E. Rotenberg, M. Luo, P. Hyldgaard, T. L. Einstein, and L. Bartels, Nano Letters **11**, 2944 (2011), http://pubs.acs.org/doi/pdf/10.1021/nl201441b .
[58] J. E. Allen, B. Ray, M. R. Khan, K. G. Yager, M. A. Alam, and C. T. Black, Applied Physics Letters **101**, 063105 (2012).
[59] J. Lüder, B. Sanyal, O. Eriksson, C. Puglia, and B. Brena, Physical Review B **89**, 045416 (2014).
[60] M. N. Shariati, J. Lüder, I. Biedermane, S. Ahmadi, E. Göthelid, P. Palmgren, B. Sanyal, O. Eriksson, M. N. Piancastelli, B. Brena, and C. Puglia, J. Phys. Chem. .
[61] E. Abad, J. Ortega, Y. J. Dappe, and F. Flores, Appl. Phys. A **95**, 119 (2009).
[62] N. Marom, R. A. DiStasio, V. Atalla, S. Levchenko, A. M. Reilly, J. R. Chelikowsky, L. Leiserowitz, and A. Tkatchenko, Angewandte Chemie International Edition **52**, 6629 (2013).
[63] W. Liu, J. Carrasco, B. Santra, A. Michaelides, M. Scheffler, and A. Tkatchenko, Surf. Sci. **1**, 3.
[64] S. L. Price, Phys. Chem. Chem. Phys. **10**, 1996 (2008).
[65] A. M. Reilly and A. Tkatchenko, Phys. Rev. Lett. **113**, 055701 (2014).
[66] D. A. Egger, V. G. Ruiz, W. A. Saidi, T. Buško, A. Tkatchenko, and E. Zojer, J. Phys. Chem. C **117**, 3055 (2013).
[67] V. V. Gobre and A. Tkatchenko, Nat Commun **4**, 2341 (2013).
[68] A. Tkatchenko, R. A. DiStasio, R. Car, and M. Scheffler, Phys. Rev. Lett. **108**, 236402 (2012).
[69] J. F. Dobson, A. White, and A. Rubio, Phys. Rev. Lett. **96**, 073201 (2006).
[70] J. Dobson, in *Time-Dependent Density Functional Theory*, Lecture Notes in Physics, Vol. 706, edited by M. Marques, C. Ullrich, F. Nogueira, A. Rubio, K. Burke, and E. U. Gross (Springer Berlin Heidelberg, 2006) pp. 443–462.
[71] D. C. Langreth and J. P. Perdew, Phys. Rev. B. **15**, 2884 (1977).
[72] H. B. G. Casimir and D. Polder, Phys. Rev. **73**, 772 (1947).
[73] S. Grimme, Journal of Computational Chemistry **25**, 1463 (2004).
[74] W. Hujo and S. Grimme, Journal of Chemical Theory and Computation **9**, 308 (2013), http://pubs.acs.org/doi/pdf/10.1021/ct300813c .
[75] J. D. Baran and J. A. Larsson, J. Phys. Chem. C **116**, 9487 (2012).
[76] Y. Y. Zhang, S. X. Du, and H.-J. Gao, Phys. Rev. **84**, 125446 (2011).
[77] X. Chu and A. Dalgarno, The Journal of Chemical Physics **121**, 4083 (2004).
[78] F. Hanke, M. S. Dyer, J. Björk, and M. Persson, Journal of Physics: Condensed Matter **24**, 424217 (2012).
[79] T. Bucko, S. Lebègue, J. Hafner, and J. G. Ángyán, Phys. Rev. B **87**, 064110 (2013).

[80] S. C. Leemann, A. Andersson, M. Eriksson, L.-J. Lindgren, E. Wallén, J. Bengtsson, and A. Streun, Phys. Rev. ST Accel. Beams **12**, 120701 (2009).
[81] J. Tersoff and D. R. Hamann, Phys. Rev. B **31**, 805 (1985).
[82] D. Woodruff, Progress in Surface Science **57**, 1 (1998).
[83] J. Zegenhagen, Surface Science Reports **18**, 202 (1993).
[84] C. Nordling, E. Sokolowski, and K. Siegbahn, Phys. Rev. **105**, 1676 (1957).
[85] D. W. Turner and M. I. A. Jobory, The Journal of Chemical Physics **37**, 3007 (1962).
[86] D. M. Hercules and S. H. Hercules, Journal of Chemical Education **61**, 402 (1984), http://pubs.acs.org/doi/pdf/10.1021/ed061p402 .
[87] D. E. Sayers, E. A. Stern, and F. W. Lytle, Phys. Rev. Lett. **27**, 1204 (1971).
[88] H. Peisert, X. Liu, D. Olligs, A. Petr, L. Dunsch, T. Schmidt, T. Chassï¿½, and M. Knupfer, Journal of Applied Physics **96**, 4009 (2004).
[89] J. Rehr, A. Ankudinov, and S. Zabinsky, Catalysis Today **39**, 263 (1998).
[90] M. P. Seah, Surface and Interface Analysis **2**, 222 (1980).
[91] J. L. Cabellos, D. J. Mowbray, E. Goiri, A. El-Sayed, L. Floreano, D. G. de Oteyza, C. Rogero, J. E. Ortega, and A. Rubio, The Journal of Physical Chemistry C **116**, 17991 (2012), http://dx.doi.org/10.1021/jp3004213 .
[92] O. Snezhkova, J. Lüder, A. Wiengarten, S. R. Burema, F. Bischoff, Y. He, J. Rusz, J. Knudsen, M.-L. Bocquet, K. Seufert, J. V. Barth, W. Auwärter, B. Brena, and J. Schnadt, Phys. Rev. B **92**, 075428 (2015).
[93] F. de Groot, Coordination Chemistry Reviews **249**, 31 (2005), synchrotron Radiation in Inorganic and Bioinorganic Chemistry.
[94] J. J. Rehr and R. C. Albers, Rev. Mod. Phys. **72**, 621 (2000).
[95] H. S. Allen, Obituary Notices of Fellows of the Royal Society **5**, 341 (1947), http://rsbm.royalsocietypublishing.org/content/5/15/341.full.pdf .
[96] J. Stohr, Springer Series in Surface Science **25** (1992).
[97] H. Wang, C. Ralston, D. Patil, R. Jones, W. Gu, M. Verhagen, M. Adams, P. Ge, C. Riordan, C. Marganian, *et al.*, Journal of the American Chemical Society **122**, 10544 (2000).
[98] A. Serrano, O. R. de la Fuente, C. Monton, A. Muñoz-Noval, I. Valmianski, J. Fernández, G. Castro, I. K. Schuller, and M. García, Journal of Physics D: Applied Physics **49**, 125503 (2016).
[99] G. Schütz, W. Wagner, W. Wilhelm, P. Kienle, R. Zeller, R. Frahm, and G. Materlik, Phys. Rev. Lett. **58**, 737 (1987).
[100] C. Rostgaard, K. W. Jacobsen, and K. S. Thygesen, Phys. Rev. B **81**, 085103 (2010).
[101] F. Aryasetiawan and O. Gunnarsson, Rep. Prog. Phys. **61**, 237 (1998).
[102] L. Hedin, Phys. Rev. **139**, A796 (1965).
[103] L. Hedin, Journal of Physics: Condensed Matter **11**, R489 (1999).
[104] F. Bechstedt, *Many-Body Approach to Electronic Excitations* (Springer Berlin Heidelberg, Berlin, Heidelberg, 2015).
[105] F. Aryasetiawan and O. Gunnarsson, Reports on Progress in Physics **61**, 237 (1998).
[106] L. G. Molinari, Phys. Rev. B **71**, 113102 (2005).
[107] A. Marini, C. Hogan, M. Grüning, and D. Varsano, Computer Physics Communications **180**, 1392 (2009).

[108] S. Lebègue, B. Arnaud, M. Alouani, and P. E. Bloechl, Phys. Rev. B **67**, 155208 (2003).
[109] F. Bruneval, N. Vast, and L. Reining, Phys. Rev. B **74**, 045102 (2006).
[110] T. Kotani, M. van Schilfgaarde, and S. V. Faleev, Phys. Rev. B **76**, 165106 (2007).
[111] N. Marom, F. Caruso, X. Ren, O. T. Hofmann, T. Körzdörfer, J. R. Chelikowsky, A. Rubio, M. Scheffler, and P. Rinke, Phys. Rev. B **86**, 245127 (2012).
[112] F. Caruso, P. Rinke, X. Ren, A. Rubio, and M. Scheffler, Phys. Rev. B **88**, 075105 (2013).
[113] M. S. Hybertsen and S. G. Louie, Phys. Rev. Lett. **55**, 1418 (1985).
[114] S. G. Louie and A. Rubio, "Handbook of materials modeling: Methods," (Springer Netherlands, Dordrecht, 2005) Chap. Quasiparticle and Optical Properties of Solids and Nanostructures: The GW-BSE Approach, pp. 215–240.
[115] M. S. Hofmann, J. T. Gluckert, J. Noe, C. Bourjau, R. Dehmel, and A. Hogele, Nat Nano **8**, 502 (2013), letter.
[116] G. Bulgarini, M. E. Reimer, M. Hocevar, E. P. A. M. Bakkers, L. P. Kouwenhoven, and V. Zwiller, Nat Photon **6**, 455 (2012).
[117] E. L. Shirley, Journal of Electron Spectroscopy and Related Phenomena **136**, 77 (2004), progress in Core-Level Spectroscopy of Condensed Systems.
[118] Y. Liang, R. Soklaski, S. Huang, M. W. Graham, R. Havener, J. Park, and L. Yang, Phys. Rev. B **90**, 115418 (2014).
[119] B. Laikhtman, Journal of Physics: Condensed Matter **19**, 295214 (2007).
[120] G. Onida, L. Reining, and A. Rubio, Rev. Mod. Phys. **74**, 601 (2002).
[121] C. Y. Wong, R. M. Alvey, D. B. Turner, K. E. Wilk, D. A. Bryant, P. M. G. Curmi, R. J. Silbey, and G. D. Scholes, Nat Chem **4**, 396 (2012).
[122] A. Damjanović, I. Kosztin, U. Kleinekathöfer, and K. Schulten, Phys. Rev. E **65**, 031919 (2002).
[123] T. Kirchartz, J. Mattheis, and U. Rau, Phys. Rev. B **78**, 235320 (2008).
[124] E. R. Schmidgall, I. Schwartz, D. Cogan, L. Gantz, T. Heindel, S. Reitzenstein, and D. Gershoni, Applied Physics Letters **106**, 193101 (2015), http://dx.doi.org/10.1063/1.4921000.
[125] R. W. Meulenberg, J. R. Lee, A. Wolcott, J. Z. Zhang, L. J. Terminello, and T. van Buuren, ACS Nano **3**, 325 (2009), pMID: 19236067, http://dx.doi.org/10.1021/nn8006916 .
[126] Y. Kodriano, E. R. Schmidgall, Y. Benny, and D. Gershoni, Semiconductor Science and Technology **29**, 053001 (2014).
[127] B. Wang and N. V. Skorodumova, Phys. Chem. Chem. Phys. **16**, 13956 (2014).
[128] J. Singh and S. Kugler, physica status solidi (a) **206**, 993 (2009).
[129] G. D. Scholes and C. Smyth, The Journal of Chemical Physics **140**, 110901 (2014), http://dx.doi.org/10.1063/1.4869329.
[130] A. Thilagam, Journal of Mathematical Chemistry **53**, 466 (2014).
[131] C. X. Guo, G. H. Guai, and C. M. Li, Advanced Energy Materials **1**, 448 (2011).
[132] B. A. Gregg, The Journal of Physical Chemistry B **107**, 4688 (2003), http://dx.doi.org/10.1021/jp022507x .

[133] G. D. Scholes, G. R. Fleming, A. Olaya-Castro, and R. van Grondelle, Nat Chem **3**, 763 (2011).
[134] I. Schwartz, E. R. Schmidgall, L. Gantz, D. Cogan, E. Bordo, Y. Don, M. Zielinski, and D. Gershoni, Phys. Rev. X **5**, 011009 (2015).
[135] Y. Benny, S. Khatsevich, Y. Kodriano, E. Poem, R. Presman, D. Galushko, P. M. Petroff, and D. Gershoni, Phys. Rev. Lett. **106**, 040504 (2011).
[136] W. Wegscheider, L. N. Pfeiffer, M. M. Dignam, A. Pinczuk, K. W. West, S. L. McCall, and R. Hull, Phys. Rev. Lett. **71**, 4071 (1993).
[137] S. Botti and M. Gatti, "Fundamentals of time-dependent density functional theory," (Springer Berlin Heidelberg, Berlin, Heidelberg, 2012) Chap. The Microscopic Description of a Macroscopic Experiment, pp. 29–50.
[138] J. Harl, *The linear response function in density functional theory*, Ph.D. thesis, uniwien (2008).
[139] J. Vinson, *Bethe-Salpeter Equation Approach for Calculations of X-ray Spectra*, Ph.D. thesis (2013).
[140] M. Dvorak, S.-H. Wei, and Z. Wu, Phys. Rev. Lett. **110**, 016402 (2013).
[141] B. Arnaud, S. Lebègue, and M. Alouani, Phys. Rev. B **71**, 035308 (2005).
[142] G. Baym and L. P. Kadanoff, Phys. Rev. **124**, 287 (1961).
[143] H. Wang, K. Wong, G. Wong, and K. Law, Superlattices and Microstructures **24**, 41 (1998).
[144] Z. Ye, T. Cao, K. O/'Brien, H. Zhu, X. Yin, Y. Wang, S. G. Louie, and X. Zhang, Nature **513**, 214 (2014), letter.
[145] E. Poem, Y. Kodriano, C. Tradonsky, N. H. Lindner, B. D. Gerardot, P. M. Petroff, and D. Gershoni, Nat Phys **6**, 993 (2010).
[146] M. Zieliński, Y. Don, and D. Gershoni, Phys. Rev. B **91**, 085403 (2015).
[147] M. Nirmal, D. J. Norris, M. Kuno, M. G. Bawendi, A. L. Efros, and M. Rosen, Phys. Rev. Lett. **75**, 3728 (1995).
[148] M. Maragkou, Nat Mater **14**, 260 (2015), research Highlights.
[149] C. Hogan, M. Palummo, J. Gierschner, and A. Rubio, The Journal of Chemical Physics **138**, 024312 (2013), http://dx.doi.org/10.1063/1.4773582.
[150] S. M. Yoon, S. J. Lou, S. Loser, J. Smith, L. X. Chen, A. Facchetti, and T. Marks, Nano Letters **12**, 6315 (2012), http://pubs.acs.org/doi/pdf/10.1021/nl303419n .
[151] L. Yang, J. Deslippe, C.-H. Park, M. L. Cohen, and S. G. Louie, Phys. Rev. Lett. **103**, 186802 (2009).
[152] L. Yang, M. L. Cohen, and S. G. Louie, Nano Letters **7**, 3112 (2007), http://pubs.acs.org/doi/pdf/10.1021/nl0716404 .
[153] M. Wang and C. M. Li, Nanoscale **4**, 1044 (2012).
[154] K. F. Mak, F. H. da Jornada, K. He, J. Deslippe, N. Petrone, J. Hone, J. Shan, S. G. Louie, and T. F. Heinz, Phys. Rev. Lett. **112**, 207401 (2014).
[155] J. Lüder, C. Puglia, H. Ottosson, O. Eriksson, B. Sanyal, and B. Brena, The Journal of Chemical Physics **144**, 024702 (2016), http://dx.doi.org/10.1063/1.4939273.
[156] O. Pulci, M. Marsili, V. Garbuio, P. Gori, I. Kupchak, and F. Bechstedt, physica status solidi (b) , n/a (2014).
[157] S. Huang, Y. Liang, and L. Yang, Phys. Rev. B **88**, 075441 (2013).

[158] S. Yuan, M. Rösner, A. Schulz, T. O. Wehling, and M. I. Katsnelson, Phys. Rev. Lett. **114**, 047403 (2015).
[159] D. K. Samarakoon, Z. Chen, C. Nicolas, and X.-Q. Wang, Small **7**, 965 (2011).
[160] P. Cudazzo, C. Attaccalite, I. V. Tokatly, and A. Rubio, Phys. Rev. Lett. **104**, 226804 (2010).
[161] F. Karlicky and M. Otyepka, Journal of Chemical Theory and Computation **9**, 4155 (2013), pMID: 26592406, http://dx.doi.org/10.1021/ct400476r .
[162] J. C. Slater, Adv. Quantum Chem. **6** (1972), transition potential.
[163] D. A. Liberman, Phys. Rev. B **62**, 6851 (2000).
[164] B. Brena, P. E. M. Siegbahn, and H. Ågren, Journal of the American Chemical Society **134**, 17157 (2012), http://pubs.acs.org/doi/pdf/10.1021/ja306794p .
[165] M. Nyberg, Y. Luo, L. Triguero, L. G. M. Pettersson, and H. Ågren, Phys. Rev. B **60**, 7956 (1999).
[166] R. Laskowski, T. Gallauner, P. Blaha, and K. Schwarz, Journal of Physics: Condensed Matter **21**, 104210 (2009).
[167] G. A. Sawatzky and J. W. Allen, Phys. Rev. Lett. **53**, 2339 (1984).
[168] F. M. F. de Groot, J. C. Fuggle, B. T. Thole, and G. A. Sawatzky, Phys. Rev. B **42**, 5459 (1990).
[169] J. Zaanen, G. A. Sawatzky, and J. W. Allen, Phys. Rev. Lett. **55**, 418 (1985).
[170] O. Gunnarsson and K. Schönhammer, Phys. Rev. B **28**, 4315 (1983).
[171] T. Jo and A. Kotani, Journal of the Physical Society of Japan **57**, 2288 (1988), http://dx.doi.org/10.1143/JPSJ.57.2288 .
[172] A. Fujimori and F. Minami, Phys. Rev. B **30**, 957 (1984).
[173] P. W. Anderson, Phys. Rev. **124**, 41 (1961).
[174] T. Kroll, E. I. Solomon, and F. M. F. de Groot, The Journal of Physical Chemistry B **119**, 13852 (2015), pMID: 26226507, http://dx.doi.org/10.1021/acs.jpcb.5b04133 .
[175] E. Stavitski and F. M. de Groot, Micron **41**, 687 (2010).
[176] P. S. Miedema, S. Stepanow, P. Gambardella, and F. M. F. de Groot, Journal of Physics: Conference Series **190**, 012143 (2009).
[177] M. W. Haverkort, M. Zwierzycki, and O. K. Andersen, Phys. Rev. B **85**, 165113 (2012).
[178] F. de Groot, Chemical Reviews **101**, 1779 (2001), pMID: 11709999, http://dx.doi.org/10.1021/cr9900681 .
[179] C. Bethke, E. Kisker, N. B. Weber, and F. U. Hillebrecht, Phys. Rev. B **71**, 024413 (2005).
[180] M. W. Haverkort, eprint arXiv:cond-mat/0505214 (2005), cond-mat/0505214 .
[181] W. Olovsson, I. Tanaka, T. Mizoguchi, G. Radtke, P. Puschnig, and C. Ambrosch-Draxl, Phys. Rev. B **83**, 195206 (2011).
[182] J. Vinson, J. J. Rehr, J. J. Kas, and E. L. Shirley, Phys. Rev. B **83**, 115106 (2011).
[183] J. J. Rehr, J. A. Soininen, and E. L. Shirley, Physica Scripta **2005**, 207 (2005).
[184] E. L. Shirley, Journal of Electron Spectroscopy and Related Phenomena **144-147**, 1187 (2005), proceeding of the Fourteenth International Conference on Vacuum Ultraviolet Radiation Physics.
[185] R. Laskowski and P. Blaha, Phys. Rev. B **82**, 205104 (2010).

[186] E. Runge and E. K. U. Gross, Phys. Rev. Lett. **52**, 997 (1984).
[187] G. Fronzoni, R. De Francesco, and M. Stener, The Journal of Chemical Physics **137**, 224308 (2012), http://dx.doi.org/10.1063/1.4769789.
[188] K. Lopata, B. E. V. Kuiken, M. Khalil, and N. Govind, Journal of Chemical Theory and Computation **8**, 3284 (2012), pMID: 26605735, http://dx.doi.org/10.1021/ct3005613 .
[189] A. L. Ankudinov, A. I. Nesvizhskii, and J. J. Rehr, Phys. Rev. B **67**, 115120 (2003).
[190] J. Schwitalla and H. Ebert, Phys. Rev. Lett. **80**, 4586 (1998).
[191] P. A. Malmqvist, A. Rendell, and B. O. Roos, The Journal of Physical Chemistry **94**, 5477 (1990), http://dx.doi.org/10.1021/j100377a011 .
[192] R. V. Pinjari, M. G. Delcey, M. Guo, M. Odelius, and M. Lundberg, The Journal of Chemical Physics **141**, 124116 (2014), http://dx.doi.org/10.1063/1.4896373.
[193] M. Roemelt, D. Maganas, S. DeBeer, and F. Neese, The Journal of Chemical Physics **138**, 204101 (2013), http://dx.doi.org/10.1063/1.4804607.
[194] R. V. Pinjari, M. G. Delcey, M. Guo, M. Odelius, and M. Lundberg, Journal of Computational Chemistry **37**, 477 (2016).
[195] H. Ikeno, F. M. F. de Groot, E. Stavitski, and I. Tanaka, Journal of Physics: Condensed Matter **21**, 104208 (2009).
[196] P. Krüger and C. R. Natoli, Journal of Synchrotron Radiation **12**, 80 (2005).
[197] A. Grechnev, I. Di Marco, M. I. Katsnelson, A. I. Lichtenstein, J. Wills, and O. Eriksson, Phys. Rev. B **76**, 035107 (2007).
[198] A. Georges, G. Kotliar, W. Krauth, and M. J. Rozenberg, Rev. Mod. Phys. **68**, 13 (1996).
[199] F. de Groot, Journal of Electron Spectroscopy and Related Phenomena **67**, 529 (1994).
[200] A. El-Sayed, P. Borghetti, E. Goiri, C. Rogero, L. Floreano, G. Lovat, D. J. Mowbray, J. L. Cabellos, Y. Wakayama, A. Rubio, J. E. Ortega, and D. G. de Oteyza, ACS Nano **7**, 6914 (2013), pMID: 23883347, http://dx.doi.org/10.1021/nn4020888 .
[201] L. Köhler and G. Kresse, Physical Review B **70**, 165405 (2004).
[202] W. Olovsson, C. Göransson, L. V. Pourovskii, B. Johansson, and I. A. Abrikosov, Phys. Rev. B **72**, 064203 (2005).
[203] W. E. Jr., Surface Science Reports **6**, 253 (1987).
[204] L. Köhler and G. Kresse, Phys. Rev. B **70**, 165405 (2004).
[205] P. S. Bagus, E. S. Ilton, and C. J. Nelin, Surface Science Reports **68**, 273 (2013).
[206] E. Snow and J. Wood, Chemical Physics Letters **25**, 111 (1974).
[207] W. Kutzelnigg, U. Fleischer, and M. Schindler, "Deuterium and shift calculation," (Springer Berlin Heidelberg, Berlin, Heidelberg, 1991) Chap. The IGLO-Method: Ab-initio Calculation and Interpretation of NMR Chemical Shifts and Magnetic Susceptibilities, pp. 165–262.
[208] J. Park, S. Ryu, M.-s. Han, and S.-J. Oh, Phys. Rev. B **37**, 10867 (1988).
[209] P. Darancet, A. Ferretti, D. Mayou, and V. Olevano, Phys. Rev. B **75**, 075102 (2007).

[210] J. B. Neaton, M. S. Hybertsen, and S. G. Louie, Phys. Rev. Lett. **97**, 216405 (2006).
[211] Y. Bai, F. Buchner, M. T. Wendahl, I. Kellner, A. Bayer, H.-P. Steinrück, H. Marbach, and J. M. Gottfried, J. Phys. Chem. C **112**, 6087 (2008).
[212] K. Toyoda, Y. Nakano, I. Hamada, K. Lee, S. Yanagisawa, and Y. Morikawa, Surface Science **603**, 2912 (2009).
[213] Y. Morikawa, K. Toyoda, I. Hamada, S. Yanagisawa, and K. Lee, Current Applied Physics **12**, S2 (2012).
[214] Z. Hu, B. Li, A. Zhao, J. Yang, and J. G. Hou, J. Phys. Chem. C **112**, 13650 (2008).
[215] E. Abad, Y. J. Dappe, J. I. Martínez, F. Flores, and J. Ortega, J. Chem. Phys. **134**, 044701 (2011).
[216] J. Lüder, O. Eriksson, B. Sanyal, and B. Brena, The Journal of chemical physics **140**, 124711 (2014).
[217] M. Rosa, S. Corni, and R. D. Felice, J. Phys. Chem. C **116**, 21366 (2012).
[218] J. Wellendorff, A. Kelkkanen, J. J. Mortensen, B. I. Lundqvist, and T. Bligaard, Top. Catal. **53**, 378 (2010).
[219] I. Hamada and M. Tsukada, Phys. Rev. **83**, 245437 (2011).
[220] I. Kröger, B. Stadtmüller, C. Kleimann, P. Rajput, and C. Kumpf, Phys. Rev. B **83**, 195414 (2011).
[221] A. De Cian, M. Moussavi, J. Fischer, and R. Weiss, Inorganic Chemistry **24**, 3162 (1985), http://pubs.acs.org/doi/pdf/10.1021/ic00214a016 .
[222] J. A. de Saja and M. L. Rodríguez-Méndez, Adv. Colloid Interface Sci. **116**, 1 (2005).
[223] M. Bouvet and J. Simon, Chemical Physics Letters **172**, 299 (1990).
[224] Z. Belarbi, C. Sirlin, J. Simon, and J. J. Andre, The Journal of Physical Chemistry **93**, 8105 (1989), http://pubs.acs.org/doi/pdf/10.1021/j100361a026 .
[225] I. Yilmaz, T. Nakanishi, A. Gurek, and K. M. Kadish, Journal of Porphyrins and Phthalocyanines **07**, 227 (2003), http://www.worldscientific.com/doi/pdf/10.1142/S1088424603000318 .
[226] M. G. Martín, M. L. Rodríguez-Méndez, and J. A. de Saja, Langmuir **26**, 19217 (2010).
[227] V. Parra, M. Bouvet, J. Brunet, M. L. Rodriguez-Mendez, and J. A. de Saja, Thin Solid Films **516**, 9012 (2008), the Tenth European Conference on Organised Films (ECOF-10).
[228] J. Brunet, V. P. Garcia, A. Pauly, C. Varenne, and B. Lauron, Sensors and Actuators B: Chemical **134**, 632 (2008).
[229] J. Ahlund, K. Nilson, J. Schiessling, L. Kjeldgaard, S. Berner, N. Martensson, C. Puglia, B. Brena, M. Nyberg, and Y. Luo, The Journal of Chemical Physics **125**, 034709 (2006).
[230] D. Y. Qiu, F. H. da Jornada, and S. G. Louie, Phys. Rev. Lett. **111**, 216805 (2013).
[231] K. Berland and P. Hyldgaard, Phys. Rev. B **87**, 205421 (2013).
[232] H.-P. Komsa and A. V. Krasheninnikov, Phys. Rev. B **86**, 241201 (2012).
[233] L. Yang, C.-H. Park, Y.-W. Son, M. L. Cohen, and S. G. Louie, Phys. Rev. Lett. **99**, 186801 (2007).

[234] J. Lüder, M. de Simone, R. Totani, M. Coreno, C. Grazioli, B. Sanyal, O. Eriksson, B. Brena, and C. Puglia, The Journal of chemical physics **142**, 074305 (2015).
[235] R. Breslow, J. Brown, and J. J. Gajewski, Journal of the American Chemical Society **89**, 4383 (1967), http://dx.doi.org/10.1021/ja00993a023 .
[236] A. H. Castro Neto, F. Guinea, N. M. R. Peres, K. S. Novoselov, and A. K. Geim, Rev. Mod. Phys. **81**, 109 (2009).
[237] K. S. Novoselov, A. K. Geim, S. V. Morozov, D. Jiang, M. I. Katsnelson, I. V. Grigorieva, S. V. Dubonos, and A. A. Firsov, Nature **438**, 197 (2005).
[238] J. O. Sofo, A. S. Chaudhari, and G. D. Barber, Phys. Rev. B **75**, 153401 (2007).
[239] B. G. Kim and H. J. Choi, Phys. Rev. B **86**, 115435 (2012).
[240] A. T. Balaban, Rev. Roum. Chim. **13**, 231 (1968).
[241] R. De Boer, A. Stassen, M. Craciun, C. Mulder, A. Molinari, S. Rogge, and A. Morpurgo, Applied Physics Letters **86**, 262109 (2005).
[242] N. Tsukahara, K.-i. Noto, M. Ohara, S. Shiraki, N. Takagi, Y. Takata, J. Miyawaki, M. Taguchi, A. Chainani, S. Shin, *et al.*, Physical review letters **102**, 167203 (2009).
[243] I. Bidermane, J. Lüder, R. Totani, G. Cesare, M. de Simone, M. Coreno, A. Kivimäki, J. Åhlund, L. Lozzi, B. Brena, *et al.*, physica status solidi (b) (2015).
[244] J. van Elp, R. H. Potze, H. Eskes, R. Berger, and G. A. Sawatzky, Phys. Rev. B **44**, 1530 (1991).
[245] S. Massidda, A. Continenza, M. Posternak, and A. Baldereschi, Phys. Rev. Lett. **74**, 2323 (1995).
[246] B. Gilbert, B. H. Frazer, A. Belz, P. G. Conrad, K. H. Nealso, D. Haskel, J. C. Lang, G. Srajer, , and G. D. Stasio, The Journal of Physical Chemistry A **107**, 2839 (2003), http://dx.doi.org/10.1021/jp021493s .
[247] T. J. Regan, H. Ohldag, C. Stamm, F. Nolting, J. Lüning, J. Stöhr, and R. L. White, Phys. Rev. B **64**, 214422 (2001).
[248] F. M. F. de Groot, M. Abbate, J. van Elp, G. A. Sawatzky, Y. J. Ma, C. T. Chen, and F. Sette, Journal of Physics: Condensed Matter **5**, 2277 (1993).
[249] D. Alders, L. H. Tjeng, F. C. Voogt, T. Hibma, G. A. Sawatzky, C. T. Chen, J. Vogel, M. Sacchi, and S. Iacobucci, Phys. Rev. B **57**, 11623 (1998).
[250] P. Poizot, S. Laruelle, S. Grugeon, L. Dupont, and J.-M. Tarascon, Nature **407**, 496 (2000).
[251] M. Chen, X. Xia, M. Qi, J. Yuan, J. Yin, and Q. Chen, Materials Research Bulletin **73**, 125 (2016).
[252] C. Chen, Y. Huang, H. Zhang, X. Wang, Y. Wang, L. Jiao, and H. Yuan, Journal of Power Sources **314**, 66 (2016).
[253] D. Tian, W. Liu, Y. Chen, W. Yu, L. Yu, and B. Lin, Materials Research Bulletin **71**, 1 (2015).
[254] J. S. Lee, S. Lee, and T. W. Noh, Applied Physics Reviews **2**, 031303 (2015), http://dx.doi.org/10.1063/1.4929512.
[255] A. Sawa, Materials Today **11**, 28 (2008).
[256] K. Ogasawara, F. Alluqmani, and H. Nagoshi, ECS Journal of Solid State Science and Technology **5**, R3191 (2016).

[257] R. H. Potze, G. A. Sawatzky, and M. Abbate, Phys. Rev. B **51**, 11501 (1995).

Acta Universitatis Upsaliensis

Digital Comprehensive Summaries of Uppsala Dissertations from the Faculty of Science and Technology 1365

Editor: The Dean of the Faculty of Science and Technology

A doctoral dissertation from the Faculty of Science and Technology, Uppsala University, is usually a summary of a number of papers. A few copies of the complete dissertation are kept at major Swedish research libraries, while the summary alone is distributed internationally through the series Digital Comprehensive Summaries of Uppsala Dissertations from the Faculty of Science and Technology. (Prior to January, 2005, the series was published under the title "Comprehensive Summaries of Uppsala Dissertations from the Faculty of Science and Technology".)

Distribution: publications.uu.se
urn:nbn:se:uu:diva-282151

ACTA
UNIVERSITATIS
UPSALIENSIS
UPPSALA
2016